Discrete Element Modelling of Cavity Expansion in Granular Materials

by

Yan Geng

BEng, MSc

A thesis submitted to The University of Nottingham

for the degree of Doctor of Philosophy

September 2010

ABSTRACT

A granular material is usually an irregular packing of particles and its constitutive relationship is very complex. Previous researches have shown that the discrete element method is an effective tool for fundamental research of the behaviour of granular materials. In this research, discrete element modelling was used to obtain the macroscopic stress-strain behaviour of granular material in cavity expansion. The micro mechanical features and the mechanical behaviour of granular material at particle level have been investigated.

A simple procedure was used to generate the samples with spherical particles and two-ball clumps. The influence of particle properties on the stress-strain behaviour within an aggregate was investigated in biaxial test simulations. It was found that more angular clumps lead to sample more homogeneous and that the interlocking provided by the angular clumps induces a higher strength and dilation in the sample response. Interparticle friction was also found to have significant effect on the strength and dilation of the sample. The sample macromechanical properties can be obtained from these biaxial simulations.

For investigating the effect of particle shape, the spherical or non-spherical (two-ball clump) particle shapes were used in the cavity expansion simulations. Monotonic loading was performed on a fan-shaped sample with various particle properties under a range of initial cavity pressures. The results were

compared with calculated analytical solutions and existing experimental data in order to optimise the micro mechanical parameters governing the behaviour. The pressuremeter test data were adapted for this comparison since the theory of cavity expansion has been used to describe the pressuremeter tests in soil and rocks by many geotechnical researchers and engineers.

This research showed that particle properties play an important role in soil behaviour of cavity expansion under monotonic loading. The contribution of this research is to present that it is possible to model a granular material of boundary value problem (cavity expansion) under static conditions, providing micro mechanical insight into the behaviour.

ACKNOWLEDGEMENTS

This research was accomplished in the Nottingham Centre for Geomechanics during the period September 2007 to July 2010 with the help from many people.

I wish to express my sincere thanks to my supervisors Professor Hai-Sui Yu and Professor Glenn McDowell, for their expert supervision, encouragement, patience and advice throughout this research. Their guidance and supervision are gratefully acknowledged.

I would like also to thank all the colleagues and friends during my studying. Special thanks are given to Dr. Jean-francois Ferellec, Dr Phil Rowsell, Dr Xia Li, Dr Mingfei Lu, and Mr John De Bono for their help, encouragement and valuable comments during the writing of this thesis.

A great thank goes to Civil Engineering Department in the University of Nottingham for providing me the financial support during PhD study.

Finally, I would like to thank my parents for their constant support, love and encouragement.

TABLE OF CONTENTS

LIST OF FIGURES

LIST OF TABLES

NOTATION

a	Radius of the cavity during loading
a_0	Radius of the cavity at initial unloaded state
A	Area of bond disk
b	Outer radius of the plastic zone during loading
b_0	Outer radius of the plastic zone at initial unload state
BEM	Boundary Element Method
BCC	Body centred cubic
c	Cohesion
C	Total number of contact points on each sphere
DEM	Discrete Element Method
d	Diameter of a grain
$d\gamma$	Shear strain
e	Void ratio
e_c	Preordained void ratio at a critical state
E	Young's modulus
f_p	Total out-of-balance force
f_{ps}	Resultant contact force
f_{tpsc}	Tangential component of the contact force
F_i	Contact force vector

F_i^n	Normal contact force
F_i^s	Shear contact force
$F_{\max}^s$	Maximum allowable shear contact force
FEM	Finite Element Method
FCC	Face centred cubic
G	Gain factor
G_s	Specific gravity
g_i	Body force acceleration vector
H_i	Angular momentum of particle
HCP	Hexagonal close packed
I	Moment of inertia of the disc cross-section
J	Polar moment of inertia of the disc cross-section
K^n	Normal stiffness at contact
k^s	Shear stiffness at contact
L	Distance between the centres of two spheres in a clump
MDEM	Modified distinct element method
M_i	Resultant moment
m	Mass of a ball
n	Porosity
N	Number of balls in the clump
PFC^{3D}	Particle Flow Code in 3 Dimensions
p'	Mean effect stress
P	Cavity pressure
P_0	Initial cavity pressure
PMT	Pressuremeter Test

q	Deviator stress
R_d	Relative density
S	Total number of element spheres
SC	Smooth ends and constant boundary pressure
v	Poisson's ratio
Δt	Timestep
U^n	Overlap of the two entities
ΔU_i^s	Shear component of the contact displacement-increment vector
$x^{[p]}$	Centroid location of the ball
$x_i^{[G]}$	Mass of clump
ξ_a	Radial displacement at the inner boundary
ξ_b	Radial displacement at the outer boundary
ε	Cavity strain
ε_a	Axial strain
ε_v	Volumetric strain
μ	Friction coefficient
σ'_h	Effect horizontal stress
σ'_v	Effect vertical stress
σ_r	Total radius stress
σ_θ	Hoop stress
σ'_1	Major principal effective stress
σ'_3	Minor principal effective stress
σ_0	Initial consolidation confining pressure
φ	Friction angle

ψ	Dilatancy angle
ω_i	Angular velocity of particle
$\dot{\omega}_i$	Angular acceleration of particle
δ	Angle of bedding plane to the principal stress direction
α	Function of friction angle

CHAPTER 1

INTRODUCTION

1.1 Background

Cavity expansion analysis plays a significant role in modern soil mechanics and focuses on the cavity pressure needed to expand a cavity in soil by a certain amount. It provides a versatile and accurate method to analyze the expansion of cylindrical and spherical cavities in soil and rock in geotechnical engineering (Yu, 2000). Cavity expansion theory is concerned with the theoretical study of stress and displacement caused by the expansion and contraction of cylindrical or spherical cavities in either linear or nonlinear media. It used to describe the stress-strain behaviour of soil or rocks, so a mathematical constitutive model and soil properties are needed. Cavity expansion theory was first developed for application to metal indentation problems (Bishop et al., 1945; Hill, 1950). The application of cavity expansion theory to geotechnical problems came later (Gibson and Anderson, 1961; Meyerhof, 1951). The analysis of a cylindrical cavity has been applied to practical problems such as the interpretation of pressuremeter tests (Ladanyi, 1963; Palmer, 1972). The application used the principal of continuum mechanics and was based on constitutive models of various complexities. Three completely independent assumptions are made in classical continuum

mechanics, i.e. continuity, homogeneity and isotropy (Malvern, 1969). The idealization of material is called a continuum, or more precisely, model of the material (Khan and Huang, 1995). As granular materials consist of grains in contact and surrounding voids, the micromechanical behaviour of granular materials is therefore inherently discontinuous and heterogeneous, and generally anisotropic.

Kishino (1988) pointed out that in continuum mechanical analysis of granular materials, the determination of a constitutive model is the most difficult process. A constitutive model based on continuum approach usually includes a lot of model parameters, which sometimes have no clear physical meaning (Kishino, 1988). However, when one observes the granular materials as packed assemblies of particles, the mechanical interaction between particles is very simple and the material constants have explicit meaning. So granular media such as sand is composed of discrete particles and exhibits very complex macroscopic mechanical responses to externally applied loading. Discrete element method provides a better way to investigate the mechanic behaviour of granular material at both micro and macro level. The discrete element method was first developed by Cundall (1971) for rock mechanics and then is being increasingly used to simulate the mechanical behaviour of granular materials (Cundall and Strack, 1979; Ting et al., 1989; Rothenburg and Bathurst, 1992). The early DEM models usually considered the granular material as assemblies of interacting spheres and reproduced results qualitatively well. However, materials consisting of non-spherical particles behave significantly differently from those consisting of spherical particles (Lin and Ng, 1997). Many experiments show that the discrete characters of the granular materials and

disconnection of the sample are not fit application of continuum mechanics, and many researchers have investigate that DEM is an efficient method in studying granular materials in terms of both the macromechanical and micromechanical behaviours. In this case, simulation of cavity expansion in granular material using DEM is studied.

1.2 Aims and Objectives

Since Cundall in 1971 first introduced the innovative distinct element method into the research on granular materials, DEM has been developed to different levels and used to a wide range of engineering applications. The purpose of this project is to understand the mechanical behaviour of the granular material of cavity expansion and obtain the interaction at micro level by using discrete element method. However, real granular materials like sand are very complex and it is very difficult for the development of theory in this area if there are no simplifying assumptions. As a first approximation, real particle shape is ignored and the particles are modelled as spheres and simple clumps. It is also assumed that the spheres are elastic and no rolling resistance is considered.

In DEM, very little research has been reported on the boundary value problem. Therefore the aim is to study the cavity expansion using DEM and the objectives of this thesis can be stated as:

1. to use DEM to analyse cavity expansion in granular materials which is one of the most useful problems in geotechnical engineering, and develop a suitable particle model in PFC^{3D} that the response of granular materials under different loading conditions can be modelled.

2. to compare the DEM solutions with those predicted using cavity expansion theory based on continuum mechanics.
3. to check the validity of the DEM solutions by comparing them with the results of cavity expansion tests conducted in the laboratory.

1.3 Outline of Thesis

The thesis is divided into eight chapters. A brief layout of this thesis is given below.

Chapter 2 presents a literature review describing granular material, and a brief review of the development and applications of cavity expansion. In section 2.2 and 2.3, cavity expansion theory and the scope of the application in geomechanics is introduced. The geotechnical applications like in-situ soil testing are also discussed in this section. Section 2.4 mainly discusses the granular material characters and the mechanical behaviour of granular material.

Chapter 3 describes the discrete element method theory and the application, including the principal and numerical modelling using PFC^{3D}. The concepts and functions of PFC^{3D} and recent applications of PFC^{3D} in simulating soil behaviour are presented.

In Chapter 4, the preliminary numerical modelling using PFC^{3D} is presented. An attempt to simulate a biaxial test using spherical particles and the observed response is discussed. This simulation aims to obtain the soil parameters from the soil element parameters by using DEM, so it can give some advices of choosing the soil parameters when using cavity expansion method to obtain cavity expansion solution.

Chapter 5 presents the simulations of cavity expansion and preliminary numerical modelling using PFC^{3D}. Several simulations of cavity expansion with different particle parameters are described and show the effect of micro parameters of particle on the macro behaviour of the assembly in cavity expansion.

Chapter 6, the solution of DEM simulation using PFC^{3D} is compared with the analytical solution of cavity expansion method. Some results using cavity expansion method are explained and the comparison results are described as well.

Chapter 7 is going to describe the comparison results between DEM simulation and experimental tests. The self-boring pressuremeter test is presented in this chapter. The effect of particle parameters under monotonic loading is investigated in the self-boring pressuremeter test simulations.

Chapter 8, conclusions on the work presented in this thesis are provided and further developments are suggested.

CHAPTER 2

REVIEW OF DEVELOPMENT OF CAVITY EXPANSION AND GRANULAR MATERIAL

2.1. Introduction

Cavity expansion in soil or rock is a fundamental problem in theoretical geomechanics. Geotechnical engineering problems include the investigation of capacity of pile foundations, pile loading and earth anchors, the interpretation of in-situ soil testing, analysis of behaviours of tunnels and underground excavations, and the prediction of borehole instability. This chapter reviews the relevant literature, including the development of cavity expansion, the interpretation of in-situ soil test such as cone penetration test and pressuremeter test, and DEM investigation on granular materials. It begins with an introduction to cavity expansion theory and associated applications, followed by a description of in-situ tests as well as the development of laboratory devices. Finally, a literature review of recent studies about the investigation on granular materials, the development of computer technology, and discrete element modelling method is undertaken.

2.2 Cavity Expansion Theory

Cavity expansion theory was first developed for application to metal indentation problems (Bishop et al., 1945; Hill, 1950). The application of cavity expansion theory to geotechnical problems came later (Gibson and Anderson, 1961; Meyerhof, 1951). Cavity expansion theory focuses on the stress and displacement fields around cavities embedded. It has been widely applied in the in-situ soil testing, deep foundations, tunnels and underground excavations in soil and rock, and wellbore instability in the oil industry. It provides a useful and simple tool for many complex geotechnical problems. The cavity expansion or contraction is a one-dimensional boundary value problem using continuum mechanics to analyse. Therefore, a mathematical constitutive model and material properties to describe the stress-strain behaviour of soil are needed. The main application of cavity expansion theory in soil mechanics is the interpretation of in-situ testing (the cone penetrometer test and the pressuremeter test). Many researchers focus on this problem and papers have been published. Use of cavity expansion theory to solve practical problems is generally termed cavity expansion method. This method applies the cavity expansion theory to obtain fundamental solutions for a wide range of geotechnical problems and the analytical solutions are achieved through the soil properties (Young's modulus E, Poisson's ratio v, Friction angle, Cohesion and Dilation angle) and boundary conditions.

2.2.1 The development of cavity expansion theory

Originally, cavity expansion theory aimed to solve problems of metal indentation (Bishop et al., 1945; Hill, 1950). Later cavity expansion was

applied to geotechnical problems (Meyerhof, 1951). Chadwick (1959) is the first person who developed the analysis with the consideration of friction, adopting the Mohr-Coulomb criterion with an associate flow rule. In order to obtain the properties of soil and the pressure-expansion curve in pressuremeter test that the analysis of a cylindrical cavity has also been applied to interpret the pressuremeter tests (Palmer, 1972; Hughes et al., 1977; Houlsby and Withers, 1988; Ajalloeian and Yu, 1998; Houlsby and Yu, 1990; Yu and Collins, 1998). The work followed by the contributions of Schnaid and Mantaras (2003), who were interested in cavity expansion in cemented materials. Salgado and Randolph (2001) focused on the dependence of the friction angle on stress state and a numerical analysis of cavity expansion in sand was described.

An analysis of cylindrical or spherical cavity expansion in dilatant soil was presented by Yu and Houlsby (1991). Yu and Houlsby (1991) pointed out that it is very difficult to fit the complete real stress-strain behaviour of sandy soils satisfactorily (Figure 2.1) with a simple elastic perfectly plastic model in simple boundary problems such as cylindrical cavity expansion. Figure 2.1 shows the actual behaviour of sand and possible elastic-perfectly plastic models for this behaviour. A number of results were selected and summarised by Yu and Houlsby (1991) to indicate the effects of various parameters on the behaviour of cavity expansion. The pressure-expansion relationship was plotted in Figure 2.2 (the material's Poisson's ratio ν is 0.3, friction angle ϕ is 30º and a stiffness index E / $\{p_0+[Y/(\alpha-1)]\}$ is 260º). The dilation angles for these three curves are 0º, 15º, 30º respectively. It can be seen that the stiffness of the response increases with the dilatancy (Figure 2.2).

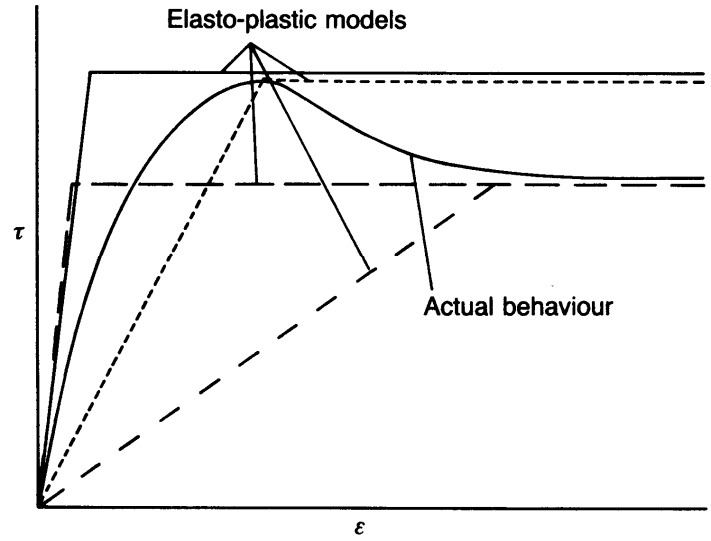

Figure 2.1: Actual behaviour of sands and possible elastic-perfectly plastic models (Yu and Houlsby, 1991)

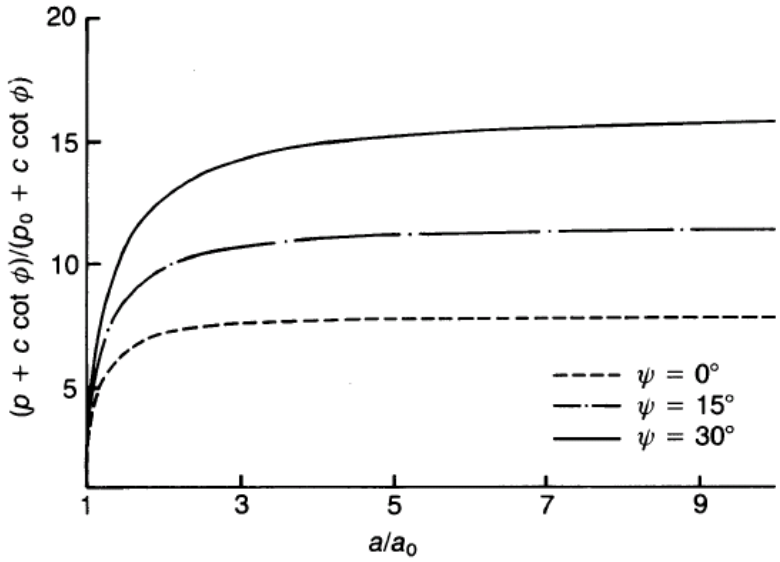

Figure 2.2: Typical pressure-expansion curves for cylindrical cavities (Yu and Houlsby, 1991)

More recently, the large-strain dynamic problem of cavity in granular medium was described by Institute for Geotechnical Engineering (2005). Rosenberg and Dekel (2008) described a numerical of simulations following the cavity expansion process. The constitutive model was considered as elastic-perfectly plastic solid. The relationship between the cavity wall velocity and the applied pressure in the cavity showed that the simulation result has a good agreement with the analytical models for compressible solids. In addition, there is a simple quadratic relation without a linear term between the dynamic radial stress and its wall velocity for the spherical cavity. For the cylindrical cavity, a linear term (in wall velocity) has to be added.

2.2.2 Fundamental solutions of cavity expansion problem (Yu, 2000)

Cavity expansion problems can be solved by considering the equations of equilibrium, compatibility, stress-strain relationship, and stress boundary conditions together with the failure criteria. In this case, numerous analytical solutions have been developed for cavity expansion.

Many existing soil and rock models can be divided into three groups and the appropriate one is selected for solving different problem conditions (Yu, 2000). Some fundamental solutions for cavity expansion problems are presented.

1. elastic models (linear or nonlinear)
2. viscoelastic or viscoelastic-plastic models
3. elastic-plastic models (perfectly plastic or strain hardening/softening)

2.2.2.1. Elastic solutions

For the expansion of thick-walled cylinder, the plane strain condition is assumed since an infinitely long cylinder is considered.

The final stresses are:

$$\sigma_r = -\frac{p_0 b^2 (r^2 - a^2)}{r^2 (a^2 - b^2)} - \frac{p a^2 (b^2 - r^2)}{r^2 (a^2 - b^2)} \tag{2.1}$$

$$\sigma_\theta = -\frac{p_0 b^2 (r^2 + a^2)}{r^2 (a^2 - b^2)} + \frac{p a^2 (b^2 + r^2)}{r^2 (a^2 - b^2)} \tag{2.2}$$

The radial displacement u can be determined:

$$u = -r\varepsilon_\theta = \frac{p - p_0}{2G(\frac{1}{a^2} - \frac{1}{b^2})}\left[\frac{1-2\upsilon}{b^2} r + \frac{1}{r}\right] \tag{2.3}$$

where G=E/2(1+ν) is the shear modulus of the material.

2.2.2.2 Elastic-perfectly plastic solutions

Some basic cavity expansion solutions in elastic-perfectly plastic soils are described. The soil behaviour is assumed to be under either drained or undrained conditions when modelled by perfect plasticity. The elastic-plastic solutions for cavity expansion using both Tresca and Mohr-Coulomb plasticity models are presented.

For cylindrical cavity expansion in a finite medium, solution for Tresca criterion is described first. A long, plane strain cylindrical tube is expanded by an internal pressure. Internal pressure increase from the initial value p_0, the material behaviour first is elastic and then become plastic from the internal radius to the external radius.

The elastic solutions for stress and displacement are:

$$\sigma_r = -p_0 - (p - p_0)(\frac{b_0^2}{r^2} - 1)/(\frac{b_0^2}{a_0^2} - 1) \tag{2.4}$$

$$\sigma_\theta = -p_0 + (p - p_0)(\frac{b_0^2}{r^2} + 1)/(\frac{b_0^2}{a_0^2} - 1) \tag{2.5}$$

$$u = \frac{(1+v)(p - p_0)}{E(\frac{b_0^2}{a_0^2} - 1)}\left[(1-2v)r + \frac{b_0^2}{r}\right] \tag{2.6}$$

When the internal pressure gets to p_{1y}, yielding begins to occur on internal surface:

$$p_{1y} = \frac{Y}{2}(1 - \frac{a_0^2}{b_0^2}) + p_0 \tag{2.7}$$

After the stress reaches p_{1y}, the material behaviour becomes plastic, and the stresses and displacement in elastic part are:

$$\sigma_r = -\frac{Yc^2}{2b_0^2}(\frac{b_0^2}{r^2} - 1) - p_0 \tag{2.8}$$

$$\sigma_\theta = \frac{Yc^2}{2b_0^2}(\frac{b_0^2}{r^2}+1) - p_0 \tag{2.9}$$

$$u = \frac{(1+v)Yc^2}{2Eb_0^2}\left[(1-2v)r + \frac{b_0^2}{r}\right] \tag{2.10}$$

The stresses in the plastic region are:

$$\sigma_r = -p_0 - \frac{1}{2}Y - YIn(\frac{c}{r}) + \frac{c^2Y}{2b_0^2} \tag{2.11}$$

$$\sigma_\theta = -p_0 + \frac{1}{2}Y - YIn(\frac{c}{r}) + \frac{c^2Y}{2b_0^2} \tag{2.12}$$

Solutions of using Mohr-Coulomb criterion for cylindrical cavity expansion in a finite medium are presented next. Like the situation before, the internal pressure increase slowly from the initial pressure p_0.

Elastic solution:

$$\sigma_r = -p_0 + (p-p_0)\left[\frac{1}{(\frac{b}{a})^2 - 1} - \frac{1}{(\frac{r}{a})^2 - (\frac{r}{b})^2}\right] \tag{2.13}$$

$$\sigma_\theta = -p_0 + (p-p_0)\left[\frac{1}{(\frac{b}{a})^2 - 1} + \frac{1}{(\frac{r}{a})^2 - (\frac{r}{b})^2}\right] \tag{2.14}$$

$$u = \frac{p - p_0}{2G(\frac{1}{a^2} - \frac{1}{b^2})}\left[\frac{1-2v}{b^2}r + \frac{1}{r}\right] \tag{2.15}$$

When the internal pressure reaches p_{1y}, material starts to yield from the internal surface.

$$p_{1y} = p_0 + \frac{(b^2 - a^2)[Y + (\alpha - 1)p_0]}{(1+\alpha)b^2 + (\alpha - 1)a^2} \tag{2.16}$$

Elastic-plastic solution:

In the elastic region:

$$\sigma_r = -p_0 + \frac{Y + (\alpha - 1)P_0}{\frac{\alpha - 1}{b^2} + \frac{1+\alpha}{c^2}}(\frac{1}{b^2} - \frac{1}{r^2}) \tag{2.17}$$

$$\sigma_\theta = -p_0 + \frac{Y + (\alpha - 1)P_0}{\frac{\alpha - 1}{b^2} + \frac{1+\alpha}{c^2}}(\frac{1}{b^2} + \frac{1}{r^2}) \tag{2.18}$$

$$\frac{c}{a} = \left\{\frac{\left[(\frac{c}{b})^2 + 1 + \frac{2}{\alpha - 1}\right](Y + (\alpha - 1)p)}{(2 + \frac{2}{\alpha - 1})(Y + (\alpha - 1)p_0)}\right\}^{\frac{\alpha}{\alpha - 1}} \tag{2.19}$$

In this equation, c is defined as the outer radius of the plastic zone.

When c=b, the whole cylinder becomes plastic, and the internal pressure is calculated as:

$$p = p_0 + \frac{Y + (\alpha - 1)p_0}{\alpha - 1}\left[\left(\frac{b}{a}\right)^{\frac{\alpha-1}{\alpha}} - 1\right] \tag{2.20}$$

The outer boundary displacement can be calculated from equation 2.21:

$$u(b) = b - b_0 = \frac{2(1-\nu^2)b\left[Y + (\alpha - 1)p_0\right]}{E\left[\alpha - 1 + (1+\alpha)\left(\frac{b}{c}\right)^2\right]} \tag{2.21}$$

The equations 2.22 and 2.23 were used to determine the value c/a and a/a_0.

$$\frac{\eta}{\gamma}\left\{\left[1 - \frac{(1+\nu)g}{\delta}\right]^{\frac{\beta+1}{\beta}} - \left(\frac{a_0}{c}\right)^{\frac{\beta+1}{\beta}}\right\} = \sum_{n=0}^{\infty} A_n^1 \tag{2.22}$$

$$A_n^1 = \begin{cases} \dfrac{(a-1)\omega^n}{an!} In\dfrac{c}{a} & \text{If } n=\gamma \\ \dfrac{\omega^n}{n!(n-\gamma)}\left[\left(\dfrac{c}{a}\right)^{\frac{(\alpha-1)}{\alpha}(n-\gamma)} - 1\right] & \text{Otherwise} \end{cases} \tag{2.23}$$

For small strain problem when r=a, the displacement can be expressed in equation 2.24:

$$\frac{u_a}{a} = \frac{\beta In\eta}{1+\beta}\left[1 - \left(\frac{c}{a}\right)^{1+\frac{1}{\beta}}\right] + \frac{(1+\nu)\left[1 + (1-2\nu)\left(\frac{c}{b}\right)^2\right]\left(\frac{c}{a}\right)^{1+\frac{1}{\beta}}}{\delta\left[(\alpha-1)\left(\frac{c}{b}\right)^2 + 1 + \alpha\right]} + \frac{\alpha\beta\omega}{\alpha+\beta}\left[\left(\frac{c}{a}\right)^{1+\frac{1}{\beta}} - \left(\frac{c}{a}\right)^{1-\frac{1}{\alpha}}\right] \tag{2.24}$$

Solution procedure is:

First, decide the suitable soil properties parameters, like E, v, C, Φ, Ψ and then choose the initial pressure p_0, the internal and external radius a_0 b_0.

Second, calculate the derived parameters: G, Y, α, β, γ, δ.

$$G = \frac{E}{2(1+v)} \tag{2.25}$$

$$Y = \frac{2C\cos\phi}{1-\sin\phi} \tag{2.26}$$

$$\alpha = \frac{1+\sin\phi}{1-\sin\phi} \tag{2.27}$$

$$\beta = \frac{1+\sin\varphi}{1-\sin\varphi} \tag{2.28}$$

$$\gamma = \frac{\alpha(\beta+k)}{k(\alpha-1)\beta} \tag{2.29}$$

$$\delta = \frac{Y+(\alpha-1)p_0}{2(k+\alpha)G} \tag{2.30}$$

Third, calculate the yielding pressure p_{1y}. If the internal pressure p is less than the yielding pressure, then calculate the expansion radius from elastic solution. If the pressure is larger than the yielding pressure, then calculate the radius from the elastic-plastic solution. When c=b, the whole cylinder becomes plastic.

2.2.3 The applications of cavity expansion theory

Cavity expansion theory has been widely applied to geotechnical problems to obtain the fundamental solutions. It is used to describe the in-situ soil testing

(cone penetrometer testing and pressuremeter testing) and to predict the behaviour of piles. It is also commonly used for the engineering solutions of deep foundations, tunnels and underground. The previous studies indicated that it is possible to apply cavity unloading solutions to conduct stability calculations for tunnels (Yu, 2000).

Tunnels have played an important role in the development of civilisation. They are underground structures having significant benefits to public transportations (Whittaker and Frith, 1990). Tunnel instability occurs from excessive displacements. In order to ensure its safety, the analysis of tunnel behaviour concerns both the stresses and displacement around an excavation and the latter's effect upon the tunnel lining (Whittaker and Frith, 1990).

Cavity expansion theory was applied to the design and construction of tunnels based on the two most important design considerations-stability and serviceability. Stability requires the tunnel to be built without causing failure. To ensure stability, it is often necessary to provide some support via linings to the internal boundary after a tunnel is excavated. To satisfy the serviceability requirement, the tunnelling-induced displacement must be small in order to avoid serious damage to the surrounding buildings and structures (Yu, 2000).

Figure 2.3 shows a horizontal cross section of an expanding cylindrical cavity in an infinite soil mass (Salgado and Prezzi, 2007). Initially, the horizontal stress is equal everywhere before the cavity is created. A plastic zone is then created after the cavity creation.

The radius of plastic zone is R. The plastic zone is bounded by a nonlinear elastic zone, which extends from R to A. The nonlinear elastic zone is bounded by a linear elastic zone. In the linear elastic zone, the shear strain is smaller than the threshold strain (typically between 10^{-6} and 10^{-4}). In this respect, soil can be assumed to behave as a linear elastic material. In the nonlinear elastic zone, the stresses have not reached the failure criterion in terms of peak strength, but the shear strains are larger than the elastic threshold strain (Salgado and Prezzi, 2007). They focused on penetration processes, which are associated with cavity creation in soil.

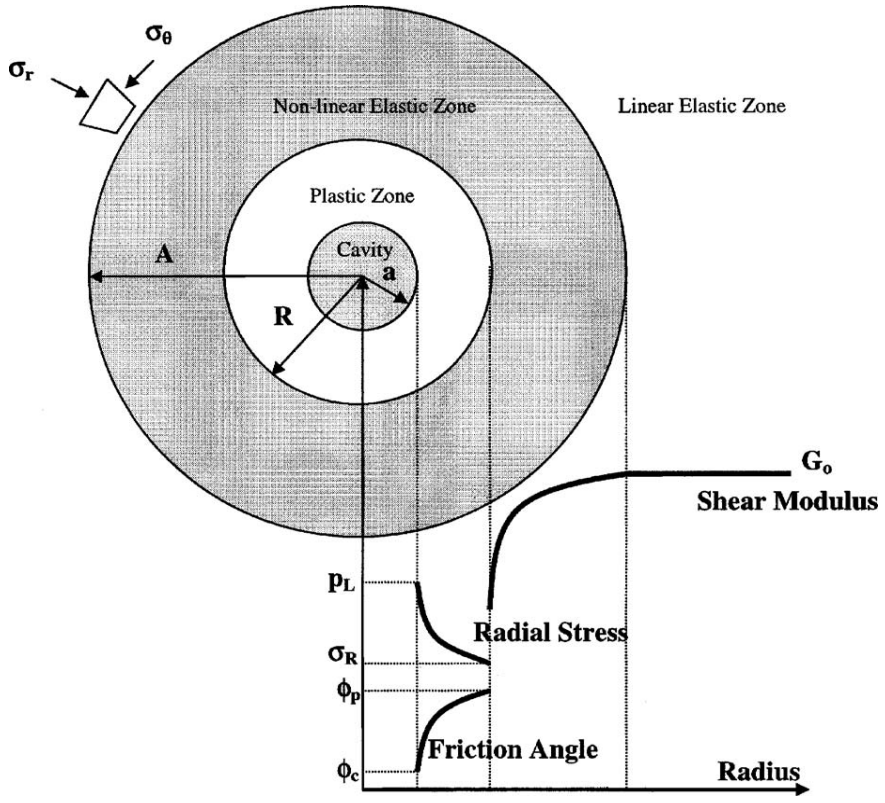

Figure 2.3: Cavity expansion: Cavity and the plastic and elastic zones (Salgado and Prezzi, 2007)

The theory of cavity expansion can be utilised in long-rod penetration mechanics which is elaborated in Rosenberg and Dekel's paper (2008). A series of 2D numerical simulations were used to describe the cavity expansion process in an elastic-plastic solid. The obtained results of strength value p_c were consistent with the analytical results. The incompressible metal critical pressure to expansion a cylindrical cavity is:

$$p_c = A_c Y \qquad A_C = \frac{1}{\sqrt{3}}\left[1 + In\frac{\sqrt{3}E}{2(1+\nu)Y}\right] \tag{2.31}$$

An analytical value of the critical pressure in a cylindrical cavity for compressible specimen can be obtained as:

$$p_c = \frac{Y}{\sqrt{3}}\left[1 + In\frac{\sqrt{3}E}{2\times 3(1-\nu)Y}\right] \tag{2.32}$$

For steel specimen, the critical pressure of cylindrical cavities in compressible solid is not far from the correct one.

The results of critical pressure for aluminium, lead and steel were shown in Figure 2.4. The results (predicted by the analytical model) for each material of compressible solid in spherical cavity expansion were also plotted in this figure. It shows that a sound consistency of results, gained through the simulation and the analytical model, was achieved. From the obtained results of the cavity wall velocity and the applied pressure in the cavity, there is an agreement between the numerical solution and the analytical models for compressible solid.

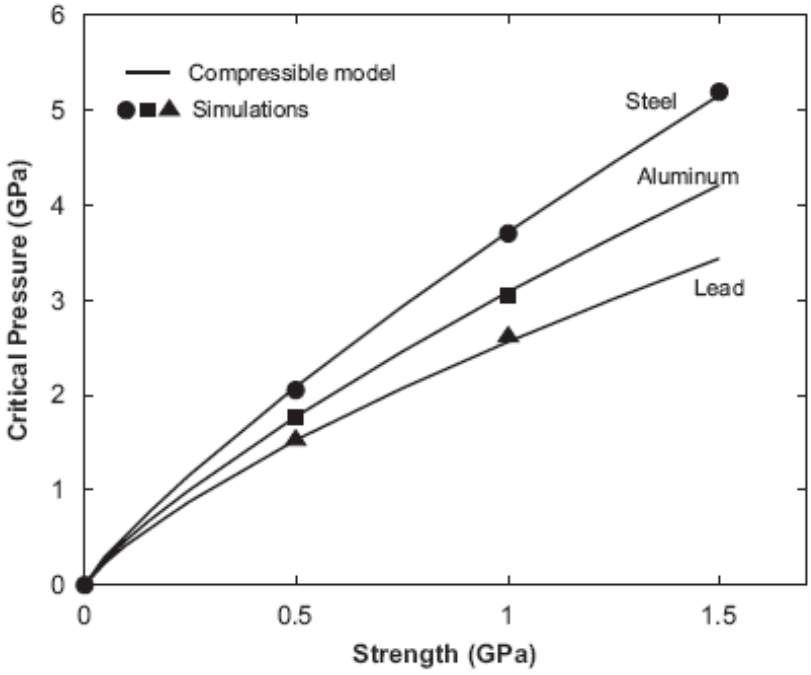

Figure 2.4: Comparison between simulation results and the analytical model for compressible steel, aluminium and lead specimens (Rosenberg and Dekel, 2008)

Undrained plane-stain expansion of a cylindrical cavity in clay was studied by Palmer (1972). In his paper, the problem of interpreting the results of Menard pressuremeter tests on soil in situ was described. Cylindrical cavity expansion by internal pressure was performed in these tests and the relationship between applied pressure and cavity volume change were measured. The condition of these tests was for undrained and saturated clay.

The condition is considered as plane strain, undrained and axially symmetric of the pressuremeter axis, the deformation is:

$$r^2 - (1 + y_1)^2 = (r - y)^2 - 1 \tag{2.33}$$

$$\text{So, } y = r - \left[r^2 - y_1(2 + y_1)\right]^{1/2} \tag{2.34}$$

The volume increase ratio is:

$$\Delta V / V = \frac{(1+y_1)^2 - 1}{(1+y_1)^2} \tag{2.35}$$

$$\text{So, } y_1 = (1-\Delta V / V)^{-1/2} - 1 \tag{2.36}$$

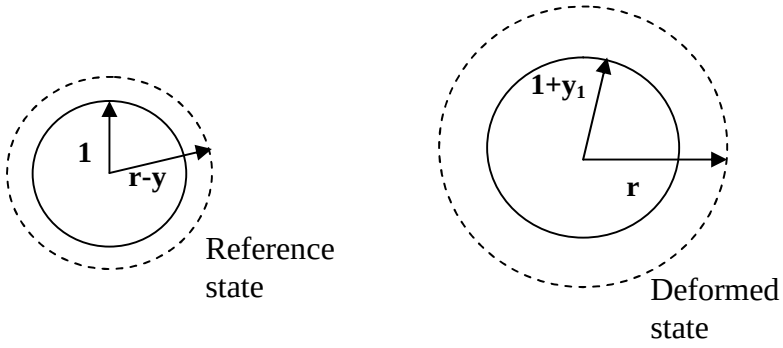

After some manipulation, the stress difference Φ is twice the gradient of Ψ (the pressure applied by the measuring cell) against $\log(\Delta V / V)$.

$$\Phi(y_1) = 2\frac{d\Psi}{d\left[\log(\Delta V / V)\right]} \tag{2.37}$$

Use of cavity expansion to analyse the sand behaviour was developed by Salgado and Randolph (2001). The relationship between shear and volumetric strain of variations relative density and stress state in the plastic zone was described. The fully non-linear soil response was considered in this analysis of sand. This research can be used to evaluate the soil variable in plastic zone during the expansion and determine the limit pressure. The cavity expansion-strain curve also can be obtained.

Figure 2.5 shows how R/a varies with relative density and initial effective stress state in sand for cylindrical cavity expansion. The properties for sand in this figure are g_r= 0.68, C_g=612, e_g=2.17, n_g=0.44, Q=9, R_q=0.49, e_{min}=0.48, e_{max}=0.78, v=0.15, and φ_c=33. These parameters are those of Ottawa sand (Salgado et al., 2000). The results show that the ratio of plastic to cavity radius R/a under limited conditions increased with increasing the dilatancy. Limit pressure increased when the lateral stress increased.

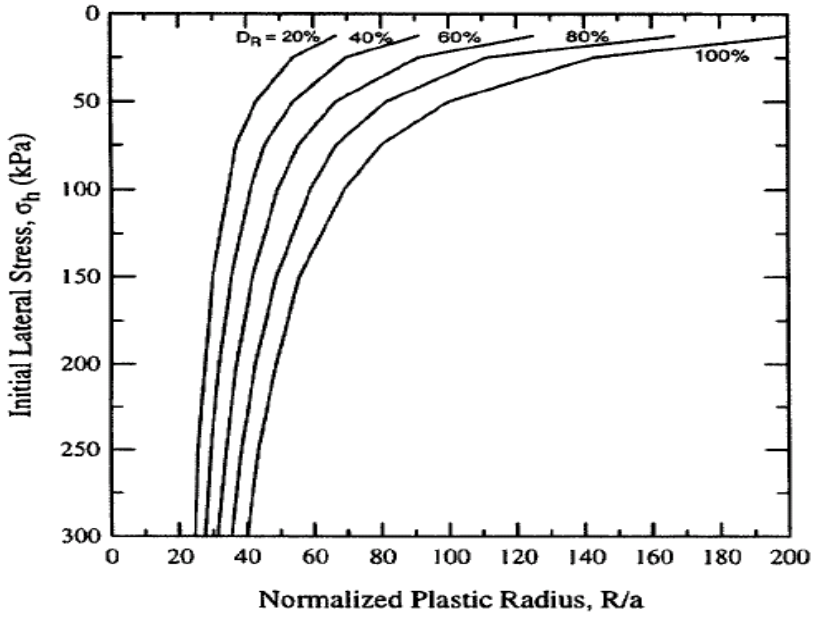

Figure 2.5: Normalized plastic radius (ratio of plastic to cavity radius) at limit condition as a function of initial soil state (Salgado and Randolph, 2001)

2.3 The Interpretation of In Situ Soil Tests

Pressuremeters and cone penetrometers are two most widely used instruments for the measurement of soil properties in-situ. The first method accurately measures the stiffness and strength of soil, while the second method can be used to obtain approximate soil profiles quickly. The theory of cylindrical

cavity expansion has been adopted as the most important interpretation method for self-boring pressuremeter tests in soil and rock (Clarke, 1995). The cone tip resistance in the cone penetration test has been predicted properly using spherical cavity expansion (Yu and Mitchell, 1998).

2.3.1 Pressuremeter test

A pressuremeter is defined here as cylindrical probe designed to apply uniform pressure to the wall of a borehole by means of an expandable flexible membrane. When a pressuremeter test is carried out in soils, the measured pressure displacement curve can be used to back-calculate the mechanical properties of soils (Yu, 2000).

In Mair and Wood's paper, the pressuremeter test (PMT) is considered as placing a cylindrical probe in a pre-drilled hole and expanding this probe while measuring changes in volume and pressure in the probe. A limited pressure can be estimated from the reading and a pressure meter modulus can be calculated from the reading of pressure-volume changes during the test. Presuremeters are normally installed vertically at various depths in the ground, and they are connected by tubing or cables to a control unit at the ground surface (Mair and Wood, 1987).

The main advantages of the pressuremeter test are (1) the boundary conditions are easy to define; (2) this test can measure the deformation and the strength at the same time; (3) the self-boring pressuremeter test gives a closest approach to undisturbed soil of other tests (Yu and Collins, 1998). They considered the

pressuremeter as cylindrical cavity expansion process and the effective stress analysis was described.

Finite strain analysis of pressuremeter test was presented by George et al. (1990). The pressuremeter test was considered as plane strain problem in their study. The assumptions of this analysis included plane strain, small strain and rigid perfectly plastic constitutive models of the Mohr-Coulomb type. From the plot of cavity pressure and expansion strain, it can be seen that a “steady state” condition was reached by reducing the stiffness and the parametric. The factors to affect the soil characteristics were evaluated in this paper (George et al., 1990).

The procedure of pressuremeter tests in sand was described by Juran and Mahmoodzadegan (1989). In this paper, a new approach for interpretation of pressuremeter tests to determine the shear strength characteristics, dilatancy properties and shear modulus was described. An elastic-plastic strain hardening soil model was developed in the dilating behaviour during the pressuremeter cavity expansion. The correct engineering properties of sand in the cavity expansion test were correlated with the conventional triaxial compression tests. It can be noted that the peak friction angle and dilation angle of plane strain cavity expansion tests were slightly higher than the conventional triaxial tests.

Antonio (1990) presented the application of pressuremeter test and the radial expansion of cylindrical cavities in sandy soils. A solution of radial expansion of cylindrical cavities was developed in his paper and the rigid-plastic model was used in his research. The curve of the friction angle mobilized at each step of the test deformation can be obtained from this solution and also some

discussion about the value of the friction angle was mobilized at the critical voids ratio. The rheological behaviour of a sand medium during the cylindrical cavity expansion was explained in his research.

Measurement of shear stiffness in pressuremeter tests in municipal solid waste was described by Dixon et al. (2006). This paper presented the results from a programme of pressuremeter tests which was modelled in municipal solid waste. Shear stiffness properties were measured as well. From the results, it has been shown that a strong relationship between shear modulus and depth from the unload-reload loops can be obtained. It can be seen that there is a good agreement between shear stiffness values calculated from small strain in pressuremeter tests and shear stiffness values measured using the continuous surface wave method in their research.

A finite element analysis of the cone pressuremeter test in sand was presented by Houlsby and Yu (1990) and the test was considered as the cylindrical cavity expansion in a Mohr-Coulomb material. In their paper, a method to obtain the strength parameters was developed and cavity expansion theory was applied to explain this test. Another analysis of self-boring pressuremeter test using the same finite element method was described later by Yu and Collins (1998). The material was considered as overconsolidated clays in this paper.

2.3.2 Cone penetration test

The cone penetration test (CPT) is an in situ testing method used to determine the geotechnical engineering properties of soil. The early application of CPT was to determine the soil bearing capacity. Most notably, limit pressure was

calculated in a much more effective way and a new formulation for calculating cone resistance from cavity limit pressure (which considers the true interface friction angle between the cone and soil) has been developed and implemented (Salgado and Prezzi, 2007).

The cone penetration test is an axisymmetric problem and the mechanism is related to the cavity expansion (Huang and Ma, 1994). A series of simulations were carried out in his research and it allowed the cone penetration test to be considered in the microscopic analysis. The results show that the loading history has the effect on the characteristics of soil failure and dilatancy, but later stress behind the cone base is not sensitive with the soil history. For the graded sand, the crushing is easy to occur in the small particles. Moreover, the cone resistance analysis is linked to the classical cavity expansion theory based on linear elasticity and perfect plasticity. These analyses would produce substantially the same values of cavity expansion limit pressure as the present theory (Salgado and Prezzi, 2007).

In Jiang et al.'s paper (2006), a two-dimensional discrete element method was used to simulate the deep penetration tests on granular materials. The effect of soil-penetrometer interface friction was discussed in their paper and it has been proved to affect the actual penetration mechanisms very much. The results show that the soil near the penetrometer has a complex displacement path in deep penetration. The penetration depth and tip-soil friction result an increasing tip resistance. The penetration leads to high gradients of displacement and velocity fields. The soil near the penetrometer has a loading, unloading process and the large rotation of principal stresses (like 180^{o}), as

well as high gradients of both the value and direction of stress can be observed. In the penetration, the soil of large deformation (when it arrive the stress state) has a little higher strength than that of the conventional tests.

2.4 Mechanics of Granular Material

Granular materials consist of individual particles in contact and interstitial voids, so that they generally comprise a multiphase media of solid, liquid and gas, and sometimes appear to behaviour as fluids or solids. However, the behaviour of granular material is more complicated than that of a fluid or a solid. The discrete characteristics of the granular material result in complex behaviour under different loading conditions.

2.4.1 Granular materials behaviour

In a granular medium composed of discrete particles, forces are transferred only through the interparticle contacts. The discrete nature makes the constitutive relationship very complex. The micromechanical behavior of granular materials is therefore inherently discontinuous and heterogeneous. If friction does not occur at the contact points, the material cannot sustain applied shear forces. Some overall resistance to the applied force is generated by the so-called interlocking effect of particles (Scott, 1963). The movement of particles takes place as the result of sliding and rolling at contact points, leading to the macro-deformation. The macroscopic properties of these materials are obviously related to the basic structure and properties of their constituents and their interactions (grains and voids).

2.4.1.1 Internal friction angle

The physics of friction behaviour has been studies for several decades. There is no doubt that the friction at the contact point plays a dominant role in controlling the macro-deformation and strength of granular materials. The Coulomb's friction law was used to explain the relation between the frictional force F_τ and the normal force F_σ:

$$F_\tau = \mu F_\sigma = F_\sigma \tan\phi_\mu \tag{2.38}$$

Where, μ, Φ_μ are physical constants called frictional coefficient and the interparticle friction angle respectively. Experiments show that this coefficient of friction drops when motion begins (the kinematic friction coefficient is less than the static friction coefficient).

In fact, for granular materials, the internal friction angle Φ has a different physical meaning compared to inter-particle friction angle Φ_μ. The internal friction angle is not a physical constant for a given soil but strongly dependent on the void ratio, fabric, stress states and other parameters. This angle is low when grains are smooth or rounded, and it is high for sticky, sharp or very fine particles. Typically, the value of this angle is between 15°-45°.

2.4.1.2 Stress tensor

In the three-dimensional space with a Cartesian coordinate system, we can write the total stress tensor for a frictional granular material as:

$$T = \begin{bmatrix} \sigma_{xx} & \tau_{xy} & \tau_{xz} \\ \tau_{yx} & \sigma_{yy} & \tau_{yz} \\ \tau_{zx} & \tau_{zy} & \sigma_{zz} \end{bmatrix} \tag{2.39}$$

Where $\sigma_{xx}, \sigma_{yy}, \sigma_{zz}$ represents the normal stress acting on the YOZ, XOZ and XOY planes respectively, τ_{xy}, τ_{xz} are the shear stresses acting in the Y-direction and Z-direction respectively on the plane YOZ (whose normal is X), τ_{yx}, τ_{yz} are the shear stress in the X-direction and Z-directions respectively acting on the plane XOZ (whose normal is Y), and τ_{zx}, τ_{zy} are the shear stress in the X direction and Y direction acting on the plane XOY (whose normal is Z).

Consider a closed continuous domain, with volume V loaded on its boundary S by a distributed force $t_i(x)$. Depending on the loads, a stress tensor $\sigma_{ij} = \sigma_{ij}(x)$ belongs to every point of the domain satisfying the boundary condition of $\sigma_{ij} n_j = t_i$ where n_i is the outwards unit normal vector on S. The volume average of the stress tensor ($\overline{\sigma_{ij}}$) can be expressed with the help of the Gauss-Ostrogradski theorem as a surface integral

$$\overline{\sigma}_{ij} = \frac{1}{V} \iiint_V \sigma_{ij} dV = \frac{1}{V} \iint_S x_i t_j dS \tag{2.40}$$

Where x_i is the position vector on the surface S.

There are concentrated forces instead of the distributed loads acting on the boundary of the domain and between the sub-domains, the above expression

can be written in a discrete form. Let f_i^k be the forces acting at the boundary points x_i^k (k=1, 2, …). Then the average stress Equation is modified as

$$\bar{\sigma}_{ij} = \frac{1}{V} \sum_{k \in S} x_i^k f_j^k \tag{2.41}$$

Where the index k runs over the external loading forces.

2.4.1.3 Shear and deformation

There are normal stress and shear stress both in the geotechnical construction. The normal stresses cause volume change due to compression or consolidation. The shear stresses prevent collapse and help to support the geotechnical structure. Failure will occur when the shear stress exceeds the limiting shear stress (strength). Shear strength is a material property, which enables soil to maintain equilibrium on an inclined surface, such as a natural hillside or the sloping sides of an embankment or earth dam.

When a granular soil is sheared, homogeneous deformation first takes place. The elastic strain is dominant at the beginning and is gradually replaced by the plastic strain. Around a peak stress, the deformation suddenly localizes into narrow zones (called shear bands), and stress drops sharply to a residual stress state. The shear strength characteristics of sand can be determined from the results of either drained triaxial tests or direct shear tests. A soil consists of discrete particles and its fabric changes easily when subjected to overall shear distortion. Volume expansion during shear (called dilatancy) is an indication of

such changes, and is one of the most interesting aspects in the mechanics of granular media. There is a good reason to believe that external work done is dissipated through sliding at contact points during non-recoverable deformation. The experimental obtained relation between dilatancy and mobilized shear strength in a granular soil on the assumption that sliding is a major micro-deformation mechanism. This method has been discussed by many engineers, and also has proposed various possible sliding models to interpret it.

In a dense sand, there is a considerable degree of interlocking between particles. Before shear failure can take place, this interlocking must be overcome the frictional resistance at the points of contact. During shearing of a dense sand, the macroscopic shear plane is horizontal, but sliding between individual particles takes place on numerous microscopic planes inclined at various angles above the horizontal as the particles move up and over their neighbours. Rowe (1962) developed a stress-dilatancy theory relating the ratio of the principal stresses, the geometry of ideal particle and the relative rates of change of volumetric and major principal strains. It was shown that:

$$\frac{\sigma_1^{'}}{\sigma_3^{'}} = \left\{ \tan^2\left(45° + \frac{\phi_f^{'}}{2} \right) \right\} \left(1 - \frac{d\varepsilon_v}{d\varepsilon_1} \right) \tag{2.42}$$

Where $d\varepsilon_v$ and $d\varepsilon_1$ are corresponding small changes in volumetric and major principal strain respectively (compressive strain being taken as positive) and $\phi_f^{'}$ is a value of angle of shearing resistance between the limits of ϕ_μ and $\phi_{cv}^{'}$ depending on the strain conditions imposed by the test. The value of $\phi_f^{'}$ is a

function of the instantaneous directions of local interparticle slip as rearrangement takes place (the preferred directions of local slip would be at $(45°+\Phi_\mu/2)$ to the major principal plane).

2.4.2 The properties of granular material

It is well known that the mechanical behaviour of granular material is affected by a lot of factors, such as distribution of particle size and particle shape. Discrete element method has been used in the recent work which gives a unique opportunity to obtain the properties of granular material from the micro level.

2.4.2.1 Dynamic properties

Dynamic response of the granular materials has the relationship with the parameters of shear modulus and damping ratio. The study using triaxial stress state to investigate dynamic response was developed by Dinesh et al. (2004). The shear modulus G was obtained by using Young's modulus E and Poisson's ratio μ.

$$G = \frac{E}{2(1+\mu)} \tag{2.43}$$

The damping ratio D (in Equation 2.44) was measured from the hysteresis loop as shown in Figure 2.6:

$$D = \frac{A_L}{4\pi A_T} \tag{2.44}$$

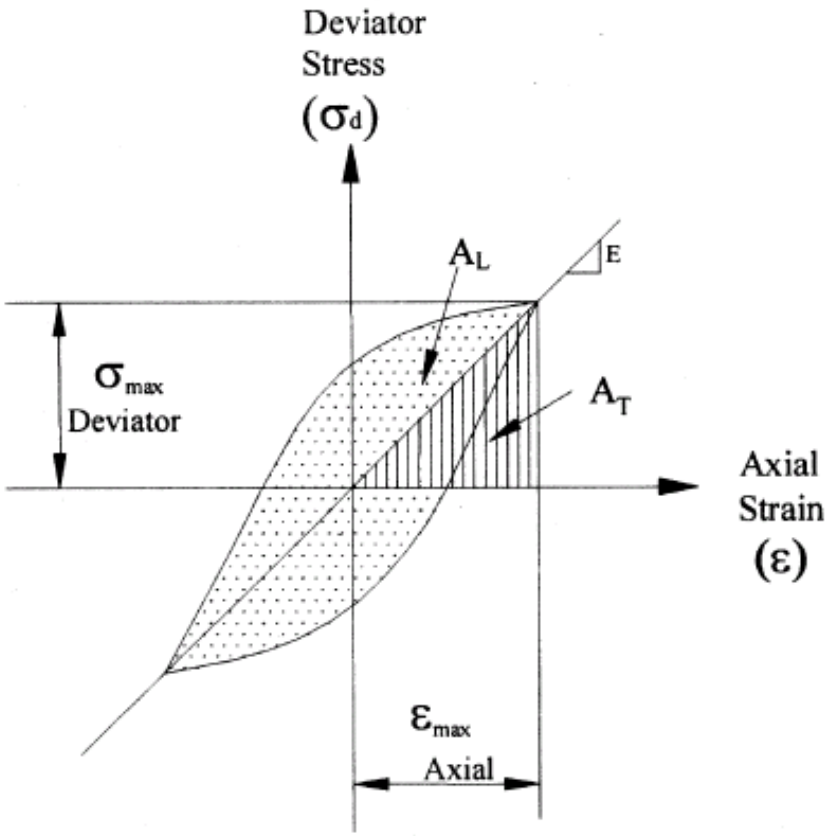

Figure 2.6: Hysteretic stress-strain relationship (Dinesh at el., 2004)

Figure 2.7 shows the relationship between the shear modulus and shear strain for different confining pressure and Figure 2.8 shows the normalized shear modulus versus shear strain with the confining pressure same as the Figure 2.7. The damping ratio versus shear strain has been shown in Figure 2.9. It can be seen that the larger damping can be obtained under the low confining pressure and damping increased with the reducing confining pressure at any shear strain level. For the same confining pressure, the damping increased when the shear strain increased. From all the results in Figure 2.7, 2.8 and 2.9, it has been improved that they have a good agreement with the experimental results of Kokusho (1980) and Yasuda and Matsumoto (1993).

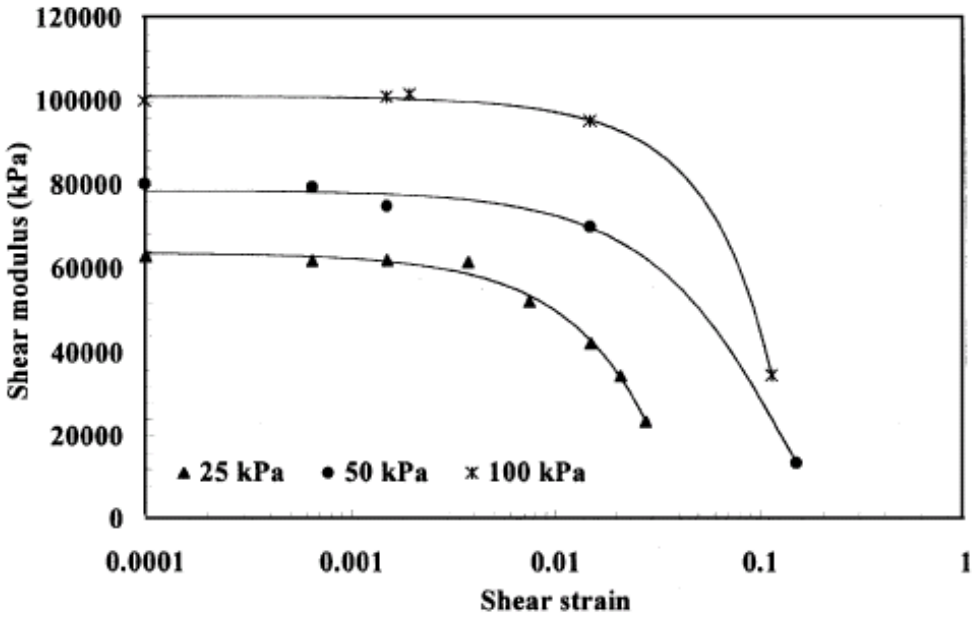

Figure 2.7: Shear modulus versus shear strain (Dinesh at el., 2004)

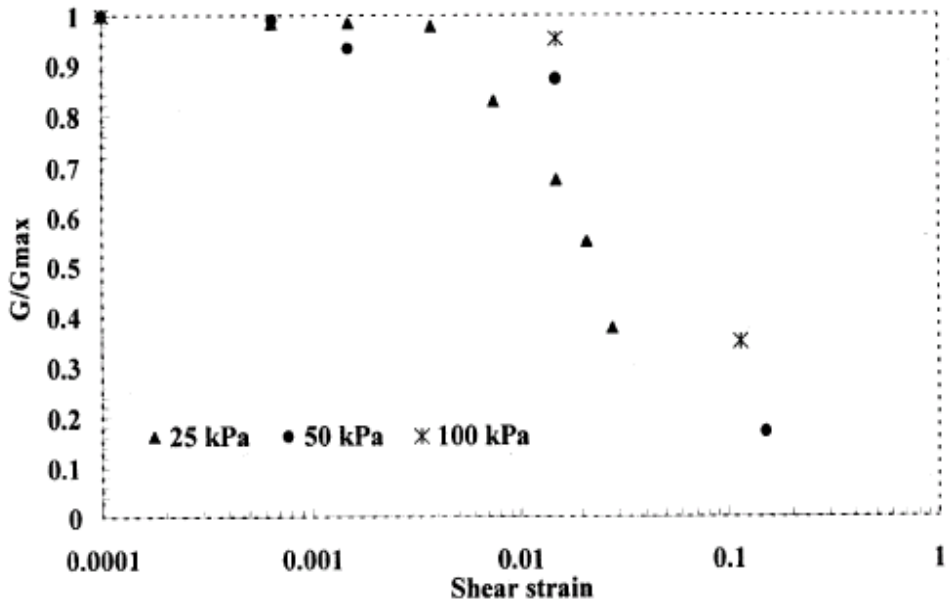

Figure 2.8: Normalized shear modulus versus shear strain for different confining pressure (Dinesh at el., 2004)

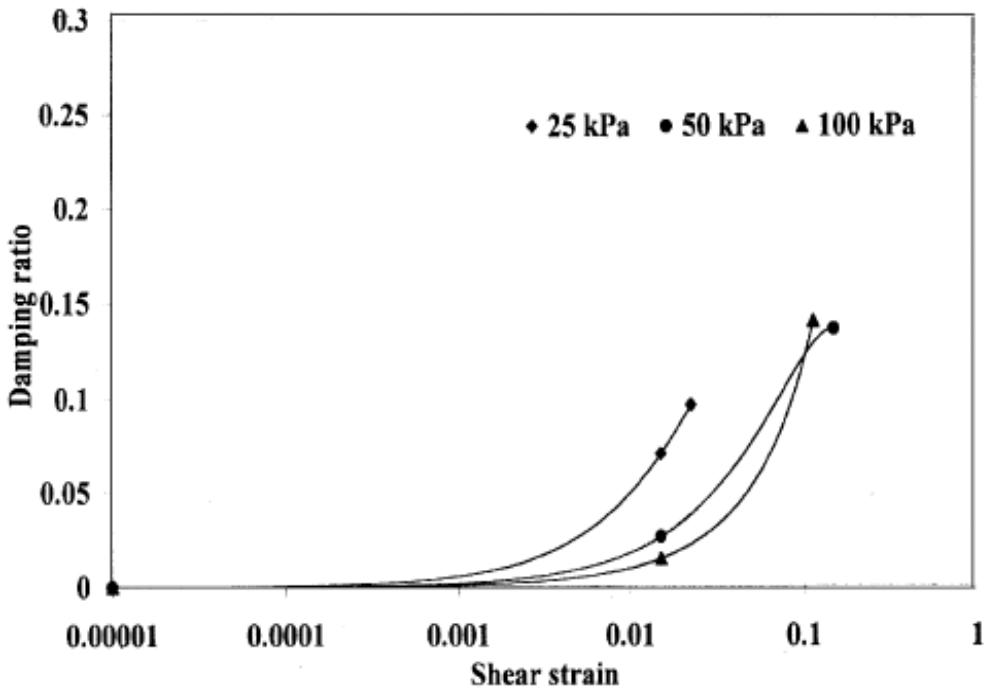

Figure 2.9: Damping ratio versus shear strain (Dinesh at el., 2004)

2.4.2.2 Yielding of granular materials

McDowell and Bolton (1998) examined that the micro mechanics of soils was subjected to one-dimensional compression. Figure 2.10 shows the plot between voids ratio and the logarithm of vertical effective stress for sands (Golightly, 1990). At low stresses in region 1, the behaviour was quasi-elastic for the dense silica sand and small irrecoverable deformations may occur because of particle rearrangement. Region 2 was described as yielding for soil subjected to one-dimensional compression, and major plastic deformation occurs beyond this region.

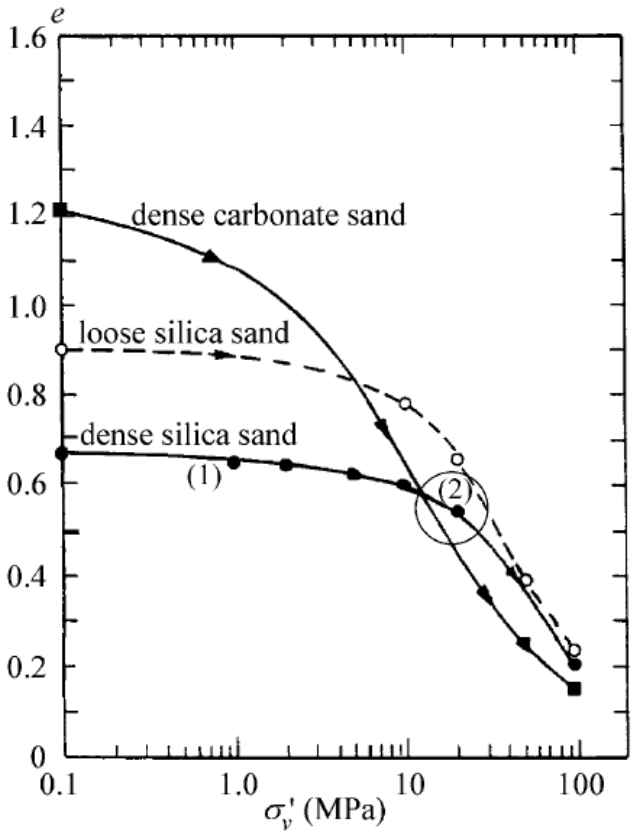

Figure 2.10: One-dimensional compression plots for carbonate and silica sands (Golightly, 1990)

Although not all particles are loaded in the same way, it may be assumed that all particles will eventually be in the path of the columns of strong force that transmit the macroscopic stress. Cundall and Strack (1979) showed that the applied major principal stress was transmitted through columns of strong force in the discrete element method numerical simulation, as shown in Figure 2.11**.** McDowell and Bolton (1998) proposed that the yield stress must be proportional to the average tensile strength of grains. They defined yielding stress as a value of macroscopic stress which caused maximum rate of grain fracture under the increasing stress and the value of yielding stress could be measured by crushing between flat platens.

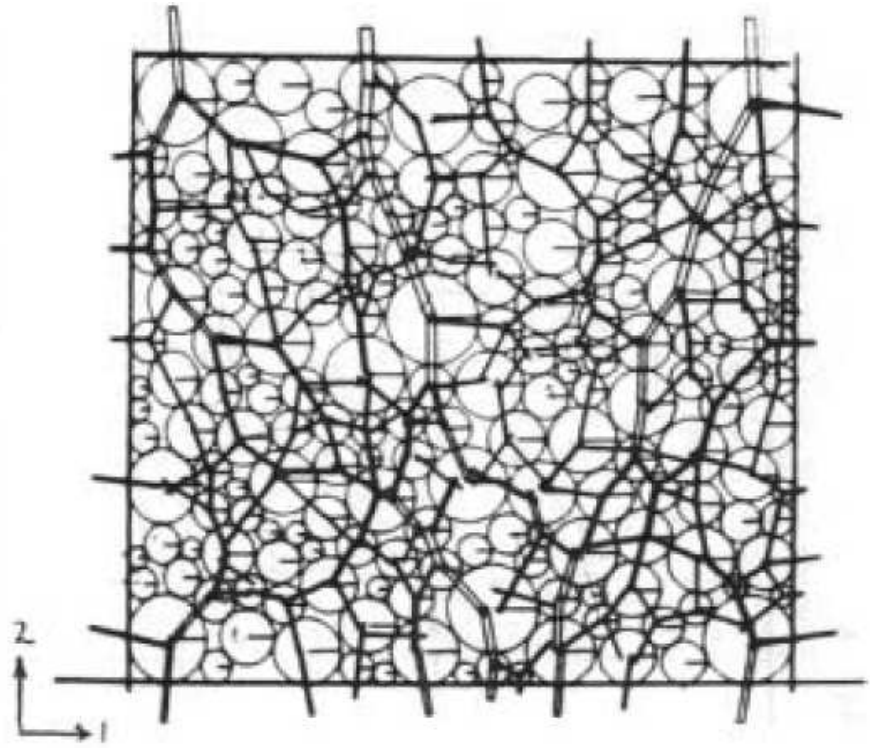

Figure 2.11: Discrete element simulation of array of photoelastic discs (Cundall and Strack, 1979)

One-dimensional normal compression tests on densely compacted silica sand of uniformly-graded samples have been described by McDowell (2002). An analysis of the yielding and plastic hardening of the material has been developed and the results of these tests were shown in Figure 2.12. It is obvious that the stress level in the yielding region depended on the initial grain size and it increased with reducing particle size. In these tests, the initial voids ratio was approximately same for each aggregate. All particles had similar angularity and the same compacted way was used to obtain the maximum density of sample.

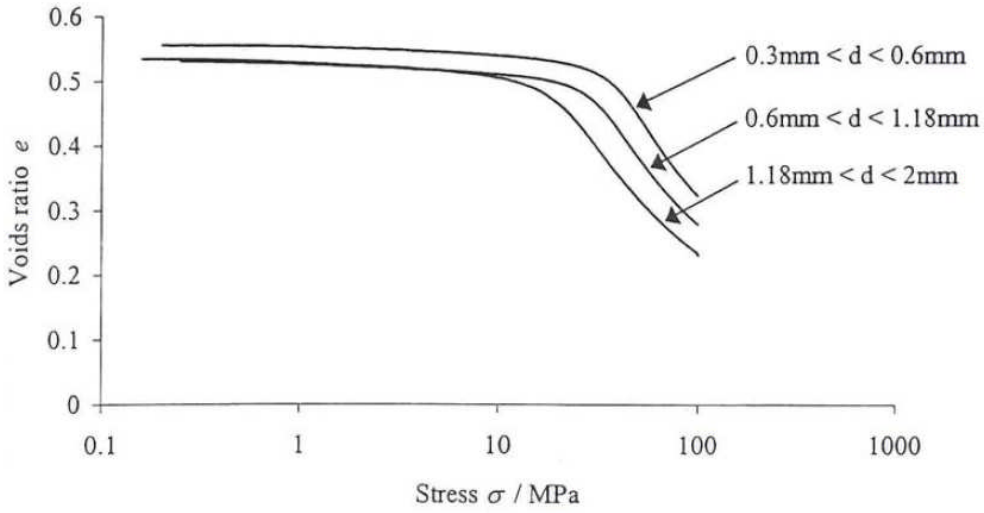

Figure 2.12: Compression plots for different uniform gradings of sand (McDowell, 2002)

McDowell (2002) described that the applied major principal stress was only transmitted through two or three columns of strong force for an array approximately 12 particles wide. Aims to predict the yield stress of the aggregate as ¼ of the 37% tensile strength of the constituent grains in the aggregate, a simple estimation (the induced characteristic stress in the particle forming the columns of strong force should be four times as the applied macroscopic stress) was used. The results were shown in Figure 2.13, it can be seen that the yield stress was predicted well and the proposition of this further strengthens statements (yields stress should be proportional to the tensile strength of the individual grains) was made by McDowell and Bolton (1998).

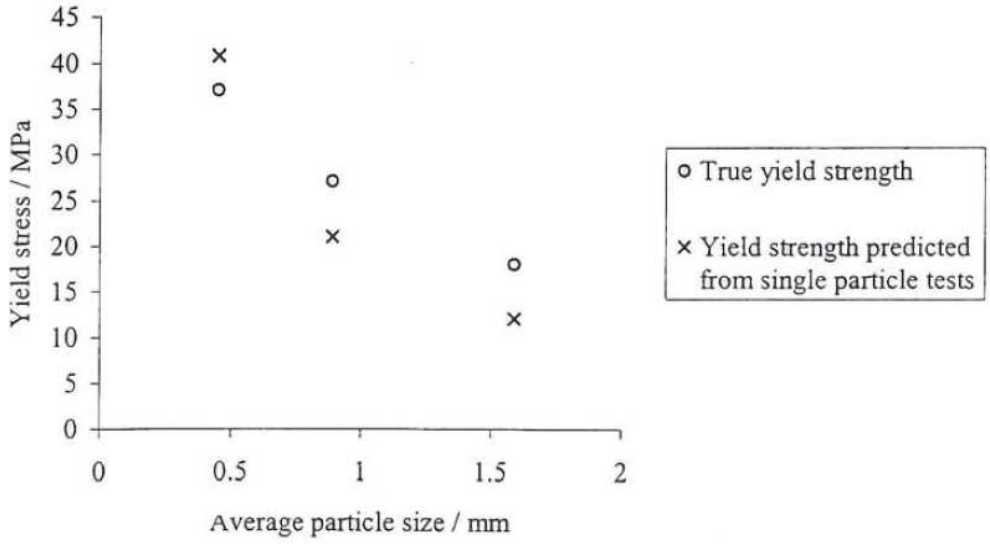

Figure 2.13: Yield stress predicted from single particle crushing tests, assuming yield stress= (37% tensile strength)/4 (McDowell, 2002)

2.5 Summary

Cavity expansion processes are operative in a number of problems in soil mechanics; including pressuremeter testing, cone penetration testing. These problems can be solved by a finite-difference technique using cavity expansion theory. A description of soil behaviour can be achieved by developing a constitutive model and a satisfactory technique for measuring the required soil properties is described. The discrete nature of granular material such as sand makes the constitutive relations very complex, and also the behaviour of granular material is complicated. The development and applications of cavity expansion, as well as the mechanical behaviour of granular material were discussed in this chapter.

CHAPTER 3

DISCRETE ELEMENT MODELLING OF GRANULAR MATERIAL

3.1 Introduction

Granular materials are composed of distinct particles that can displace independently from each other and interact only at contact points. The discrete nature of the granular material results in complex behaviour under conditions of loading and unloading. Although examples of granular materials exist around us, until now there is no widely accepted constitutive model describing the behaviour of these materials. The granular materials are particulate in nature and sustain loads mainly by interparticle friction, such as sand, powers gravel (Sitharam and Dinesh, 2002). Their constitutive behaviour is complicated and a lot of tests are needed to understand the soil behaviour before modelling.

It is well know that the test conditions and particle size distribution can affect the constitutive behaviour of granular materials (Sitharam and Nimbkar, 2000). However, it is difficult to model the particle size and gradation effects using continuum mechanicals based models. From the work of Cundall and Strack

(1979), the discrete element method (DEM) is widely used to study the behaviour of granular materials and provides a way to investigate the mechanic properties of granular material at both microscopic and macroscopic level. In DEM, the interaction of the assembly's particles is viewed as a transient problem with states of equilibrium developing whenever the internal forces balance.

Model for stress-strain behaviour of granular material with microstructural consideration can be derived from properties of inter-particle contacts. Each particle is identified by properties such as normal stiffness, shear stiffness, friction coefficient and adhesion. The discrete element modelling is allowed to investigate some features of granular materials which are not easily measured in laboratory tests, such as interparticle friction and distribution of contact forces. It is also possible to use the same sample for different loading conditions, so the material properties (the distribution of contact forces and the internal particle structure) and the effect of loading conditions can be investigated independently. Granular materials are modelled as packed assemblies of discrete elements in DEM. In this chapter, the background and development of DEM is presented. The concepts and the development of DEM are introduced in Section 3.2. Section 3.3 presents the application of discrete element modelling of granular materials and some literature reviews of discrete element modelling. In section 3.4, discrete element program PFC^{3D} (a simplified implementation of DEM) is described. In this thesis, a popular numerical technique (DEM) is used to apply on the cavity expansion simulations in granular materials.

3.2 Introduction to the Discrete Element Method

Granular media such as sand composed of discrete particles exhibit very complex macroscopic mechanical responses to externally applied loading. DEM is an alternative view of granular materials to investigate their mechanical behaviour at the microscopic level. DEM was first developed by Cundall (1971) for rock mechanics applications and is being increasingly used to simulate the mechanical behaviour of granular materials (Cundall and Strack, 1979; Ting et al., 1989; Rothenburg and Bathurst, 1992). DEM provides the possibility of investigating the mechanical behaviour of granular materials at both micro and macro levels. Some researchers developed a numerical quasi-static model for granular media based on displacement methods of structural mechanics and finite element method (FEM). However, this method is not able to follow large displacement and rearrangements which are fundamental characteristics of state changing processes of granular media. DEM is better in modelling a discontinuous material than other numerical tools such as FEM and BEM (boundary element method). It considers the particle-scale interaction, allowing the micro-mechanics of soil response to be analysed in detail. In DEM, the interaction of the discrete particles is monitored contact by contact and the motion of the particles is modelled particle by particle.

DEM numerical simulations become a valuable tool in the study of different phenomena occurring at the micro mechanical behaviour in granular materials. DEM provides a virtual laboratory that allows the modeller to perform experiments which are difficult or impossible to undertake in a physical laboratory. The DEM is primarily used to study the fabric and structure of

granular materials under loading and gives the contribution on developing the constitutive relations for soil using disks and spheres (Bathurst and Rothenburg, 1988; Zhang and Cundall, 1986; Oner, 1984). Recently, Lorig and Brady (1984) have developed the DEM on the application of stress around tunnel openings. Cundall and Hart (1992) gave a summary on fundamental aspects of discrete element modelling systems and defined the scope of DEM. DEM allows finite displacements and rotations of discrete bodies including complete detachment, and recognises new contacts automatically as the calculation progresses.

In DEM, the contact forces and displacements of a stressed assembly of particles are found by tracing the movements of the individual particles. The particle interactions are considered as a dynamic process with states of equilibrium developing whenever the internal forces are in balance. The dynamic interaction of a particle assembly is treated by using an explicit time-stepping scheme. Specified walls, particle motions and body forces controlled the particle system of distribution. Damping is one of the most important calculation parameters in the DEM since the movements of soil particles are irreversible. If there is kinetic energy in the system, simple harmonic motion will be occurred around the equilibrium position without damping. Damping must be applied at the system to evanesce the kinetic energy from the action.

The idea of explicit finite-difference method for continuum analysis is treated as the heart of most DEM simulations. However the timestep is so small and the disturbances cannot propagate from any particle further than its immediate neighbours in a single timestep. So the interaction of particles determines the forces acting on any particle. Discrete element modelling can accurately

replicate the behaviour of real assemblies at the particle scale by simulating the motion of individual grains. A sufficient number of particles are required in the simulation for getting the accurate macroscopic stress and strain relationship. In the DEM calculation, velocities and accelerations are assumed constant in each timestep and the dynamic behaviour is represented numerically by a timestepping algorithm.

The calculations in DEM are based on two laws: Newton's second law on the particles and a force-displacement law at the contacts. Newton's second law is used to calculate the motion of each particle arising from the contact and body forces acting upon it. While the force-displacement law is used to get contact force from displacement and update the contact forces arising from the relative motion at each contact. The interparticle forces are renewed at each time step, which is computed from the relative velocities at the contacts (the force-displacement relation). Then the new out-of-balance force at each contact is determined and used to calculate the new translational and rotational of particle accelerations (Newton's law of motion) after updating the interparticle force. Integration of the particle accelerations provides the particle velocities and then the displacements of each particle are obtained. After that new particle position is determined by using the updated velocities at the contacts, the process will repeat. The DEM approach involves two separate scales: the macro-scale on continuum properties of the assembly and the micro-scale on particle-scale properties.

The calculation repeated of force and displacement is given here:

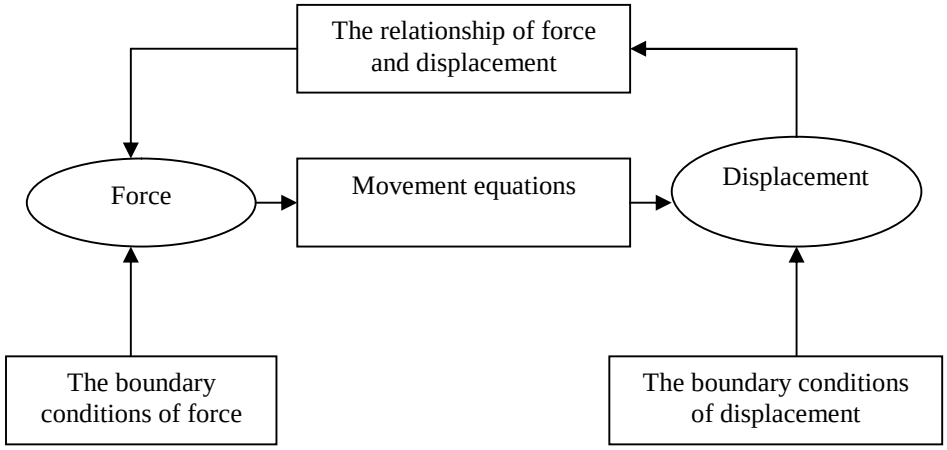

3.3 Influence of particle properties

DEM is a numerical method using assemblies of discs or spheres to describe the mechanical behaviour of granular material. It has been improved to be a valid and fundamental tool for the research of granular behaviour. DEM has been frequently used in the research during the past two decades with the computational capacity development. It is widely used to investigate the behaviour of a granular mass from a micromechanical level. The effects of micro-properties on the mass behaviour are very important and DEM supplies a useful tool for research on this point.

3.3.1 Particle shape of circular/spherical or non-circular/spherical

In the early discrete element analysis, the particle is used as circle element to obtain the results from the two-dimensional simulations (Cundall and Strack, 1979). A large number of problems can not be modelled just using the two-

dimensional simulations in practical situation, so spherical particles are widely used in the simulations recent years. Much more information and published works were obtained from the three-dimensional simulations. Normally, natural grains (like the sands and gravels) have irregular shapes, so similar shape is required in the recent research on DEM simulation. If the sample is filled with non-spherical particles, the more interlocking and moment resistant will be induced. The problem of circle and spherical particles rolling in the simulation has been presented by Bardet and Proubet (1991). The biaxial test was simulated using disks with three different radiuses in DEM (Ting et al., 1989). They noted that the internal friction angle obtained from the simulation was lower than the calculation from real sand and particle rotation plays an important role in the strength and deformation of materials. Santamarina and Cho (2004) explained that the size and shape of particles reflect the composition of material and play a significant role in soil behaviour. Particle shape is a very important parameter to determine the soil characterization, including sphericity, angularity and roughtness. Simulation using circular or spherical particles is too idealized to capture the characteristic of soil behaviour.

Frossard (1979) presented that the shape of particles also have a significant effect on the volume strain, especially in the maximum angle of dilation. Many researchers focus on the shape of the particle to get more reliable results. Favier et al. (1999) described that particle shape is very important to get the real particle behaviours. The earliest DEM were performed on two-dimensional problem and the shape was considered as either circular or polygonal. Detailed information of individual particle-particle contact is required for models using discrete elements (Cundall and Strack, 1979; Drake and Shreve, 1986; Hogue

and Newland, 1994; Walton, 1983). Later researchers developed the DEM to three dimensional condition using spheres and polyhedra particle with the addition of ellipses. The actual shape of granular material (like ellipsoid) in the DEM has been developed by many researchers (Lin and Ng, 1997). A new method of representing non-spherical, smooth-surfaced, axisymmetrical particles in discrete element modelling has been presented by Favier et al. (1999). The Multi-element particle model is described. This particle was constructed of spheres whose centres are located on the axis of symmetry. The two spheres are fixed to be one particle. Figure 3.1 shows the contact of two particles, each particle has two spherical elements with identical diameters. The global position of each particle is determined at its centroid by its global position vector $r_{p(G)}$. The relative position vector between the particle centroid and the centre of an element sphere d_{ps} is prior known because the position of each sphere within a particle is determined in advance. Figure 3.2 shows how to transfer the force between the element spheres and particles. The total moment for the centre of an element sphere due to tangential forces is

$$M_{t_{ps}} = \sum_{c=1}^{c} (r_{psc} \times f_{t_{psc}}) \tag{3.1}$$

where $f_{t_{psc}}$ is the tangential component of the contact force at contact point c and C is the total number of contact points on each sphere at the current timestep, as shown in Figure 3.2a. Each element sphere resultant contact force is

$$f_{ps} = \sum_{c=1}^{c} f_{psc} \tag{3.2}$$

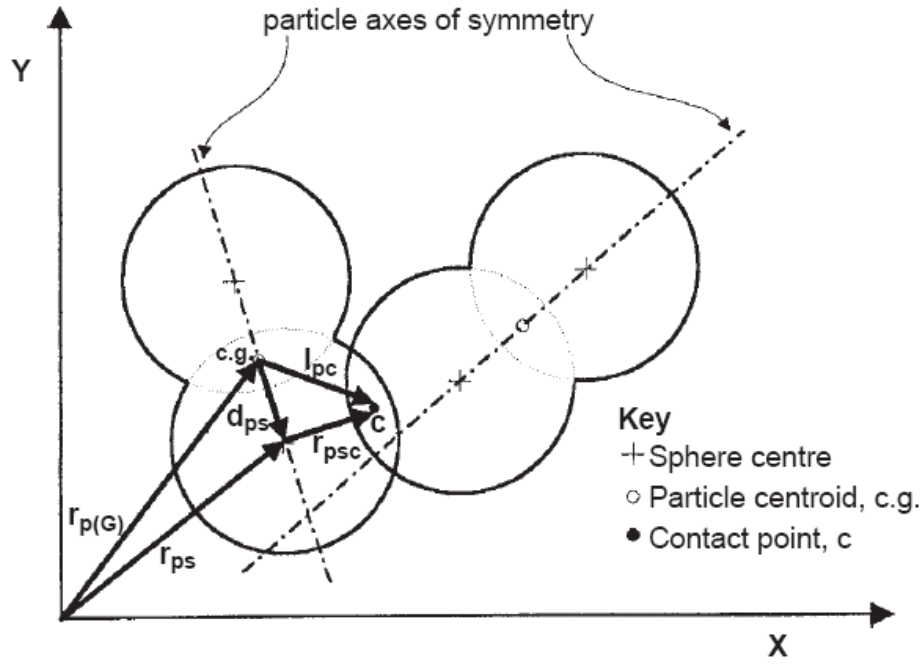

Figure 3.1: Schematic of contact between two multi-element axis-symmetrical particles, each comprising two element spheres of the same diameter (Favier et al., 1999)

Figure 3.2b shows that this force is transferred to the centre of each element sphere. The moments generated by force acting on the centre of each element sphere which so not pass through the centroid of the particle are then added to the moment of the tangential forces, giving the total moment acting on the particle, as shown in Figure 3.2c.

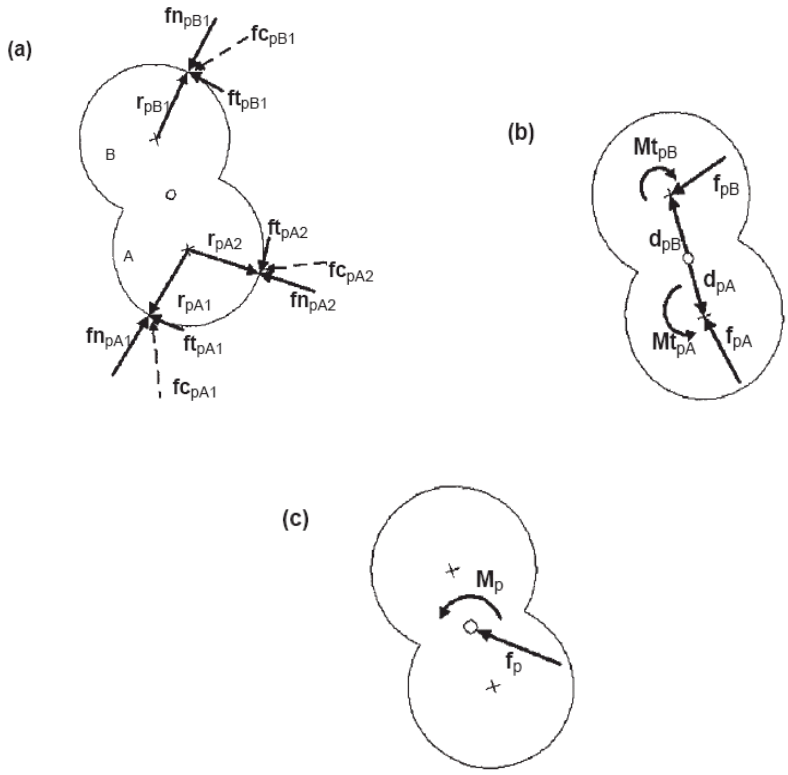

Figure 3.2: Method of transfer of force acting on element spheres to the centroid of a particle (Favier et al., 1999)

$$M_P = \sum_{S=1}^{S} \left[\left(d_{ps} \times f_{ps} \right) + M_{t_{ps}} \right] \tag{3.3}$$

$$M_p = \sum_{s=1}^{s} \left[\left(d_{ps} \times f_{ps} \right) + \sum_{c=1}^{c} \left(r_{psc} \times f_{t_{psc}} \right) \right] \tag{3.4}$$

where S is total number of element spheres in the particle. The total out-of-balance force acting on the particle is the vectorial sum of resultant contact forces acting on its element spheres:

$$f_p = \sum_{s=1}^{s} f_{ps} \tag{3.5}$$

Once the total force and moment of particle have been determined, the translational and rotational acceleration of the particle can be calculated using Newton's second law (Favier et al., 1999). Figure 3.3 shows the three arbitrary particle reference points A_1, A_2 and A_3 in the co-ordinate frame. The position vectors of these points have to be linearly independent. The new inertia tensor can be visualised by the inertia ellipsoid whose major axes are coincident with the principal axes of inertia and the total applied moment on a particle is transformed from global co-ordinate to the local co-ordinate system during each timestep (Favier et al., 1999). This multi-sphere method uses overlapping spheres to represent non-sphereical particles.

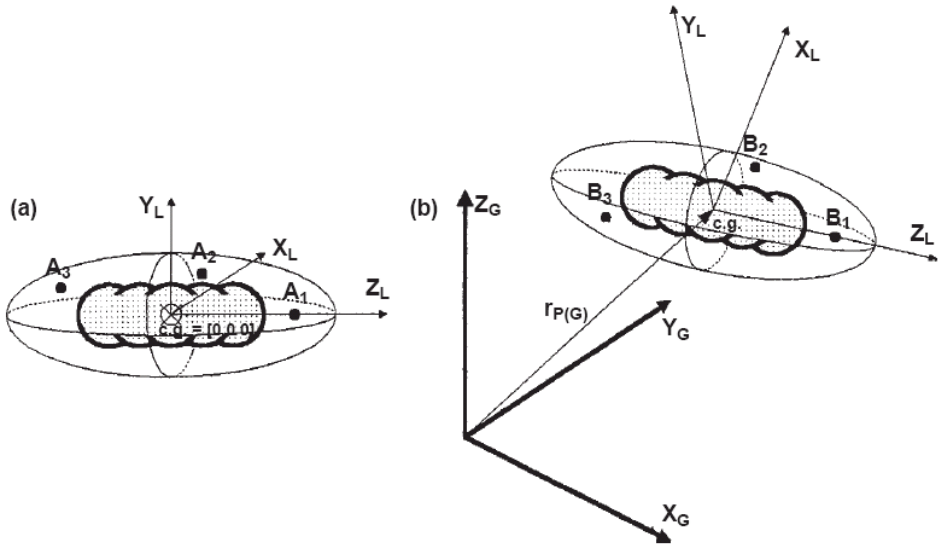

Figure 3.3: Characteristic inertial ellipsoid for a particle a) during particle generation with arbitrary reference points A1, A2 and A3 and b) during transformation of local rotation acceleration to the global co-ordinate system showing rotated reference points B1,B2 and BDN3 (Favier et al., 1999)

Elastic ellipsoidal particles are used in a three-dimensional discrete element model (Lin and Ng, 1997). A new numerical model (computer code ELLIPSE3D) has been developed in this paper. The results show that particle shape has a very important effect on shear strength, deformation behaviour and fabric statistics of particle arrays. It described that non-spherical particles in the discrete element model can possibly be used to study the effect of particle shape and to improve the results of DEM.

Hogue (1998) pointed out that a lot of computational models can not directly address the problem about the assemblies of arbitrary particles. When the model extends to three dimensions, the arbitrary shape is more accentuated. Several shapes of particle were described in two and three dimensions and their related techniques for contact detection were compared in his paper. Flexible shape descriptors were then described and it can represent a variety of arbitrary shapes within a single simulation allowing efficient, accurate collision detection between adjacent bodies. Rothenburg and Bathurst (1992) described the results of numerical simulation using elliptical particles. The influence of particle eccentricity on peak friction angle and peak dilation rate was presented in this paper. The accuracy of the proposed stress-force-fabric relationship can be verified from the results comparing between perfectly circular particles and particles of elliptical shape.

The fabric evolution of ellipsoidal arrays with different particle shapes was developed by Ng (2001). He focused on a DEM simulation of drained triaxial compression tests of ellipsoid arrays using different aspect ratios (major/minor axis of the ellipsoidal particle) varying between 1.2 and 2. The program

ELLIPSE3D was used in the drained triaxial compression tests simulation with periodic boundaries and zero gravity. The fabric parameters were shown in Figure 3.4, including the particle orientation, normal vector, branch vector (the vector from one particle centre to the contacted neighbour's centre), branch angle and branch distance. Figure 3.5 showed the results of stress-strain behaviour and volume strain for four specimens. The stress-strain behaviours of these four samples were quite similar, as shown in Figure 3.5(a). The volume changes were shown in Figure 3.5(b). It indicated that the effect of particle shape on the volume change was obvious. The volumetric dilation decreased with increasing a/b if data of a/b=1.2 was ignored.

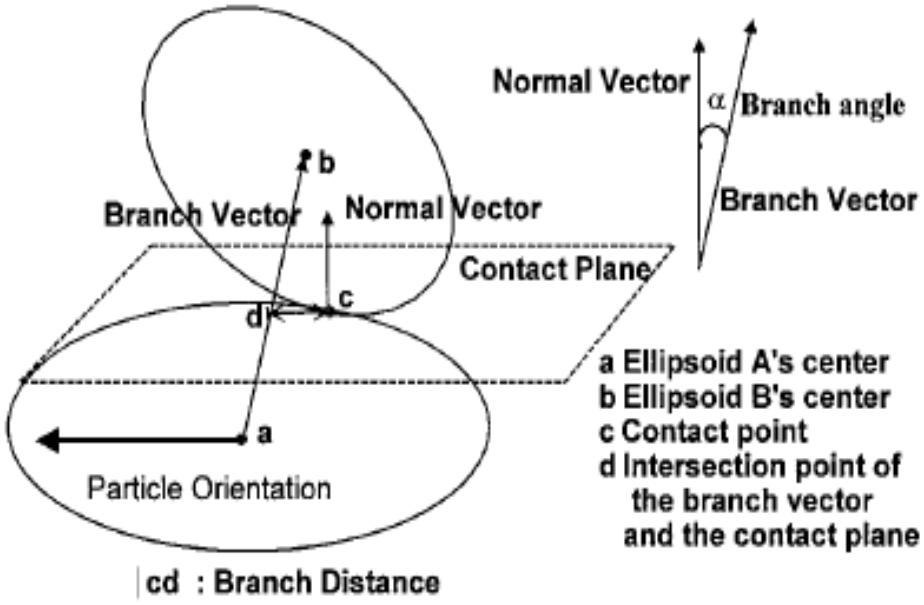

Figure 3.4: Fabric parameters (Ng, 2001)

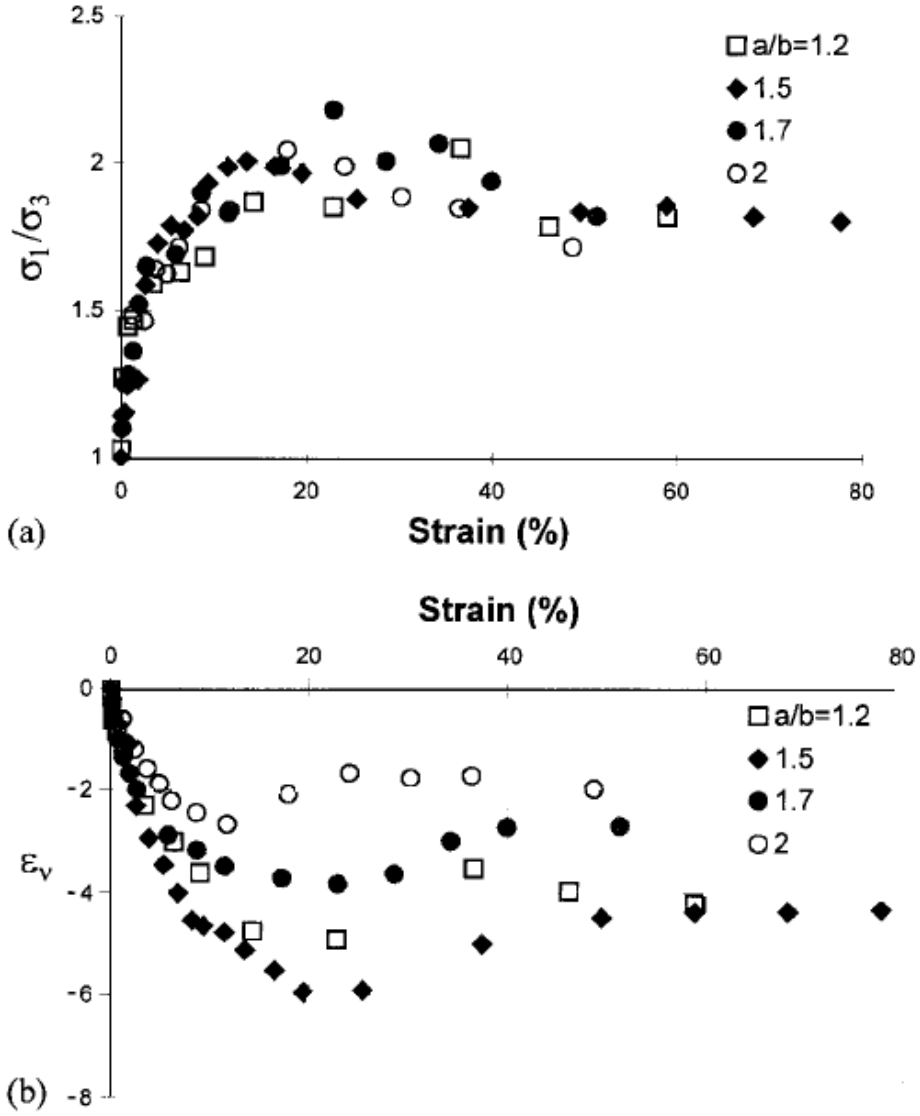

Figure 3.5: Microscopic results of four specimens: (a) Stress-strain behaviour (b) Volumetric strain (Ng, 2001)

The effect of applied stress, initial sample porosity, particle shape and interparticle friction on the behaviour of sand using DEM was studied in Ni's work (Ni, 2003). In order to investigate the effect of the particle shape, each particle was modelled as two spheres bonded together with a high strength parallel bond, as shown in Figure 3.6. The bond can be imagined to act as a column of elastic glue between the two spheres. The overall shape of particle

was determined by the radius of these two spherical balls and particle shape factor was defined as (R+r)/R. They found that the deformation and shear strength of the assembly are a function of the particle shape factor. The peak/ultimate shear strength and the overall dilation of the sample during the simulations increased with increasing the shape factor. However, the degree of particle rotation reduced significantly with increasing particle shape factor. It has been improved that particle shape was a very vital parameter for particle movement since restraining rotation of spherical particles can not capture the effect of interlocking provided by particle shape.

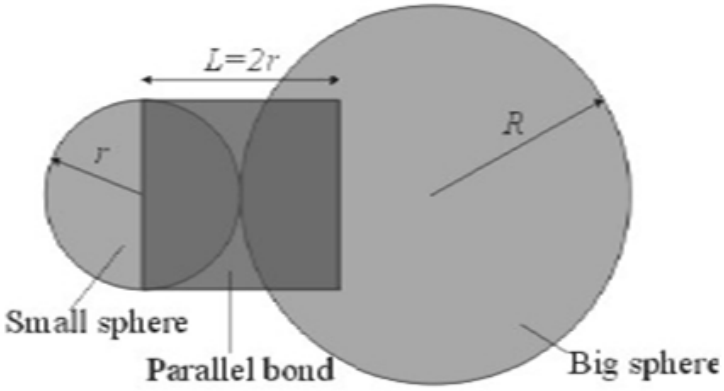

Figure 3.6: Particle bonded (Ni, 2003)

Many researchers focused on the development of representation of actual shape of granular materials since modelling the shape characteristic of particle was significantly important in the DEM. Since DEM was used to simulate the railway ballast behaviour (Norman and Selig, 1983; McDowell et al., 2005), the shape of railway ballast has been studied by many people. Lim and McDowell (2005) developed clumps with simple cubic of 8 spheres to simulate the box tests. They found that the eight-ball clumps give much more realistic

behaviour due to particle interlocking. The effect of the shape of railway ballast on their behaviour has been investigated by Lu and McDowell (2007). Both spherical particle and clumps were used to represent railway ballast particle in the simulations. A procedure was developed to generate the clump which is close to the real ballast, the geometry and generation of a clump along a direction x was shown in Figure 3.7. It has been shown that balls have been generated in all selected directions to model the real ballast shape in Figure 3.8. The edge of the clump was formatted by using the generated balls.

A developed procedure for simulating the real ballast was described in Lu and McDowell's paper (2007). It has been noted that the result using clump of the developed procedure was closer to the real ballast behaviour obtaining from experimental test.

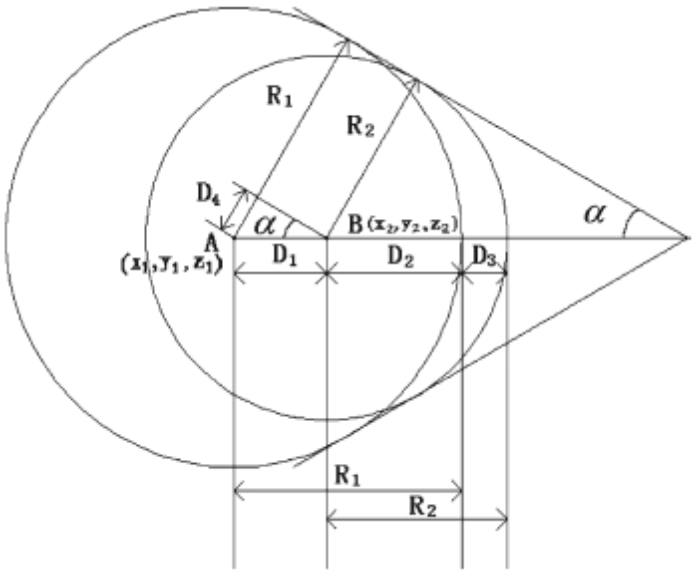

Figure 3.7: Definition of clump geometry (Lu and McDowell, 2007)

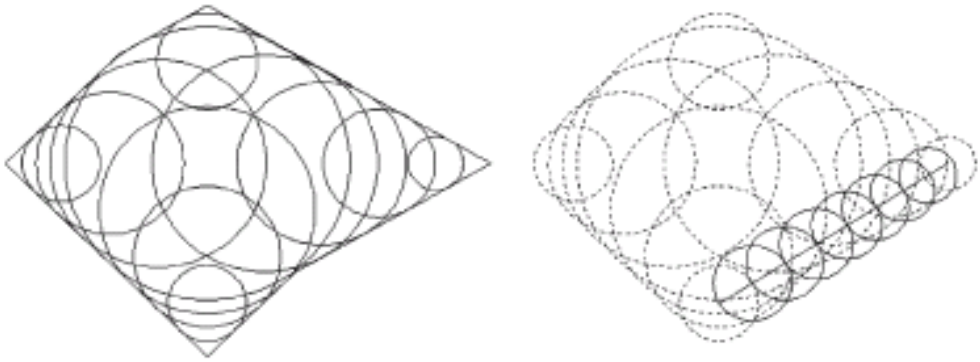

Figure 3.8: Formation of edge of clump (Lu and McDowell, 2007)

3.3.2 The rotation of each particle

Interpretation of tests on real granular media, such as sand, is difficult because the stresses inside of the sample cannot be measured, so boundary conditions must be established. The DEM treats soil like discrete particles and the two-dimensional disk is used to simulate the laboratory tests in Ting et al.'s paper (1989). The results show that two-dimensional DEM can simulate realistic nonlinear, stress history-dependent soil behaviour appropriately when rotational is restrained of each particle (Ting et al., 1989). It can be found that the internal friction angle value is close to sand using DEM when the particle rotation is inhibited.

Iwashita and Oda (1998) described that rotational resistance to rolling for each particle is one of the factors controlling the strength and dilatancy of granular soils. They suggested that rotational resistance should be activated at contact points in the discrete element modelling. A modified distinct element method (MDEM) was developed by Iwashita and Oda (1998). They used MDEM to investigate the effect of rolling restriction. In the convention DEM, a set of springs, dash pots, no-tension joint, and a shear slider were replaced at each

contact which responded to a contact force F_i acting on it. Then each contact was installed by an additional set of elastic spring, dash pot, no-tension joint and a slider, which responded to the moment M_i. The contact model in MDEM was shown in Figure 3.9.

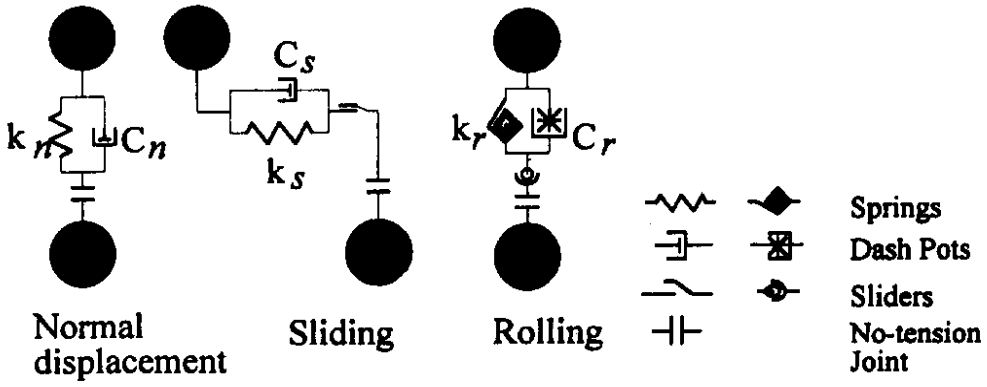

Figure 3.9: Contact Model in MDEM (Iwashita and Oda, 1998)

Three biaxial tests were carried out to investigate the effect of rolling resistant on the microstructure which developed in the shear band. The relationship between the stress ratio and the axial strain, as well as the relationship between the axial strain and volumetric strain were shown in Figure 3.10. The curve of rolling resistant test simulation was in between the curves of free rolling test and no rolling test simulations. It is clear to see that a higher peak and ultimate shear strength were observed by restricting the particle rotations, compared with simulations using free rolling particles.

It can be noted that the shear bands has been developed well when the particle rolling resistant is considered in DEM. That means the high gradient of particle rotation along the shear band boundaries could be used as a manner to obtain the natural granular soils.

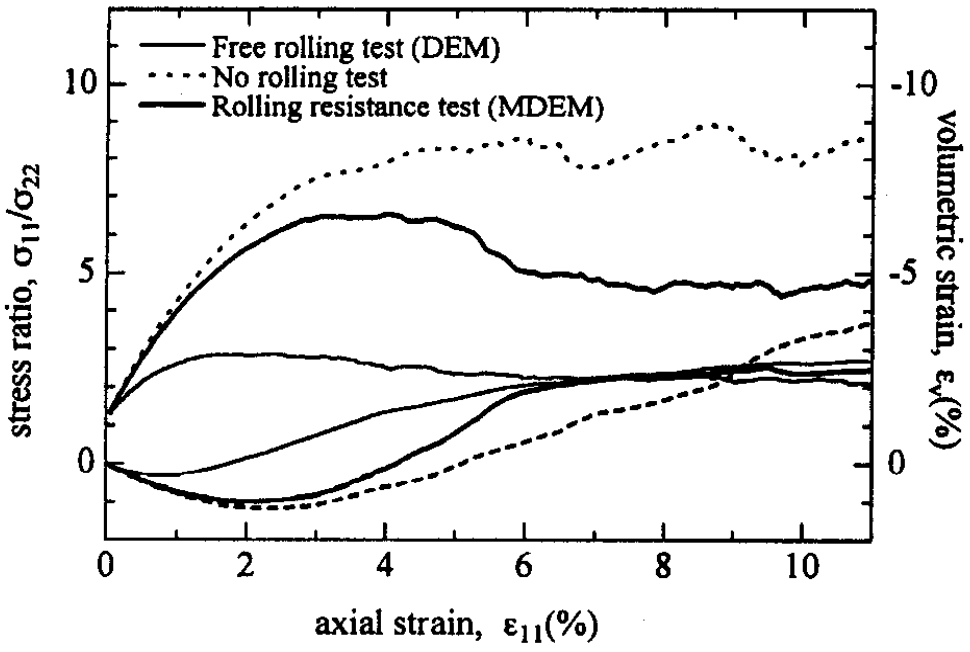

Figure 3.10: Stress ratio-axial strain-volumetric strain relationships in three numerical simulation tests (Iwashita and Oda, 1998)

3.3.3 Interparticle friction angle

From the previous research, it is very clear to see that interparticle friction has a very important effect on the granular material behaviour. The relationship between the interparticle friction and shearing strength was investigated using the results of laboratory triaxial test (Bishop, 1954). Skinner (1969) pointed out that when the interparticle friction was high, the particle rolling controlled the sample volume changed and when the interparticle friction was low, the sample volume changed was controlled by sliding. The shear strength value depends on both particles rolling and sliding.

Horne (1968) described the interactions of the different packing condition and proposed a relationship between the peak strength and interpaticle friction. It presented that the shear strength increased when the interparticle friction increased.

Ni (2003) studied the effect of interparticle friction angle using direct shear box test simulations. Both spheres and two bonded spheres particles were used in the simulations. It can be noted that the interparticle friction has the significant effect on the peak strength and volumetric dilation. Both the peak strength and volumetric dilation were increased when the interparticle friction increased. For the sample consisting of two bonded spheres, the residual strength increased with increasing the interparticle friction. However, the residual strength for samples using spherical particle did not affect much by interparticle friction. The larger particle rotation was observed for sample consisting of spherical particles. As for the spherical particles, it is easy to know that the interlocking between them is less than two bonded spheres particles.

Many researchers focused on the effect of interparticle friction on soil behaviour. The relation between interparticle friction and soil friction angle was discussed by Kruyt and Rothenburg (2004). The results for shear strength q/p and volumetric strain with various value of interparticle friction coefficient (μ) were shown in Figure 3.11. In terms of σ_1, σ_2, mean pressure $p=1/2(\sigma_1+\sigma_2)$ and shear stress $q=1/2(\sigma_1-\sigma_2)$. It can be seen that the volumetric strain and the shear strength increased with increasing particle friction coefficient.

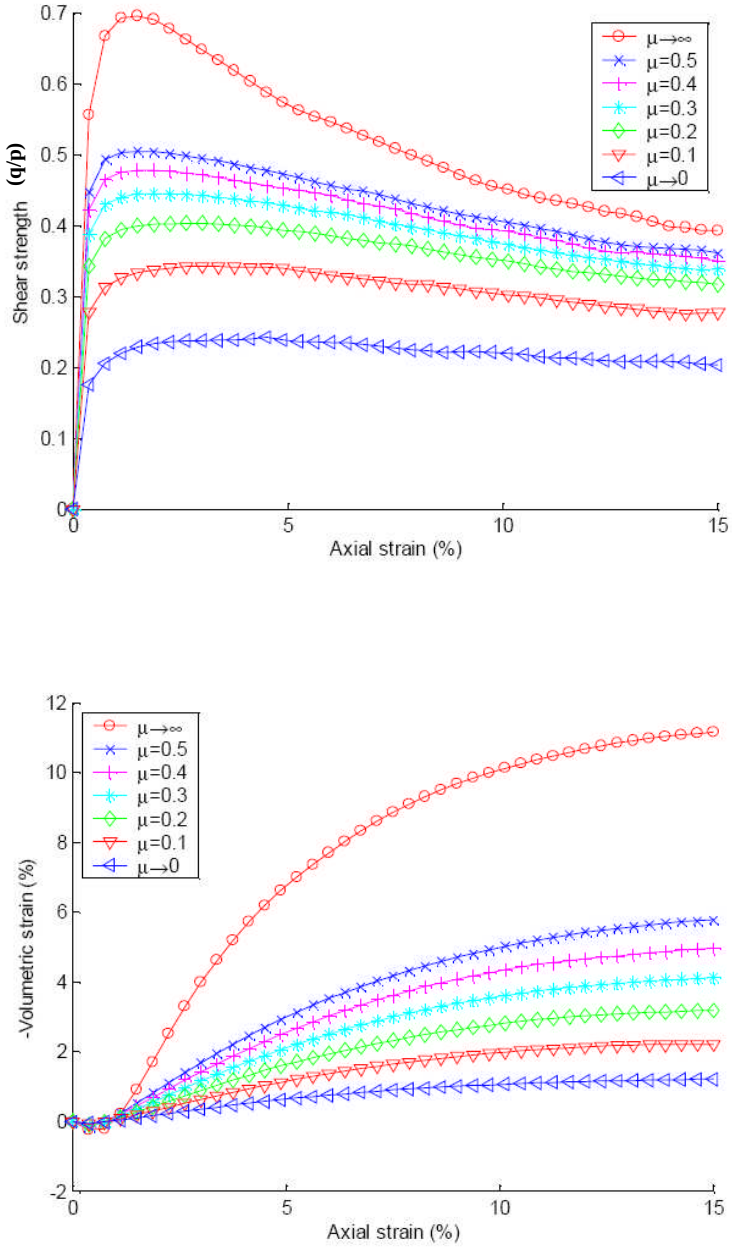

Figure 3.11: Macroscopic behaviour as a function of imposed axial strain for various interparticle friction coefficients μ (Kruyt and Rothenburg, 2004)

3.3.4 Particle fracture

Two methods have been proposed to model particle breakage in DEM. One is to treat each granular particle as a porous agglomerate built by bonding smaller particles (Robertson, 2000 and Lim and McDowell, 2005). Another is to place

the particle with an equivalent group of smaller particles when the original particle fulfils a predefined failure criterion (Lobo-Guerrero and Vallejo, 2005). The particle fracture was first investigated by Robertson (2000). Regularly packed balls of identical size were bonded together using contact bonds for forming approximately spherical agglomerates. These agglomerates were intended to represent soil grains and allowed soil particle fracture in the simulation. Three types of regular packing were investigated: face centred cubic (FCC), body centred cubic (BCC) and hexagonal close packed (HCP). The results of HCP packing were the most consistent one among these three packing types. He found that it was possible to produce a Weibull distribution of soil particle strengths by randomly removing some of the regularity in the agglomerate. Flaws of three types were introduced: removing bonds, flawing balls and removing balls. He presented that a Weibull distribution of bond strengths was best reproduced by removing balls randomly in the agglomerate and Weibull modulus depended on the range of the number of balls removed.

McDowell and Harireche (2002) used PFC^{3D} to simulate the fracture of silica sand with the crushable agglomerates particles. They used realistic particle parameters and applied gravity to stabilise the agglomerate prior to loading for replicating experiments of crushing of particles. They described that the force increase from the beginning of test by allowing the agglomerates to stabilize under the application of gravity. They also pointed out that the strengths followed the Weibull distribution, since the right average strength of agglomerates could be reproduced by a function of size and the correct statistical distribution of strength for a given size.

3.4 The PFC^{3D} Particle-Flow Model

3.4.1 Theoretical background

The PFC^{3D} model is a general particle-flow model that simulates the mechanical behaviour of a system comprised of a collection of arbitrarily-shaped particles. Particles here occupy a finite amount of space. The model consist of distinct particles that displace independently of each other and just interact only at contacts or interfaces between the particles. The fundamental relationship between particle motion and the corresponding forces follows Newton's laws of motion. Particles are assumed to be rigid and the behaviour of the system is shown by the motion of each particle and the force acting on each contact point. PFC^{3D} allows particle bonding together at the contact point. The bond will break when the acting force exceeds the bond strength. The velocity boundary conditions can be applied on the wall to model the ball compaction. The contact point affects each other (ball-ball or ball-wall). Newton's second law is used as the principle for the motion of each particle arising from the contact and body forces acting upon it, while the force-displacement law is used to update the contact force arising from the relative motion at each contact.

3.4.1.1 Assumptions

PFC^{3D} can model stressed assemblies using the movement and interaction of rigid spherical particles based on the DEM. PFC^{3D} provides a particle-flow model containing the following assumptions:

1. The particles are treated as rigid bodies.

2. The contacts occur over a vanishingly small area (as a point).

3. Behaviour at the contacts uses a soft-contact approach wherein the rigid particles are allowed to overlap one another at contact points.

4. The magnitude of the overlap is related to the contact force via the force-displacement law, and all overlaps are small in relation to particle sizes.

5. Bonds can exist at contacts between particles.

6. All particles are spherical (the clump logic supports the creation of super-particles of arbitrary shape. Each clump consists of a set of overlapping spheres, and acts as a rigid body with a deformable boundary).

The PFC^{3D} particle-flow model includes walls and balls. Walls allow one to apply velocity boundary conditions to assemblies of balls for purposes of compaction and confinement. The balls and walls interact with one another via the forces that arise at contacts. PFC^{3D} is used to model the behaviour of granular material which the deformation results primarily from the sliding and rotation of the rigid particles and the interlocking at particle interfaces. A physical problem is concerned with the movement and interaction of spherical particles by PFC^{3D}. It is also possible to create particles of arbitrary shapes by bonding the particles together at the contact points for obtaining more complex

behaviours of granular materials. The mathematical backgrounds and some conceptual models are presented in the following section (Itasca, 1999).

3.4.1.2 Theory of PFC

3.4.1.2.1 Calculation cycle

The repeated application of the law of motion to each particle is performed in the calculation cycle in PFC^{3D}. Contact exists between the balls or a ball and a wall, which is formed and broken automatically during the simulation (Zhou et al., 2006).

The calculation cycle in PFC^{3D} is a timestepping algorithm that requires the repeated application of the law of motion to each particle, a force-displacement law to each contact, and constant updating of wall positions. The calculation cycle is illustrated in Figure 3.12. At the start of each timestep, the contacts are updated from the known particle and wall positions. Then the force-displacement law is applied to each contact to update the contact forces based on the relative motion between the two contacted entities and the contact constitutive model. After that, the law of motion is applied to each particle to update its velocity and position based on the resultant force and moment arising at the contact forces and the body forces acting on the particle. Also the wall positions are updated based on the specified wall velocities.

(1) Force-Displacement law

The force-displacement law relates the relative displacement between two entities at a contact and the contact force acting on the entities. There are two types of the contacts: ball-ball and ball-wall.

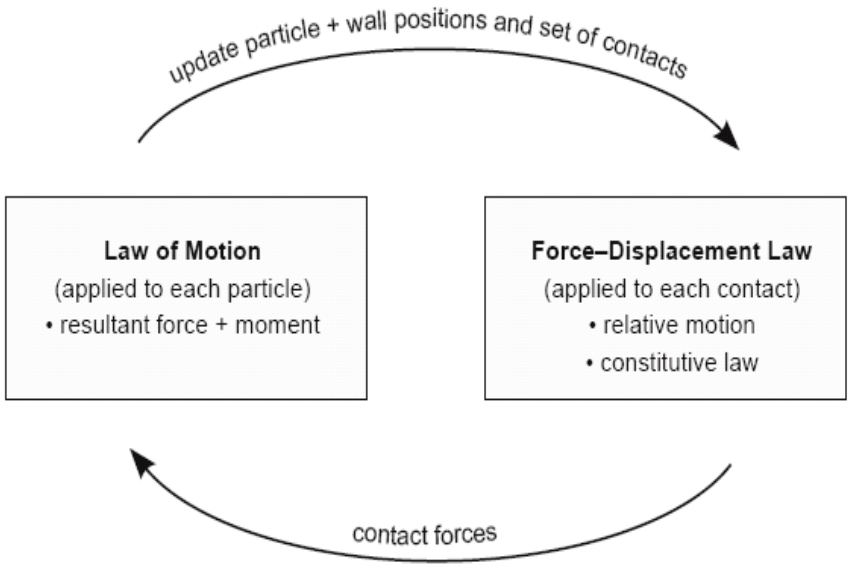

Figure 3.12: Calculation cycle in PFC^{3D} (Itasca, 1999)

The contact force vector F_i can be resolved into normal and shear components with respect to the contact plane as

$$F_i = F_i^n + F_i^s \tag{3.6}$$

Where F_i^n and F_i^s denote the normal and shear component vectors, respectively.

The normal contact force vector is calculated by

$$F_i^n = K^n U^n n_i \tag{3.7}$$

Where K^n is the normal stiffness [force/displacement] at the contact and the value is determined by the current contact-stiffness model. n_i is the unit normal and U^n is the overlap of the two entities.

The shear contact force is calculated in an incremental fashion. When the contact is formed, the total shear contact force is initialized to zero. Each subsequent relative shear-displacement increment results in an increment of elastic shear force that is added to the current value. The shear component of the contact displacement-increment vector occurring over a time step of Δt is calculated by

$$\Delta U_i^s = V_i^s \Delta t \tag{3.8}$$

The shear elastic force-increment vector is calculated by

$$\Delta F_i^s = -k^s \Delta U_i^s \tag{3.9}$$

Where k^s is the shear stiffness [force/displacement] at the contact and the value is determined by the current contact stiffness model. The shear stiffness is a tangent modulus. Finally, the new shear contact force is calculated by summing the old shear force vector existing at the start of the timestep with the shear elastic force-increment vector.

$$F_i^s = F_j^s + \Delta F_i^s \tag{3.10}$$

The values of normal and shear contact force, determined by equations 3.7 and 3.10, are adjusted to satisfy the contact constitutive relations. After this

adjustment, the contribution of the final contact force to the resultant force and moment on the two entities in contact is given by

$$F_i^{[\Phi^1]} \leftarrow F_i^{[\Phi^1]} - F_i \tag{3.11}$$

$$F_i^{[\Phi^2]} \leftarrow F_i^{[\Phi^2]} - F_i \tag{3.12}$$

$$M_i^{[\Phi^1]} \leftarrow M_i^{[\Phi^1]} - e_{ijk}(x_j^{[C]} - x_j^{[\Phi^1]})F_k \tag{3.13}$$

$$M_i^{[\Phi^2]} \leftarrow M_i^{[\Phi^2]} - e_{ijk}(x_j^{[C]} - x_j^{[\Phi^2]})F_k \tag{3.14}$$

Where $F_i^{[\Phi^j]}$ and $M_i^{[\Phi^j]}$ are the force and moment sums for entity Φ^j from $\{\Phi^1, \Phi^2\} = \begin{cases} \{A, B\}, (ball - ball) \\ \{b, w\}, (ball - wall) \end{cases}$, and F_i is given by equation 3.10.

(2) Law of Motion

The motion of a single particle is determined by the resultant force and moment vectors acting upon it and can be described in terms of the translation motion of a point in the particle and the rotational motion of the particle.

The equations of motion can be expressed as two vector equations. One of equations relates the resultant force to the translational motion and the other one relates the resultant moment to the rotational motion. The equations of motion can be written in the vector form as

$$F_i = m(\ddot{x}_i - g_i) \qquad \text{Translational motion,} \tag{3.15}$$

$M_i = \dot{H}_i$ Rotational motion, (3.16)

Where F_i is the resultant force, the sum of all externally applied forces acting on the particle; m is the total mass of the particle; g_i is the body force acceleration vector; M_i is the resultant moment acting on the particle; H_i is the angular momentum of the particle.

For a spherical particle of radius R with distributing uniformly, the centre of mass coincides with the sphere centre. $M_i = \dot{H}_i$ can be simplified and referred to the global-axis system as $M_i = I\dot{\omega}_i = (\frac{2}{5}mR^2)\dot{\omega}_i$. The two equations 3.17 and 3.18 of motion are integrated by finite difference procedure using a timestep Δt. The equations $\dot{x}_i$ and ω_i are calculated at the mid-intervals $(t \pm n\Delta t/2)$, and the other equations $x_i, \ddot{x}_i, \dot{\omega}_i, F_i,$ and M_i are calculated at the primary intervals $(t \pm n\Delta t)$.

$$F_i = m(\ddot{x}_i - g_i) \tag{3.17}$$

$$M_i = I\dot{\omega}_i = (\frac{2}{5}mR^2)\dot{\omega}_i \tag{3.18}$$

The accelerations of translation and rotation at time t in terms of the velocity values at mid-intervals are shown as:

$$\ddot{x}_i^{(t)} = \frac{1}{\Delta t}(\dot{x}_i^{(t+\Delta t/2)} - \dot{x}_i^{(t-\Delta t/2)}) \tag{3.19}$$

$$\dot{\omega}_i^{(t)} = \frac{1}{\Delta t}(\omega_i^{(t+\Delta t/2)} - \omega_i^{(t-\Delta t/2)}) \tag{3.20}$$

So, the velocities at time $(t + \Delta t/2)$ can be calculated:

$$\dot{x}_i^{(t+\Delta t/2)} = \dot{x}_i^{(t-\Delta t/2)} + (\frac{F_i^{(t)}}{m} + g_i)\Delta t \tag{3.21}$$

$$\omega_i^{(t+\Delta t/2)} = \omega_i^{(t-\Delta t/2)} + (\frac{M_i^{(t)}}{I})\Delta t \tag{3.22}$$

Finally, used these velocities to update the position of the particle centre:

$$x_i^{(t+\Delta t)} = x_i^{(t)} + \dot{x}_i^{(t+\Delta t/2)} \Delta t \tag{3.23}$$

In the summary, values of $\dot{x}_i^{(t-\Delta t/2)}, \omega_i^{(t-\Delta t/2)}, x_i^{(t)}, F_i^{(t)}$, and $M_i^{(t)}$ are used to obtain the values of $\dot{x}_i^{(t+\Delta t/2)}$ and $\omega_i^{(t+\Delta t/2)}$, finally $x_i^{(t+\Delta t)}$ can be calculated. $F_i^{(t+\Delta t)}$, $M_i^{(t+\Delta t)}$ can be calculated from force-displacement law and then used in the next cycle

3.4.2 Contact constitutive model

The overall constitutive behaviour of a material is simulated in PFC^{3D} by associating a simple constitutive model in each contact. The constitutive model acting at a particular contact consists of three parts: a stiffness model, a slip model and a bonding model. The stiffness model provides an elastic relation between the contact force and relative displacement. The slip model enforces a relation between shear and normal contact forces so that the two containing

balls may slip relative to one another. The bonding model serves to limit the total normal and shear forces that the contact can carry by enforcing bond-strength limits. These three models are described in detail in the following section.

(1) Contact-stiffness model

The contact stiffness provides the relative displacement via a Force-Displacement Law. Two models are described in PFC^{3D} which are linear model and Hertz-Mindlin model. The linear contact model is defined by the normal stiffness (k_n) and shear stiffness (k_s) between two contacts and assumes that the stiffnesses of the two contacting entities A and B act in series. The contact normal and shear stiffnesses for the linear contact model are given by

$$K^n = \frac{k_n^{[A]} k_n^{[B]}}{k_n^{[A]} + k_n^{[B]}} \tag{3.24}$$

$$k^s = \frac{k_s^{[A]} k_s^{[B]}}{k_s^{[A]} + k_s^{[B]}} \tag{3.25}$$

Where the superscripts [A] and [B] denote the two entities in contact.

(2) The Slip Model

The slip model is an intrinsic property of two entities in contact. It provides no normal strength in tension and allows slip to occur by limiting the shear force. The model describes the constitutive behaviour for particle contact occurring at a point, and it is suitable to be used for the disseminate material such as sand (Zhou et al., 2006). This model is defined by the friction coefficient at the

contact μ [dimensionless], where μ is taken to be the minimum friction coefficient of the two contacting entities. If the overlap is less than or equal to zero, both the normal and shear contact forces are set to zero.

The contact is checked for slip conditions by calculating the maximum allowable shear contact force

$$F_{\max}^{s} = \mu \left| F_i^{n} \right| \tag{3.26}$$

If $\left| F_i^{s} \right| > F_{\max}^{s}$, then slip is allowed to occur (in the next calculation cycle) by setting the magnitude of F_i^{s} via

$$F_i^{s} \leftarrow F_i^{s} (F_{\max}^{s} / \left| F_i^{s} \right|) \tag{3.27}$$

(3) The bonding models

PFC^{3D} allows particles to be bonded together at contacts. Two bonding models are available: a) a contact-bond model and b) a parallel-bond model. The two types of bonds may be active at the same time. However the presence of a contact bond inactivates the slip model. The bonds can be envisioned as a kind of glue joining the two particles. Once a bond is formed at a contact between two particles, the contact continues exist until the bond broken. Particles can only be bonded to particles, while a particle can not be bonded to a wall. The model is suitable for modelling the cohesive materials such as clay (Zhou et al., 2006).

a) The contact-bond model

The contact-bond glue is of a vanishingly small size that acts only at the contact point and the contact bonds can only transmit a force. A contact bond can be envisaged as a pair of elastic springs with constant normal and shear stiffnesses acting at the contact point. These two springs have specified shear and tensile normal strengths. The magnitude of the shear contact force is limited by the shear contact bond strength and tensile force can be developed at a contact in the contact bonds. The magnitude of the tensile normal contact force is determined by the normal contact bond strength.

A contact bond consists of normal contact bond strength F_c^n and shear contact bond strength F_c^s. If the magnitude of the tensile normal contact force equals or exceeds the normal contact bond strength, the bond breaks, and both the normal and shear contact forces are set to zero. If the magnitude of the shear contact force equals or exceeds the shear contact bond strength, the bond breaks, but the contact forces are not altered, provided that the shear force does not exceed the friction limit and provided that the normal force is compressive. The constitutive behaviour relating the normal and shear components of contact force and relative displacement for particle contact occurring at a point is shown in Figure 3.13.

b) The parallel-bond model

A parallel bond can be envisaged as a finite sized piece of cementations material acted over a circular cross-section lying between the particles. The parallel bond can transmit both forces and moments between particles. The constitutive behaviour of the parallel bond is shown in the Figure 3.14, similar

with the contact bond. Relative motion at the contact causes a force and a moment to develop within the bond material as a result of the parallel bond stiffnesses. The parallel bond breaks when either of these normal and shear maximum stresses exceeds the corresponding parallel bond strength.

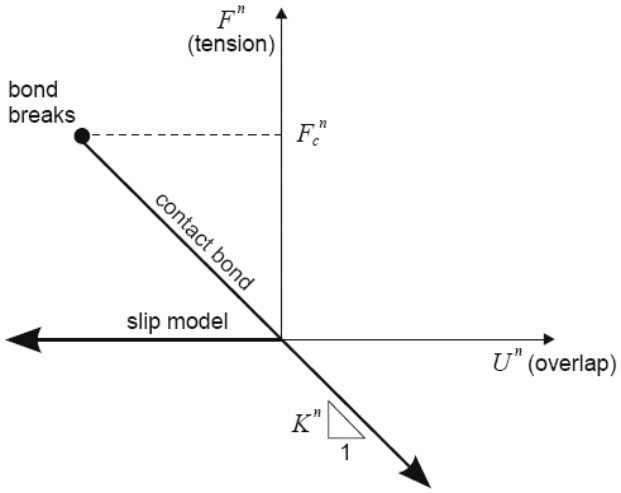

(a) Normal component of contact force

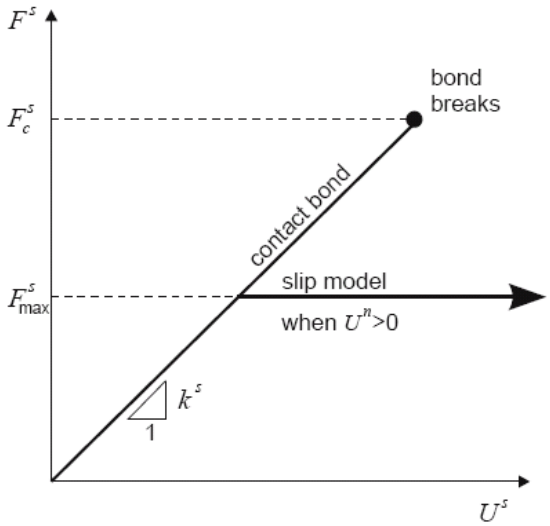

(b) Shear component of contact force

Figure 3.13: Constitutive behaviour for contact occurring at a point (Itasca, 1999)

The total force and moment associated with the parallel bond are denoted by $\overline{F_i}$ and $\overline{M_i}$, with the convention that this force and moment represent the action of the bond on sphere B in Figure 3.14. Each of these vectors can be resolved into normal and shear components with respect to the contact plane as

$$\overline{F_i} = \overline{F}_i^n + \overline{F}_i^s \tag{3.28}$$

$$\overline{M_i} = \overline{M}_i^n + \overline{M}_i^s \tag{3.29}$$

Where $\overline{F}_i^n$, $\overline{M}_i^n$ and $\overline{F}_i^n$, $\overline{M}_i^s$ denote the normal and shear component vectors, respectively. These vectors are shown in Figure 3.14.

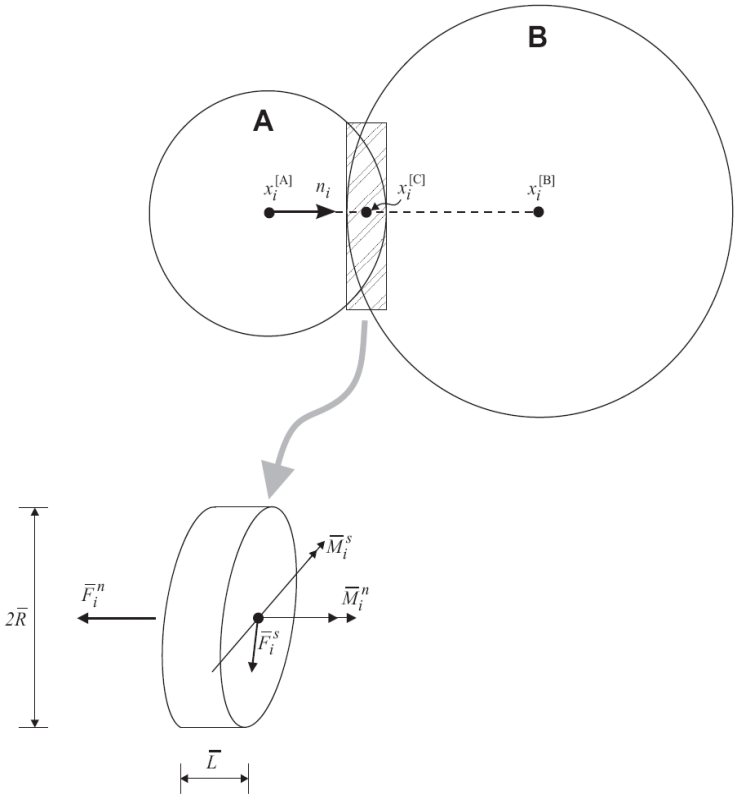

Figure 3.14: Parallel bond depicted as a cylinder of cementations material (Itasca, 1999)

Where the parallel bond is depicted as a cylinder of elastic material, the normal component vectors can be expressed in terms of the scalar values $\overline{F}^n$ and $\overline{M}^n$ via

$$\overline{F}_i^n = (\overline{F}_j n_j) n_i = \overline{F}^n n_i \tag{3.30}$$

$$\overline{M}_i^n = (\overline{M}_j \; n_j) n_i = \overline{M}^n n_i \tag{3.31}$$

The maximum tensile and shear stresses acting on the bond periphery can be calculated by

$$\sigma_{\max} = \frac{-\overline{F}^n}{A} + \frac{\left|\overline{M}_i^s\right|}{I}\overline{R} \tag{3.32}$$

$$\tau_{\max} = \frac{\left|\overline{F}_i^s\right|}{A} + \frac{\left|\overline{M}^n\right|}{J}\overline{R} \tag{3.33}$$

Where *A* is the area of the bond disk, *J* is the polar moment of inertia of the disc cross-section, *I* is the moment of inertia of the disc cross-section about an axis through the contact point, and R is the radius of the bond disc. The values of these parameters can be calculated as:

$$A = \pi \overline{R}^2 \tag{3.34}$$

$$J = \frac{1}{2}\pi \overline{R}^4 \tag{3.35}$$

$$I = \frac{1}{4}\pi \overline{R}^4 \tag{3.36}$$

3.4.3 Clump logic

A clump is a single entity of overlapping balls and behaves as a rigid body (i.e. the balls comprising the clump remain at a fixed distance from each other). Internal overlapping contacts are ignored in calculations, resulting in a saving of computational time compared to a similar calculation in which all contacts are active. Thus, a clump acts as a rigid body (with a deformable boundary) that will not break apart, regardless of the forces acting upon it. In this sense, a clump differs from a group of particles that are bounded to one another.

The total mass of a clump m, the location of the centre of mass of clump $x_i^{[G]}$ and the moments and products of inertia I_{ii} and I_{ij}, which are the basic mass properties of a clump, are defined by the following equations:

$$m = \sum_{p=1}^{N_p} m^{[p]} \tag{3.37}$$

$$x_i^{[G]} = \frac{1}{m} \sum_{p=1}^{N_p} m^{[p]} x_i^{[p]} \tag{3.38}$$

$$I_{ii} = \sum_{p=1}^{N_p} \left\{ m^{[p]} \left(x_j^{[p]} - x_j^{[G]} \right) \left(x_j^{[p]} - x_j^{[G]} \right) + \frac{2}{5} m^{[p]} R^{[p]} R^{[p]} \right\} \tag{3.39}$$

$$I_{ij} = \sum_{p=1}^{N_p} \left\{ m^{[p]} \left(x_i^{[p]} - x_i^{[G]} \right) \left(x_j^{[p]} - x_j^{[G]} \right) \right\} ; \ \left(j \neq i \right) \tag{3.40}$$

Where N_p is the number of balls in the clump, $m^{[p]}$ is the mass of a ball, $x^{[p]}$ is the centroid location of the ball and $R^{[p]}$ is the radius of the ball.

The motion of a clump is determined by the resultant force and moment vectors acting upon it. Because a clump is treated as a rigid body, its motion can be described in terms of the translational motion of the entire clump. The equation for translational motion can be written in the vector from

$$F_i = m\left(\ddot{x}_i - g_i\right) \tag{3.41}$$

where F_i is the resultant force, the sum of all externally-applied forces acting on the clump and g_i is the body force acceleration vector arising from gravity loading.

The equation for rotational motion can be written in the vector form

$$M_i = \dot{H}_i \qquad \text{(rotational motion)} \tag{3.42}$$

Where M_i is the resultant moment about the centre of mass, and $\dot{H}_i$ is the time rate-of-change of the angular momentum of the clump.

The resultant moment in Eq. (3.42) is computed by

$$M_i = \sum_{p=1}^{N_p}\left(\tilde{M}_i^{[p]} + \varepsilon_{ijk}\left(x_j^{[p]} - x_j^{[G]}\right)F_k^{[p]} + \sum_{c=1}^{N_c}\varepsilon_{ijk}\left(x_j^{[c]} - x_j^{[p]}\right)F_k^{[p.c]}\right) \tag{3.43}$$

Where $\tilde{M}_i^{[p]}$ is the externally-applied moment acting on particle (p), $F_k^{[p]}$ is the resultant force acting on particle (p) at its centroid, and $F_k^{[p,c]}$ is the force acting on particle (p) at contact (c).

The time rate-of-change of the angular momentum for a system can be written as

$$\dot{H}_i = \alpha_i I_{ii} - \alpha_j I_{ij} + \varepsilon_{ijk}\omega_j(\omega_k I_{kk} - \omega_l I_{kl}) \qquad (j \neq i, l \neq k) \tag{3.44}$$

Where $\alpha_i = \dot{\omega}_i$.

3.5 Summary

DEM has been used to model geotechnical problems by many researches. The basic concepts and general mathematical backgrounds of PFC^{3D} have been presented in this chapter. DEM is a powerful tool for fundamental research on the behaviour of granular materials. The main disadvantage of DEM simulation is the enormous computational expense, since a very small timestep of simulation must be used to ensure the numerical stability and accuracy. Many particles are required to guarantee the sufficient number of contacts. It enables to investigate the particle properties which can not be obtained using continuum mechanics, such as interparticle friction, contact forces distribution, as well as coordination numbers. The circular/spherical shape particles tend to roll excessively and then lead to a lower strength of the assembly, so clump of complex particle shape and restraining the rotation of circular/spherical particles have been developed to solve this problem. The determination of particle parameters (particle shape, particle rotation and friction coefficient) in the DEM is important for modelling the behaviour of granular materials.

CHAPTER 4

DEM SIMULATION OF BIAXIAL TEST

4.1 Introduction

Granular media such as sand composed of discrete particles exhibit very complex macroscopic mechanical responses to externally applied loading. The Biaxial test is one of the most important laboratory tests to investigate the soil stress-strain behaviour. The Biaxial consolidation test was developed to determine the axial and radial permeabilities by Peters and Leavell (1986) and then showed that isotropy in stiffness has an important effects on the results. Previous researchers have succeeded in using PFC^{3D} to simulate the properties of granular material (Ni, 2003). Compacting of particles for the biaxial compression test using DEM was discussed by Darius and Rimantas (2006). Packing of polygonal particles was used to simulate the biaxial test by Pena et al (2008); they showed the effects of initial density and the interparticle coefficient of friction on the macro mechanical behaviour of granular material. Tatsuoka et al. (1986) performed drained plane strain compression tests on saturated samples of fine angular to sub-angular sand at confining pressures of 400kPa to study the strength and deformation characteristcs of sand. The porosities of the compacted specimens were around 0.41 and 0.44. Samples

were prepared by the air-pluviation method with changing the angle δ of bedding plane to the $\sigma_1^{'}$–direction during plane strain compression tests from 0 to 90 degrees. The key results from their study are shown in Figure 4.1. It may be seen that anisotropy is significant in the strength and deformation characteristics for both dense and loose samples.

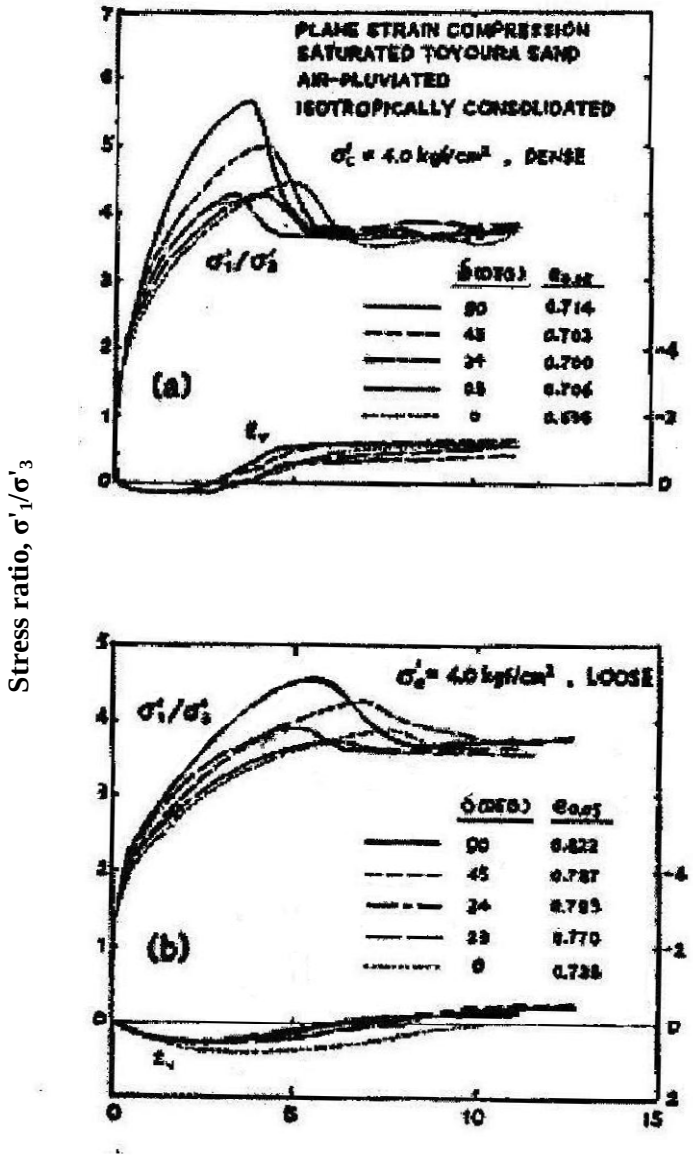

Figure 4.1: Typical stress-strain relations for tests at σ_3=400kPa for both dense and loose samples (Tatsuoka et al., 1986)

In this chapter, the discrete element method is used to simulate the mechanical behaviour of granular material under the biaxial test conditions and the results are compared with the experimental data (Tatsuoka et al., 1986), so that the effects of micro properties can be related to the macro behaviour of granular material. A confining pressure of 1000kPa has been used in a series of simulations to study the effect of particle shape, particle friction coefficient and sample initial porosity on the stress-strain behaviour of granular materials. Three different sample porosities, two different particle shapes and three different friction coefficients are studied first. The stress-strain behaviour for each simulation is then compared with that for experimental results.

4.2 Modelling Procedure

PFC^{3D} models stressed assemblies by the movement and interaction of rigid spherical particles based on DEM. The model is composed of distinct spheres that displace independently of one another and interact only at contacts or interfaces between the spheres. The contact force vector F_i can be resolved into normal and shear components (F_i^n and F_i^s) with respect to the contact plane as

$$F_i = F_i^n + F_i^s \tag{4.1}$$

The normal contact force is calculated by

$$F_i^n = K^n U^n n_i \tag{4.2}$$

Where K^n is normal stiffness [force/displacement], at the contact and U^n is the overlap of the two entities.

The shear force-increment is calculated by

$$\Delta F_i^s = -k^s \Delta U_i^s \tag{4.3}$$

The new shear contact force is calculated by summing the shear force vector existing at the start of the timestep with the shear force-increment

$$F_j^s = \left\{F_j^s\right\}^{[old]} + \Delta F_i^s \tag{4.4}$$

Where k^s is the shear stiffness [force/displacement] at the contact and ΔU_i^s is the shear component of the contact displacement-increment vector calculated from the motion. In these simulations, the normal stiffness, and shear stiffness were chosen as

$$k^n = k^s = k \tag{4.5}$$

PFC^{3D} was used to simulate the plane-strain compression test on samples consisting of spheres or clumps. A clump is a single entity of overlapping balls and behaves as a rigid body (i.e. the balls comprising the clump remain at a fixed distance from each other). Internal overlapping contacts are ignored in calculations, resulting in a saving of computational time compared to a similar calculation in which all contacts are active. Thus, a clump acts as a rigid body (with a deformable boundary) that will not break apart, regardless of the forces acting upon it. In this sense, a clump differs from a group of particles that are bounded to one another. The clump logic is given in section 3.4.3 of chapter 3. A cuboidal sample (Figure 4.2) was generated and loaded by the top and bottom walls. The right and left walls were used to maintain a constant confining pressure. The velocities of the top and bottom walls were specified to simulate the strain controlled loading, the velocities of right and left walls were

automatically controlled by a servo-mechanism (see Appendix) to keep the confining pressure constant (Figure 4.3).

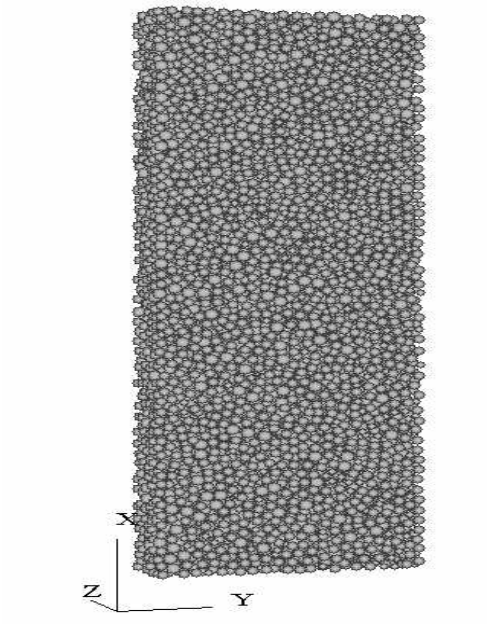

Figure 4.2: A sample of biaxial test simulations

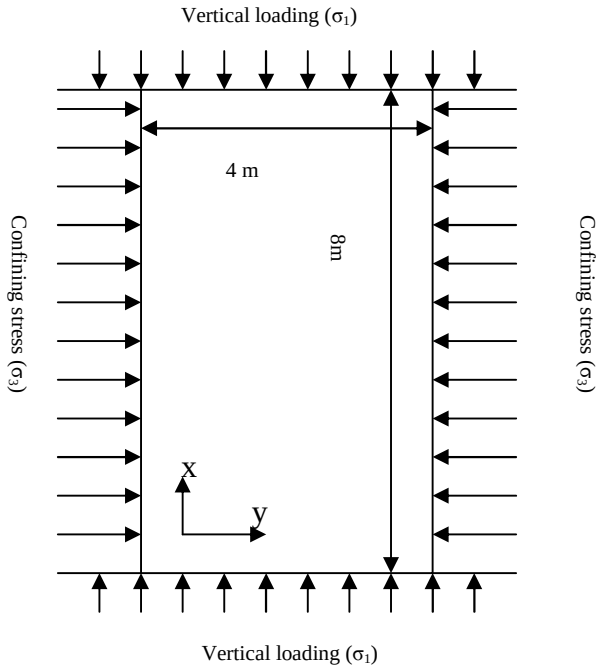

Figure 4.3: Schematic illustration of biaxial test

The sample modelled in the numerical biaxial test simulations had dimensions of 8m × 4m × 1m in the directions of the major (x), minor (y), and intermediate

(z) principal stresses respectively. The positions of the walls were recorded as well as the movement and the contact forces for each particle during the whole simulation for subsequent analysis. The properties of all walls are assumed to be same. The wall friction coefficient is 0 and wall normal stiffness and shear stiffness are chosen to be the same as particle stiffness 1×10^9 N/m. Around 7000 particles are used to form each sample in these simulations. All the particle parameters are identical. The particle size distribution for this numerical sample range from 0.075m to 0.1m. The specific gravity is 2.65. Six walls were generated as sample boundaries. Particles were generated to fill this space. The samples were generated by the particle radius expansion method. This is used to place a specified number of particles at random coordinates within a given space. A population of particles with artificially small radii is created within the specified volume because a new particle will not be placed if it would overlap another particle or a wall. The particles are then expanded until the desired porosity is obtained. The number of particles required to satisfy the specified particle size and void ratio is defined as:

$$e = \left[bht - \sum_{1}^{N} \frac{4}{3}\pi r_i^3 \right] \Big/ \sum_{1}^{N} \frac{4}{3}\pi r_i^3 \tag{4.6}$$

Where b is the width of the sample, h is the length of the sample, t is the thickness of the sample. N is the total number of the particles. After the sample is generated, the sample stress state is adjusted to $\sigma_x = \sigma_y = \sigma_0$. σ_0 is the initial consolidation confining pressure. The stresses σ_x and σ_y are defined as the axial stress and confining stress, calculated from the contact forces and the ball/wall contact areas. The loading was carried out by moving the top and

bottom walls at a rate of 0.01m/s after the sample reached the equilibrium initial state.

4.3 Influence of Initial Sample Porosity

The analyses described in this section were carried out to investigate the effect of the initial sample porosity. Friction coefficients from 0.0 to 1.0 were used to control the porosities of assemblies during artificial isotropic compaction; after compaction the friction coefficient was changed back to 0.7 for the shearing stage of the simulation. Apart from the initial porosity, the samples were generated and the biaxial tests simulated exactly as above, each sample comprising around 7000 spherical particles. The confining stress was 1000kPa, Figure 4.4 show the results of three simulations carried out from initial porosity, n, of 0.36, 0.39 and 0.42, in terms of axial stress and volumetric dilation against axial strain. The particle properties are given in Table 4.1.The peak value of axial stress varied from 3400kPa for the densest sample to 2250kPa for the loosest. The corresponding range of axial strain at peak axial stress was 1.8% (densest) to 12.0% (loosest). The final axial stress, at 14.0% axial strain, was about 2250kPa in all cases (Figure 4.4(a)). The graph of volumetric dilation against axial strain (Figure 4.4(b)) shows that the peak strength is associated with maximum rate of dilation. For the densest sample, the dilation angle at peak strength was nearly 14° compared with 0° for the loosest. The loosest sample simply contracts to a critical state. All the simulations showed a dilation rate of about 0° after 14.0% axial strain, indicating that a critical state had been reached. Dilation angle can be calculated by the equation below:

$$\sin\psi_{\max} = \frac{\delta\varepsilon_1 + \delta\varepsilon_3}{\delta\varepsilon_1 - \delta\varepsilon_3} \tag{4.7}$$

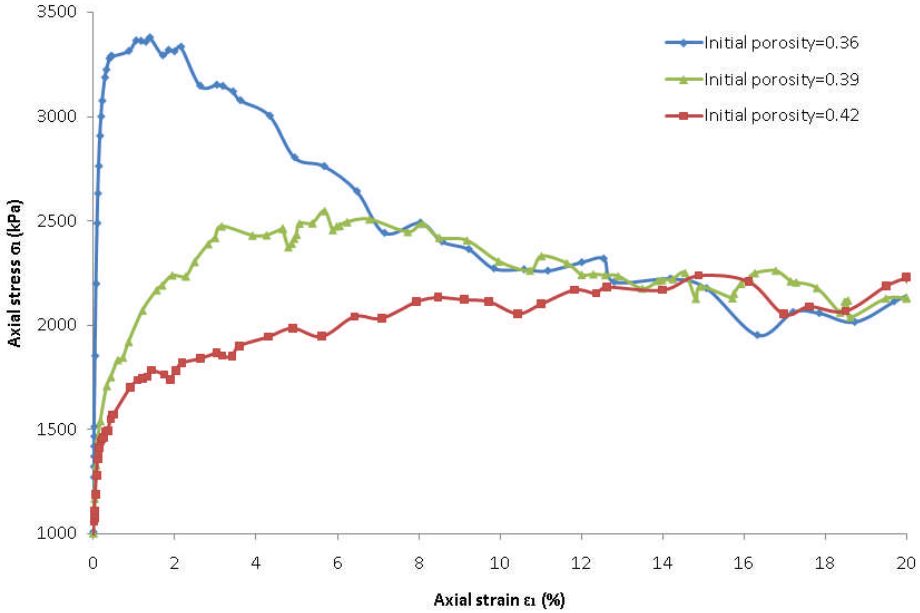

(a)

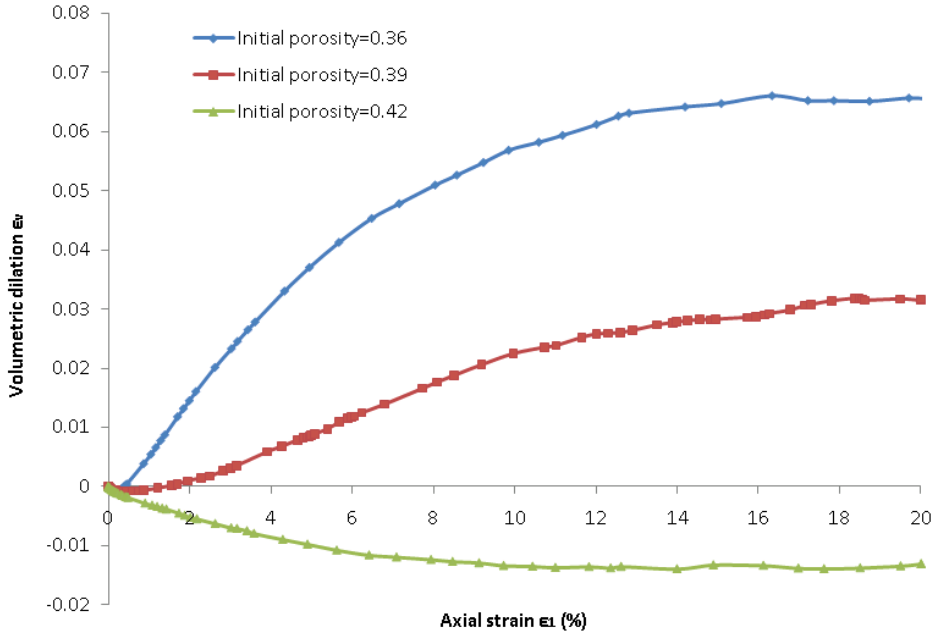

(b)

Figure 4.4: Axial stress and volumetric dilation of the samples with various initial porosities (a) Axial stress against axial strain (b) Volumetric dilation against axial strain

4.4 Influence of Particle Shape

The simulations described in this section involved numerical biaxial tests on samples comprising particles of spheres and two-ball clumps. The particle shapes in these simulations are shown in Figure 4.5. Each of the samples contained 7000 particles (there are around 14000 particles for the sample consisting of clumps) with friction coefficient 0.7. All samples were prepared at an initial porosity of 0.36 under a confining stress of 1000kPa. Figure 4.6 show the axial stress and the volumetric dilation against axial strain for each sample of spheres and clumps. The peak axial stress increases when the particle shape changes from sphere to two-ball clump, as would be expected owing to the increased opportunity for interlocking and dilation (Mitchell, 1993). Both the maximum angle of dilation ψ_{peak} (Figure 4.6(b): calculated according to Equation (4.7)) and the overall dilation of the sample during the simulation increased with changing the particle shape. The two initial stiffnesses from simulations in Figure 4.6(a) are quite similar, and then both curves reach peak strength at almost the same axial strain. The result using clumps gives larger peak stress and higher ultimate stress, giving a higher peak friction angle and critical state friction angle.

(a) (b)

Figure 4.5: PFC^{3D} model (a) single sphere as a particle; (b) two-ball clump as a particle

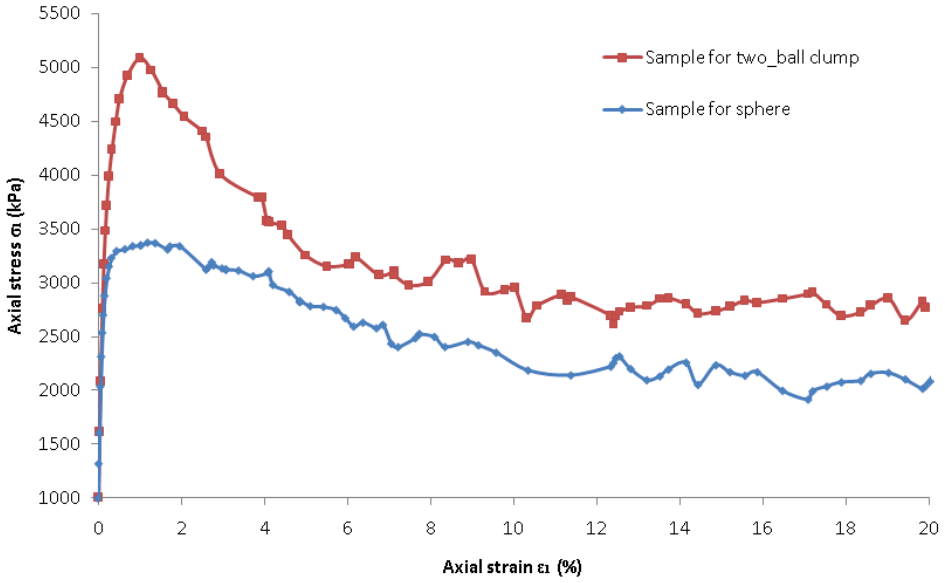

(a)

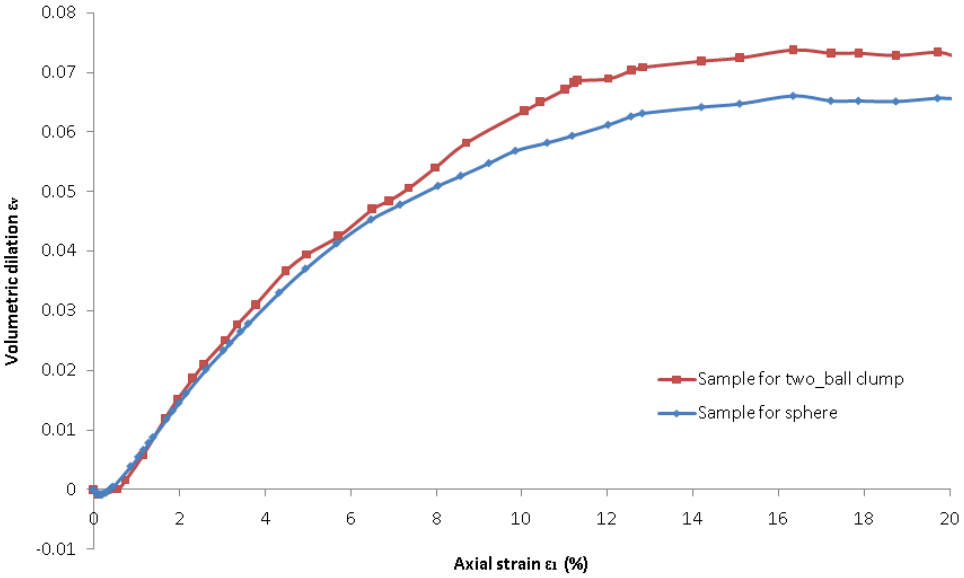

(b)

Figure 4.6: Axial stress and volumetric dilation of the samples with spherical particles and two-ball clumps (a) Axial stress against axial strain (b) Volumetric dilation against axial strain (Initial porosity=0.36)

Sample	Initial porosity	Particle friction coefficient and stiffness	
Sample of spherical particles	0.36	0.7	1×10^9N/m
	0.39	0.7	1×10^9N/m
	0.42	0.7	1×10^9N/m
Sample of two-ball clumps	0.36	0.7	1×10^9N/m

Table 4.1: The particle properties and porosity of the samples for DEM simulations in Figure 4.6

The simulations in Figure 4.6 used the samples of spherical particles and two-ball clumps. The information of particles and samples are listed in Table 4.1.

4.5 Influence of Interparticle Friction Angle

Interparticle friction is known to have a significant effect on the deformation behaviour of a soil (Lee and Seed, 1967). Further numerical biaxial test simulations were carried out on samples with particle friction coefficients of 0.3, 0.5 and 0.9, to complement the 0.7 simulation already reported. The initial sample porosity was kept at 0.36 and spherical particles were used in these simulations. The initial porosity of assembly was controlled by friction coefficients of 0.0 during artificial isotropic compaction. The samples include circa 7000 particles with a confining stress of 1000kPa.

The results (shown in Figure 4.7) show that interparticle friction has a large effect on the peak axial stress, as well as the overall sample dilation at the end of shear. Figure 4.7(a) shows the stress-strain relationship with different friction coefficients. The peak axial stress of each stress-strain curve increases

when the friction coefficient increases. Figure 4.7(b) shows that the volumetric dilation increases when the friction coefficient increases.

Comparison of the results of the simulations carried out to investigate the effect of particle shape and interparticle friction angle (Figure 4.6 and Figure 4.7) shows that increasing the particle friction coefficient dramatically increased sample peak axial stress and volumetric dilation, but did not affect the ultimate stress that much. Changing the particle shape from sphere to two-ball clump did not only affect the peak axial stress and volumetric dilation, but also the ultimate stress. The simulations in Figure 4.7 are summarised in Table 4.2 showing the particle properties and sample initial states of these simulations.

	Sample 1	sample 2	sample 3	sample 4
Particle friction coefficient	0.3	0.5	0.7	0.9
Porosity of the samples	0.36	0.36	0.36	0.36
Particle stiffness (N/m)	1×10^9	1×10^9	1×10^9	1×10^9

Table 4.2: The particle properties and porosity of the samples for DEM simulations in Figure 4.7

Therefore using a clump gives both higher peak stress and higher ultimate stress, and increasing coefficient of friction increases dilation and peak strength. These results are consistent with previous studies (Ni, 2003).

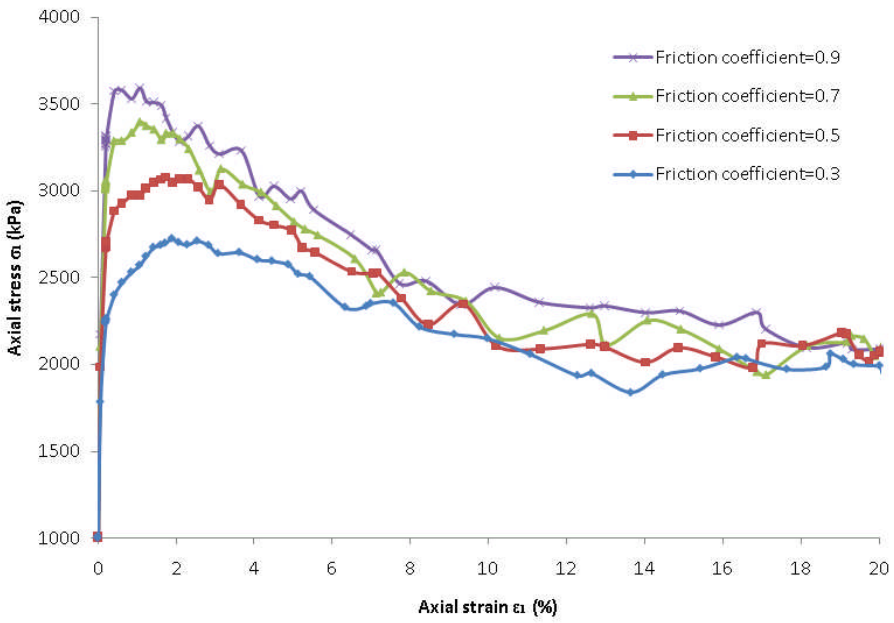

(a)

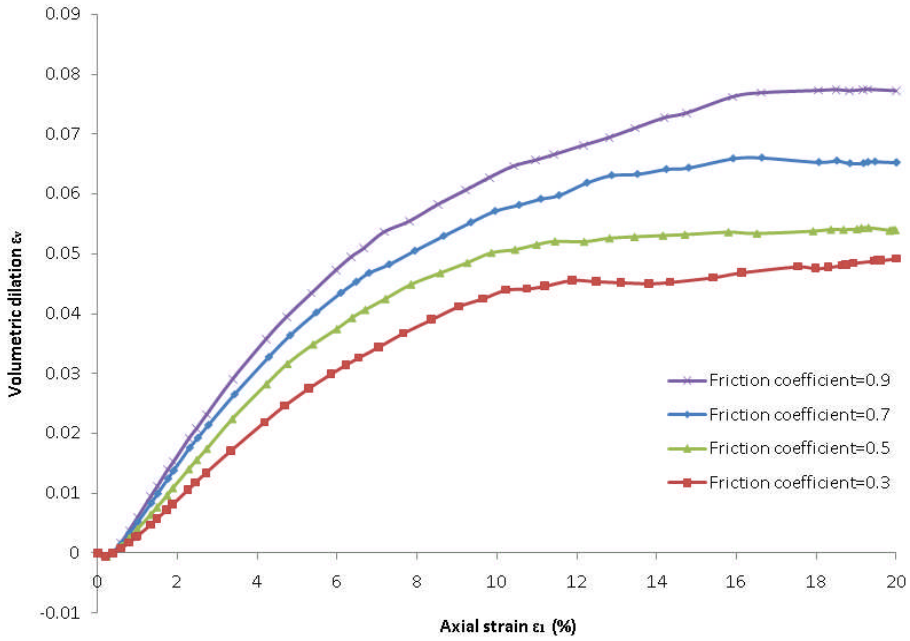

(b)

Figure 4.7: Axial stress and volumetric dilation of the samples with various particle friction coefficients (a) Axial stress against axial strain (b) Volumetric dilation against axial strain

4.6 Results and Discussion

4.6.1 Experimental data

Tatsuoka et al. (1986) performed a series of drained plane strain compression tests on saturated samples of fine angular to sub-angular sand (Toyoura Sand) at confining pressure 400kPa. The samples were prepared by the air-pluviation method with changing the angle δ of bedding plane to the σ_1'- direction during plane strain compression tests from 0 to 90 degrees. The equipment used in their tests is shown in Figure 4.8. The nominal initial sample dimensions are h_0 (height) =10.5cm, w_0 (length in the σ_3'-direction) =4cm and l_0 (length in the σ_2'-direction) =8cm.

The typical relationships between stress ratio, axial strain and volumetric strain are shown in Figure 4.1. These curves describe the results from anisotropic samples with different angle δ from 0 to 90 degrees. The DEM simulation results will be compared with these experimental results.

4.6.2 DEM simulations

DEM provides the possibility to investigate the mechanical behaviour of granular materials at both micro and macro level. Some results of the simulations are discussed with reference to the stress-strain behaviour observed in biaxial tests on real sand reported by Tatsuoka et al. (1986). The particles used for the simulation follow the relative particle size distribution of Toyoura sand (the sand tested in laboratory) but proportionally larger. The specified number of particles can be adjusted by changing the actual particle sizes in

proportion to the laboratory particle grading (Figure 4.9). Subsequently the relative dimensions of the particles in simulation are similar to that of the real sand. It reduces the number of particles in the simulation and the calculation time.

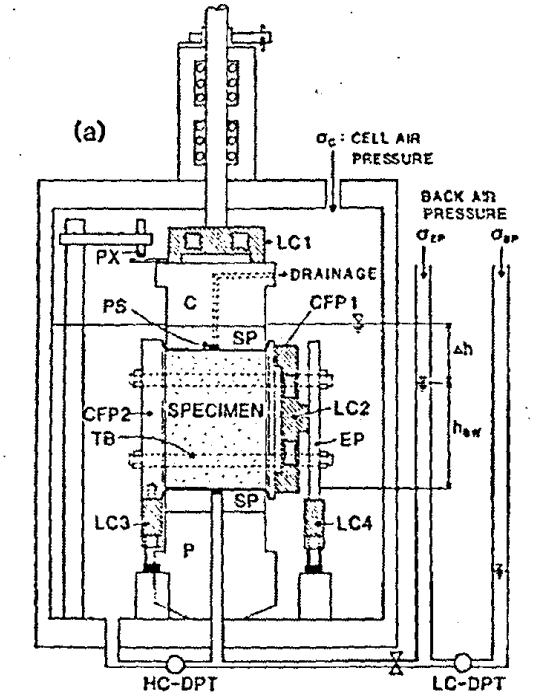

Figure 4.8: The equipment of plane strain compression tests (Tatsuoka et al., 1986)

The simulated sand particles using single spheres and two-ball clumps in the biaxial test have been shown in Figure 4.2. A clump is an agglomerate of overlapping spheres. Each clump here comprises two sphere particles of different sizes. R and r are the radii of the larger and smaller spheres respectively, and L is the distance between the centres of two spheres in each clump, such that L=R and r=0.75R. The clumps were formed by creating initial spheres, of the same size as the simulations using spherical particles. “Virtual spheres” were then created by deleting the initial spheres and creating a virtual

space by multiplying the initial sphere diameter by a factor of 1.27. Each "virtual sphere" formed the outermost possible boundary for each clump and the clumps were created in the "virtual spheres. The simulated sample dimensions were chosen to be the same as for the lab sample (105mm×40mm×80mm), except for the dimension in the plane direction (ie 105mm×40mm×20mm). This is to reduce the number of particles in each sample and reduce calculation time. The number of each particle size is adjusted (proportionally remaining the same), so that the specified number of particles fills the standard sample box at the chosen porosity, which is set by the user. It should be noted that the porosity set by the user may differ from the final porosity obtained in sample preparation and just before shearing, since the final size of the sample may change slightly after cycling to equilibrium. The initial state is defined such that after one numerical sample has been generated at the required porosity, a confining stress σ_0 of 400kPa is applied to all boundaries and the sample is allowed to come to equilibrium.

The properties of all six walls are assumed to be same. The wall friction coefficient is 0 and wall normal stiffness and shear stiffness were chosen to be the same as particle stiffness: 1e6 N/m. The maximum particle radius for each sample was 2.05mm and the minimum radius was 0.5mm, which was about 10 times the size of the real sand (Figure 4.9). The loading was carried out by moving the top and bottom walls at a rate 0.0002mm/s after the sample reached the initial state. The confining pressure is applied to the left and right vertical walls. The axial stress is applied to the top and bottom walls. The sample front and back walls were fixed to give plane-strain conditions. In each of the tests, the sample has about 13000 particles with spheres or two-ball clumps.

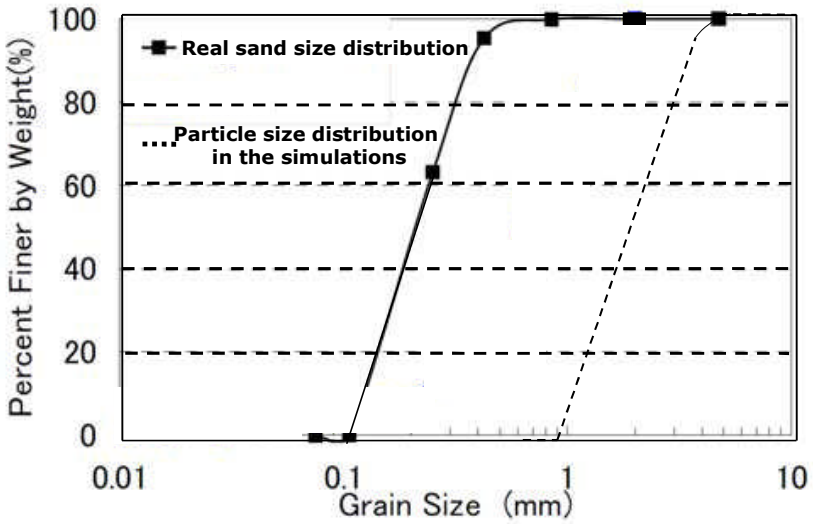

Figure 4.9: Particle size distributions of numerical sample and real sand

4.6.3 Results

The purpose of these simulations is to try to model using DEM, experimental biaxial test results, by studying the effects of various parameters. The effects of interparticle friction and particle shape will be discussed. Three simulations using spheres with particle friction coefficients of 0.5, 0.7, and 0.9 were performed with sample initial porosity 0.411 and confining pressure 400kPa as the initial state, the results are shown in Figure 4.10. However these sample strengths are much lower than the experimental results, see Figure 4.11. Therefore the influence of particle shape on the sample strength was studied.

The real sand particle is irregular and involves more complex intergranular interactions than between spheres. Therefore clumps were used in the simulation. The shape of the clump is shown in Figure 4.2(b). The simulation results using both spherical particles and clumps are compared with the experimental result from Tatsuoka et al. (1986). The particle properties and initial porosities used in each sample are shown in Table 4.3.

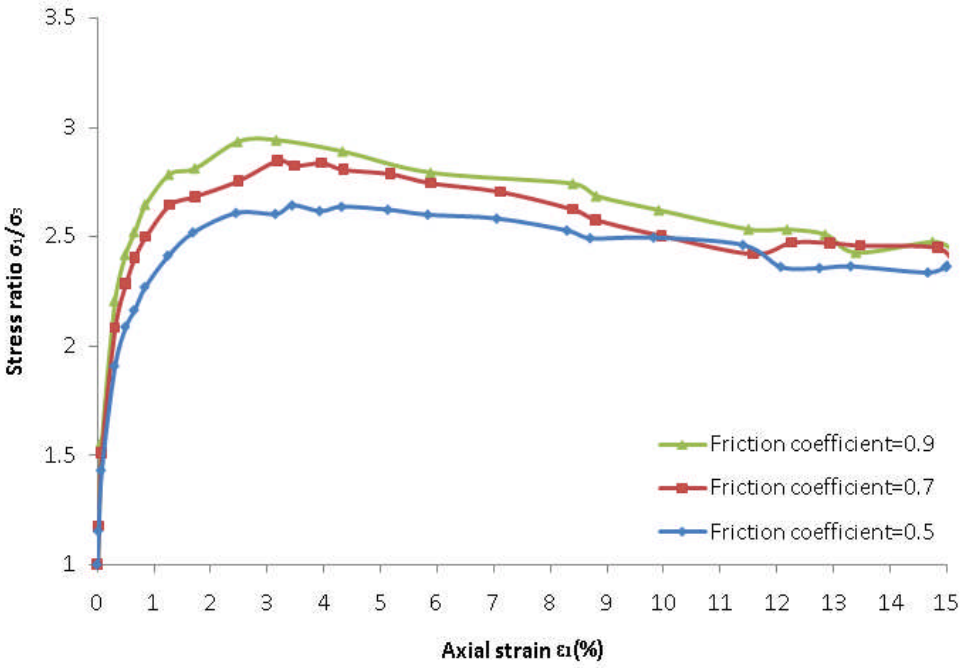

Figure 4.10: Stress ratio against axial strain (using spheres, σ_3=400kPa)

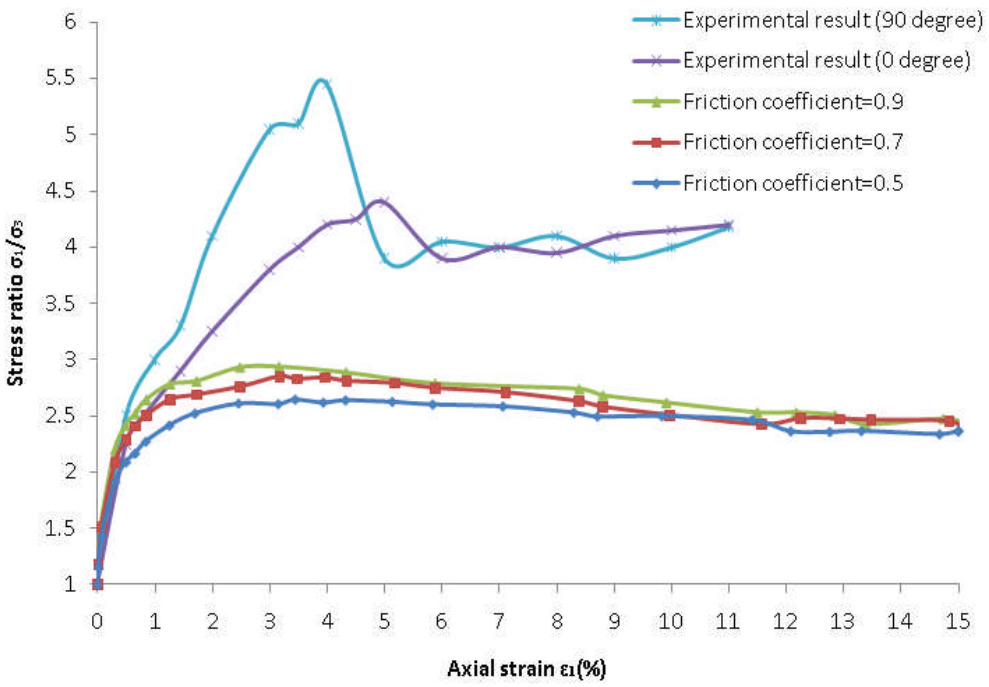

Figure 4.11: Results of stress ratio against axial strain between experimental test data and DEM simulations using spheres (σ_3=400kPa)

The samples using in the laboratory test were anisotropic, but the samples using in the simulations are isotropic. Therefore two results were selected from the experimental results (Figure 4.1): δ=90º (top line in Figure 4.12) and δ=0º (second line to top in Figure 4.12). As shown in Figure 4.12, the bottom line is the simulation result with spherical particles and the simulation result by using clumps is shown as the curve above. The simulation result with spherical particles is selected from Figure 4.10 with particle friction coefficient 0.7. The simulation results using spheres and clumps are quite similar. We can see that they reach the peak axial stress almost at the same axial strain before heading towards a critical state. The result using clumps gives both a larger peak stress ratio and a higher ultimate stress ratio (critical state angle of friction).

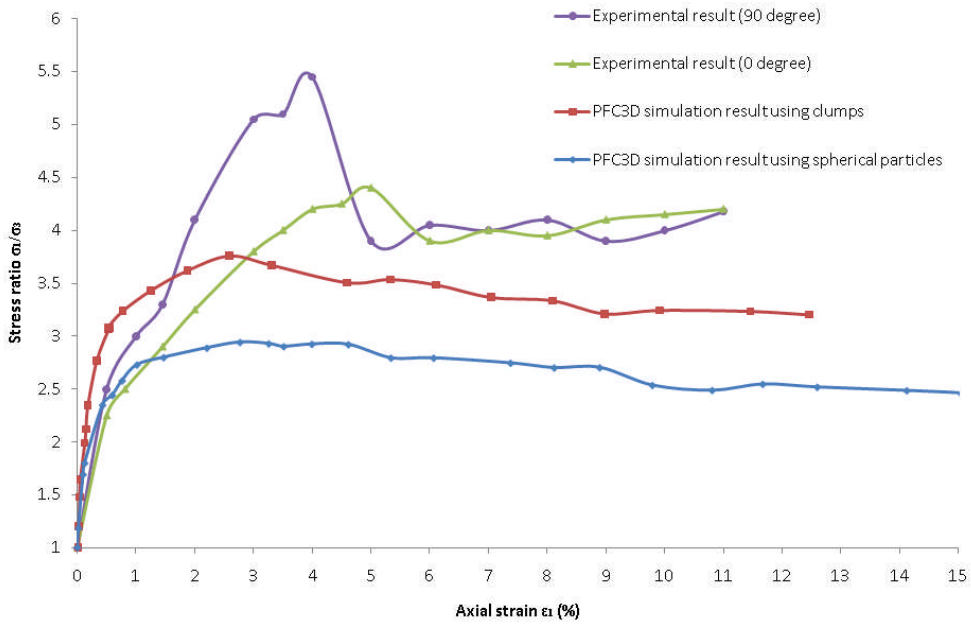

Figure 4.12: Comparison between results from PFC^{3D} simulation and experimental data (σ_3=400kPa)

Sample	Initial porosity	Particle friction coefficient and stiffness	
Sample of spherical particles	0.41	0.7	1×10^6N/m
Sample of two-ball clumps	0.41	0.7	1×10^6N/m

Table 4.3: The particle properties and porosity of the samples for DEM simulations in Figure 4.12

The simulations in Figure 4.10 show that the friction coefficient of a particle is an important parameter to affect the sample properties. The shear strength and friction angle of the sample both increase with the increasing particle friction coefficient. Therefore, another DEM simulation using particle friction coefficient 0.9 is carried out to obtain the particle friction coefficient effect on the behaviour of sample consisting of clumps, as shown in Figure 4.13. Table 4.4 lists the particle properties and initial porosities of each sample.

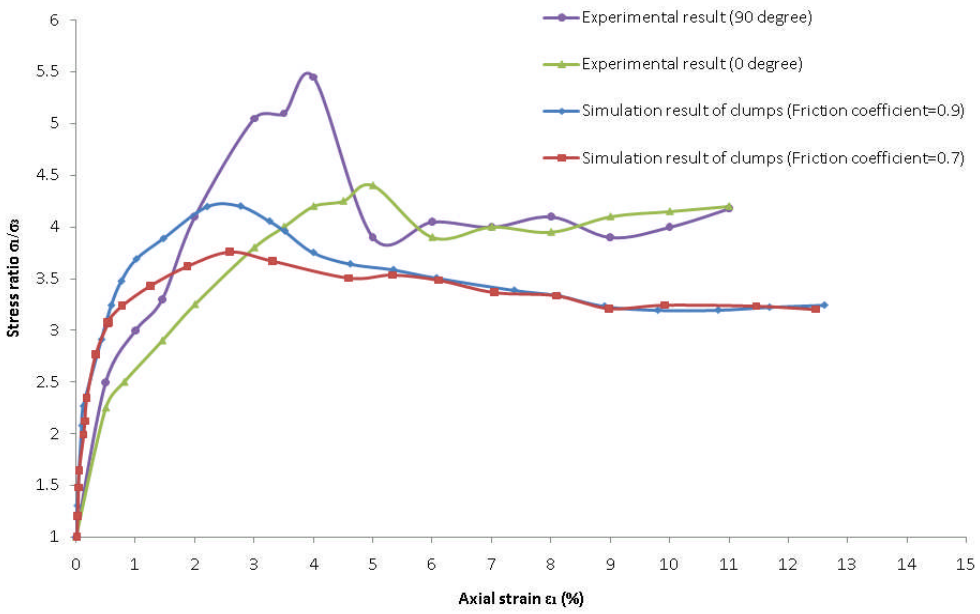

Figure 4.13: Comparison between results from PFC^{3D} simulation using clumps and experimental data (σ_3=400kPa)

Sample	Initial porosity	Particle friction coefficient and stiffness	
Sample of two-ball clumps	0.41	0.9	1×10^6N/m
Sample of two-ball clumps	0.41	0.7	1×10^6N/m

Table 4.4: The particle properties and porosity of the samples for DEM simulations in Figure 4.13

As shown in Figure 4.12, the simulated mechanical behaviour of granular materials is compared with those observed from the laboratory tests. The material used in the laboratory test is a sub-angular sand (Toyoura sand). The particle shape must be the principal reason for affecting the material behaviour in the simulations. Figure 4.12 shows the effect of particle shape. It can be seen that the stress ratio-strain curve for the clumps is closer to the experimental test result. The effect of particle friction coefficient on behaviour of sample using clumps shows that the stress ratio-strain curve for particle friction coefficient 0.9 is closer to the experimental test data (Figure 4.13). The strength of sample increased when the particle friction coefficient increased, but the ultimate axial stress ratio did not affect much by the particle friction coefficient.

4.7 Conclusions

In this chapter, granular material behaviour is investigated by the numerical approach with the aid of DEM. The mechanical response of cohesionless granular material under monotonic loading is studied. DEM has been used to simulate successfully the typical granular material behaviour in the plane-strain biaxial compression tests and compares well with experimental test results. The

simulations show that particle properties have a significant effect on the soil stress-strain behaviour.

Using the soil element to simulate the soil behaviour is a very complex problem, where many factors should be considered. These simulations are very important for the micro parameters research. The shear strength and friction angle of the sample increases when the particle friction coefficient increases and when the shape is irregular. The results are valuable for developing the constitutive model of the soil. So DEM can simulate the biaxial test properly and the suitable soil properties can be obtained.

CHAPTER 5

DEM SIMULATION OF CAVITY EXPANSION

5.1 Introduction

This chapter describes the simulation of cylindrical cavity expansion in granular materials using the discrete element method (DEM). Cavity expansion analysis focuses on the cavity pressure needed to expand a cavity in a material medium by a certain radial displacement. The problem of expansion of cylindrical cavities has been dealt with by many investigators in the last 50 years, in connection with its potential applications to a number of practical problems in mechanics and engineering. Three distinct zones can be considered during the stress increases depending on the strain levels. Figure 5.1 shows the three zones (Salgado et al., 1997). In the linear elastic zone, the soil linear elastic and the strains are very small. Beyond the nonlinear elastic zone, the material has yielded and strains are plastic (Salgado et al., 1997).

For granular material, the discrete element method is a useful tool for studying cavity expansion, based on discrete particle properties. This numerical analysis technique starts with basic constitutive laws at interparticle contacts and the macroscopic response of particle assemblage under loading can be provided. Few studies have been carried out on analysis of cavity expansion on granular

material. The dynamic problem of the symmetric expansion of a cylindrical or spherical cavity in a granular material was studied by Osinov (2005). This problem was solved by a finite-difference technique. A description of soil behaviour can be achieved by developing a constitutive model and a satisfactory technique for measuring the required soil properties. As far as granular soils are concerned, DEM is popular used to simulate the granular soil behaviour. Because of the micro properties can be defined in DEM which is very difficult to describe in the other method. As the thesis mentioned in the beginning section, DEM has succeeded used to simulate the penetration test. The penetration test is an in situ testing method used to determine the geotechnical engineering properties of soil. The penetration test can be considered as an axisymmetric problem and the mechanism is related to the cavity expansion (Huang and Ma, 1994). Therefore, DEM might be used in the cavity expansion simulation. In this research, PFC^{3D} is used to simulate the soil behaviour in the cavity expansion.

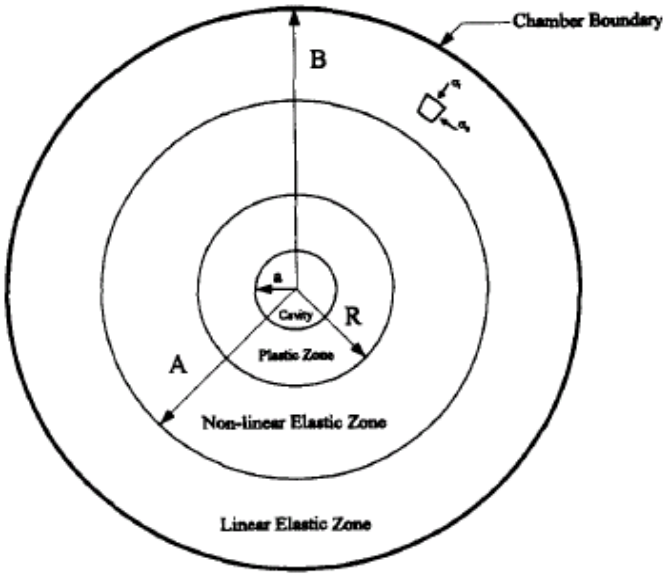

Figure 5.1: Cavity expansion generates plastic, nonlinear elastic and elastic zone (Salgado et al., 1997)

5.2 Modelling Procedure

The DEM code PFC^{3D} was used to simulate cylindrical cavity expansion on samples consisting of spheres (Figure 5.3). For this situation, which is axisymmetric, a quarter of the sample was generated and loaded by the internal circular boundary using a constant strain rate. A quarter of the geometry was chosen so as to have vertical and horizontal boundaries to align with the axes for simplicity. That is reduces calculation time significantly. To investigate the effect of sample shape, one simulation of full circle was compared with that of a quarter. The minimum particle radius for each sample was 0.075m and maximum radius was 0.1m. The particle friction coefficient is 0.7 and the normal stiffness and shear stiffness of particles are 1×10^9N/m. The density of the particles is 2650kg/m^3. The results were shown in Figure 5.2. It has been shown that there is not a large effect on the result, but it can save a lot of calculation time using a quarter of the sample. Therefore a quarter of the sample was used for the other simulations in this thesis for saving the calculation time.

The velocity of the external boundary was automatically controlled by a servo-mechanism (see Appendix) to keep a constant external pressure (Figure 5.4). Stresses on the walls are determined from the particles contact forces acting on them. Six walls were generated as sample boundaries, as shown in Figure 5.5. The normal stress on each wall was calculated by the summation of the normal contact forces acting on the wall divided by the area of the sample where the wall was located. The wall friction coefficient is 0 and wall normal stiffness and shear stiffness are 1×10^9 N/m. The samples had dimensions of

approximately 13.0m external diameter × 2.0m internal diameter × 1.0m high with more than 7000 particles in each sample. For each simulation, about 2 weeks are needed using computer with Intel(R) Core(TM)2 CPU 6320 @1.86GHz, 1.97GB of RAM and 250GB memory. It also depends on the number of particles, particle stiffness and the particle size.

The same particle properties are used as described before. The samples were generated by the particle radius expansion method. This is used to place a specified number of particles at random coordinates within a given space. Generate the particles with small diameter first and then multiply a ratio to get the design diameter particle because a new particle will not be placed if it would overlap another particle or a wall.

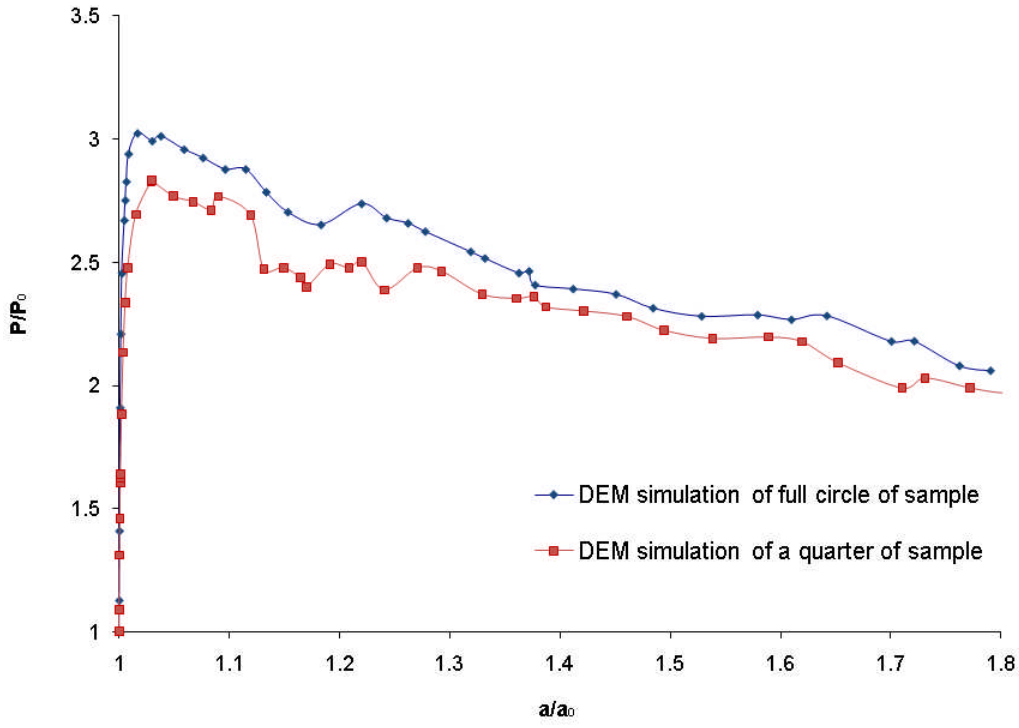

Figure 5.2: Cavity expansion simulations using full circle and a quarter of the sample

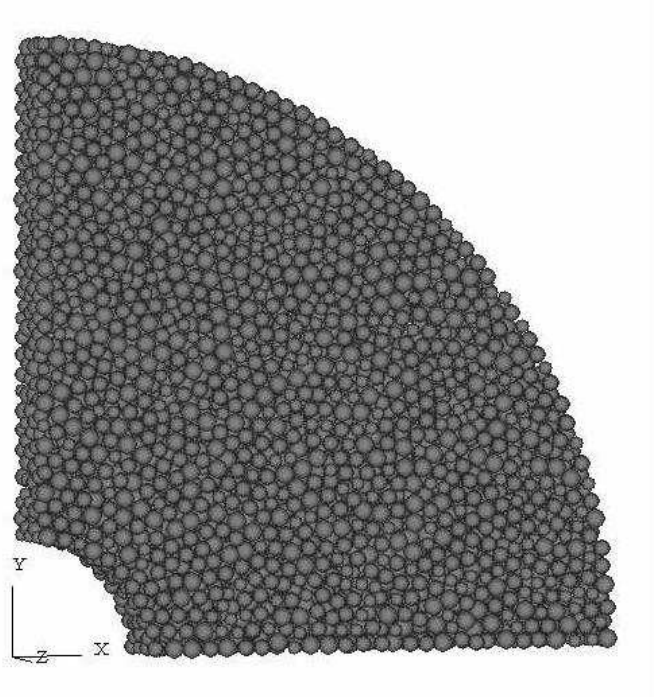

Figure 5.3: DEM sample for cavity expansion

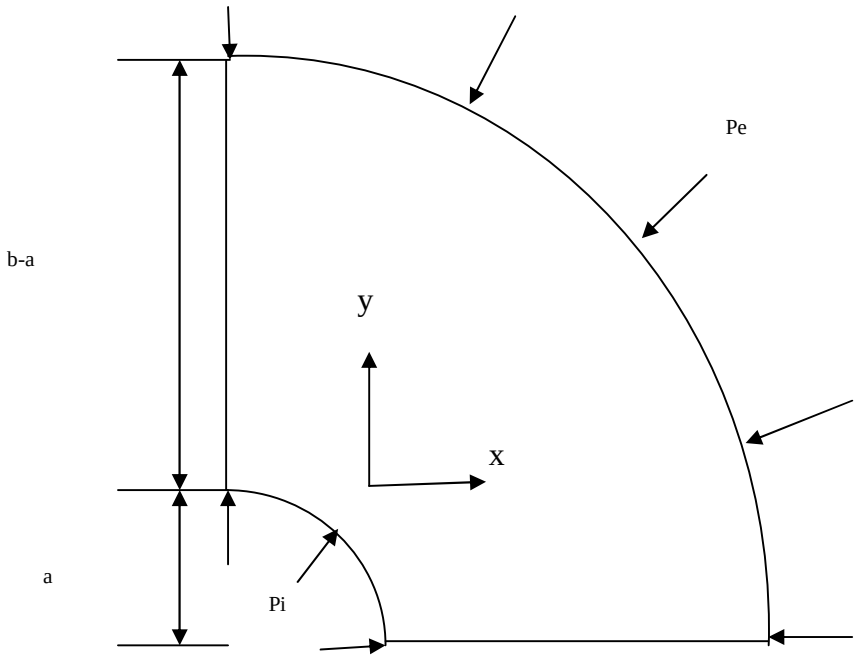

Figure 5.4: Schematic illustration for cavity expansion

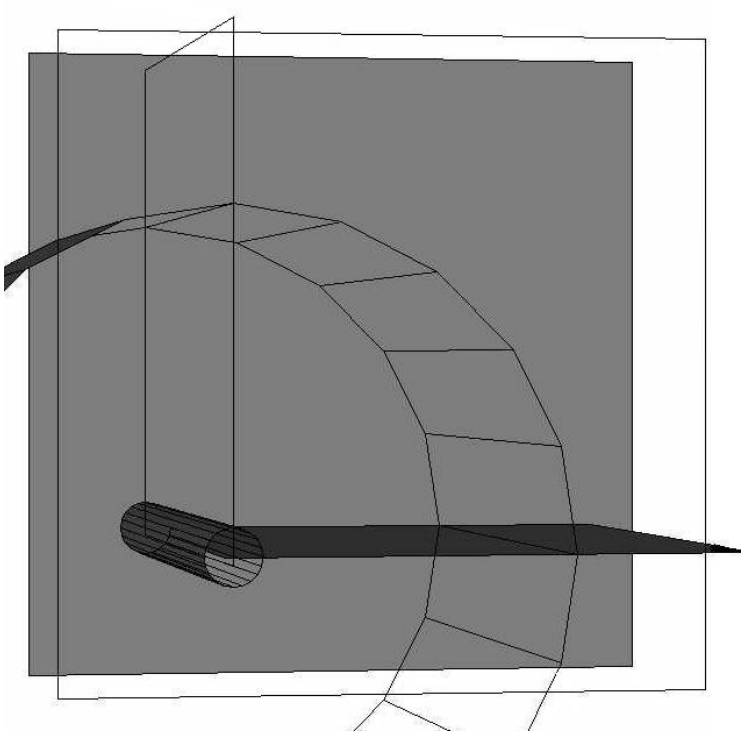

Figure 5.5: Six walls of DEM sample

After the sample is generated, the sample stress state is adjusted to $P_i=P_e=P_0$. P_0 is the initial cavity pressure. P_i and P_e are defined as the internal and external pressures. The loading was carried out by moving the internal wall at a rate of 0.01m/s after the sample reached the initial state. The sample thickness was fixed by front and back walls to simulate the plane-strain condition. An initial cavity pressure of 20MPa was used. For the initial cavity pressure $P_i=P_e=P_0=20$MPa, four samples were generated with different initial porosities (0.36, 0.38, 0.40 and 0.42). The initial porosities were calculated by a measurement sphere which is a function available in PFC^{3D}. Many measurement spheres are generated to cover the whole sample. The finial porosity is calculated using the average value of these porosities. The various initial porosities of these samples result from the different particle friction coefficients (0.0-0.7) during the generation of each sample. Once the initial

state of the sample is reached, the particle friction coefficient is changed to 0.7 to study the effect of porosity on the behaviour. Different particle friction coefficients of 0.1, 0.3, 0.5 0.7 and 0.9, were used to examine the effect of this particle property on cavity expansion curves when the sample initial porosity is 0.36. Two particle shapes (as for the biaxial test simulations) were used to investigate the effect of particle shape. The particle properties and sample initial states are listed in Table 5.1.

5.3 Effect of Particle Parameters and Loading Conditions

5.3.1 Effect of speed of loading

In this research, all the simulations were operated with particle rotation allowed. It is well known that particle rotation plays an important role in the development of shear bands (Bardet and Proubet, 1992; Oda, 1997). While the degree of particle rotation is a factor of particle shape, it is easy to ascertain that non-spherical particles can cause more interlocking than spherical particles. The interlocking gives higher rolling resistance and the peak and critical state angles of friction will be higher than for an aggregate of spherical particles. The more interlocked sample will also give a higher yield pressure (Oda and Iwashita, 2000). This part will be discussed in the section 5.3.5. Loading velocity is another important parameter in the simulations. It will influence the macro behaviour of the sample significantly. A suitable loading velocity needs to be determined for each sample in the simulations. The priority in choosing this parameter is to minimise calculation time. When the loading velocity is slow enough, both the mean contact force and mean unbalanced force approach a constant value and if the velocity is reduced further, the sample response does

not change much. For these simulations in this research, loading velocities of 0.001m/s, 0.005m/s, 0.01m/s, 0.05m/s, 0.1m/s have been used. It was found that the fastest velocity that could be applied without significantly affecting the results was 0.01m/s.

5.3.2 Effect of number of particles

The minimum number of required particles also needs to be determined. To examine the effect of the number of particles in the sample, simulations with samples comprising 3000, 7000, 10000 and 15000 particles were carried out. To run one simulation with 15000 particles, extra 2 weeks are needed. In view of the computer time taken to run an analysis with a very large number of particles, further simulations were carried out on samples comprising 7000 particles only. This was considered reasonable in view of the relatively small changes in the behaviour found by using 10,000 or 15,000 particles.

5.3.3 Effect of initial sample porosity

It is well known that the sample porosity can have a great influence on the soil behaviour. Figure 5.6 shows the results of four simulations carried out with initial porosity, n, of 0.36, 0.38, 0.40 and 0.42, in terms of P/P_0 against $\mathbf{a}/a_0$. P is defined as the cavity pressure and P_0 is the initial cavity pressure. Also **a** is defined as the radius of the cavity during loading and a_0 is the radius of the cavity at initial unloaded state. In the case of the dense sample (n=0.36, n refers to porosity) there is a pronounced peak cavity pressure ratio of about 3.1 attained at an internal radius ratio of 1.15. Before the peak, the cavity pressure increases as the internal radius increases. After the peak, the cavity pressure

decreases as the internal radius increases. For the sample (n=0.38, medium dense), a maximum cavity pressure ratio 2.8 is attained at an internal radius ratio of 1.2. For the sample (n=0.40), the maximum cavity pressure is attained at an internal radius ratio of 1.3. For the loose sample (n=0.42), the maximum cavity pressure ratio 2.2 occurs at a large internal radius ratio and there is no significant occurrence of a peak cavity pressure prior to this. Around 7000 particles were generated for each sample. The initial cavity pressure for these samples was 20MPa and b_0/a_0 was around 6. The final cavity pressure ratio, at 1.7 internal radius, was about 2 in all cases.

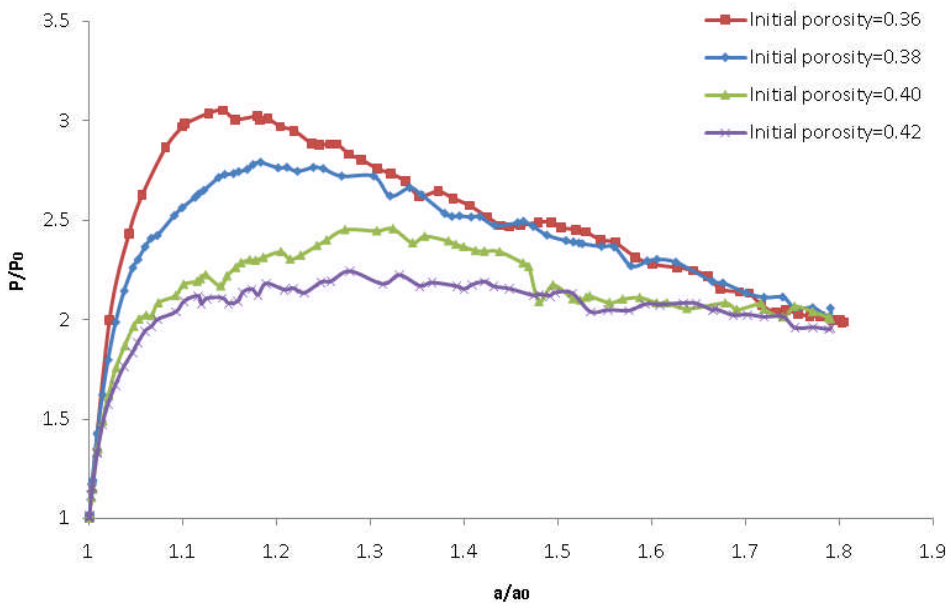

Figure 5.6: The cavity expansion curves of different sample initial porosities using DEM simulations

5.3.4 Effect of initial sample thickness

It can be seen that this is a plane-strain problem, so the thickness of sample is fixed. For obtaining the thickness effect on the behaviour of cavity expansion,

3 simulations with thickness of 0.5, 1 and 2m were carried out. The other particle properties were given in the beginning. The simulation results are shown in Figure 5.7. It can be seen that the thickness of sample did not affect the cavity expansion behaviour much if the number of the particles is enough. Therefore, the suitable thickness of the sample can be determined regarding the geometry of the sample and the number of particles.

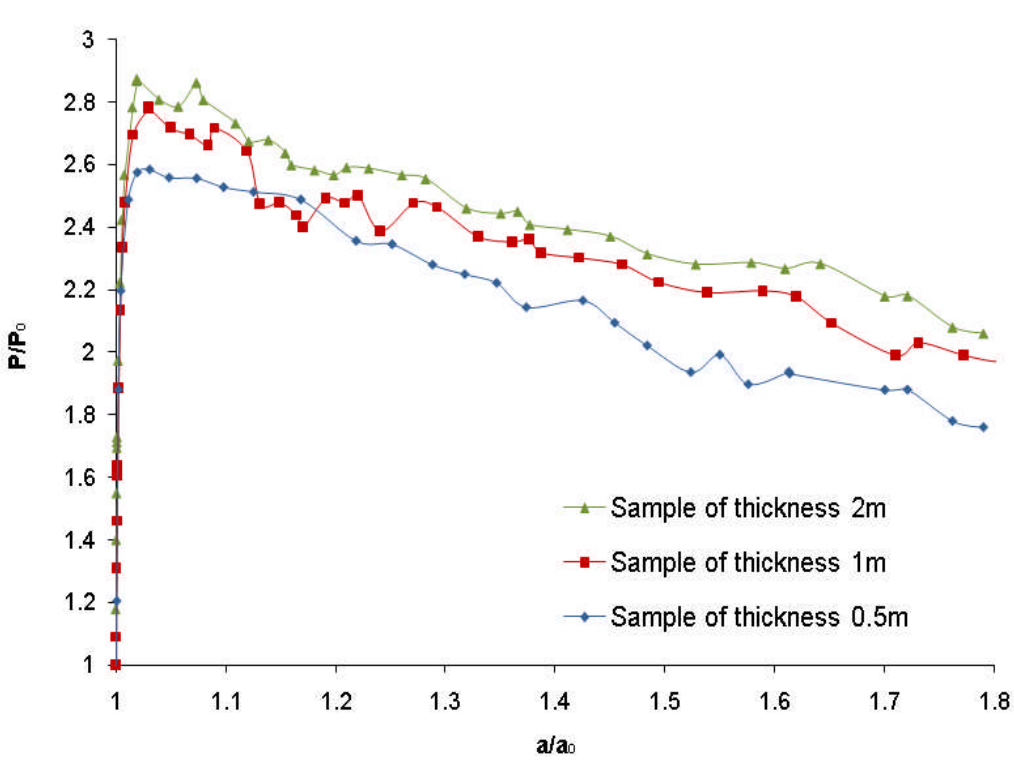

Figure 5.7: The cavity expansion curves of different sample initial thickness using DEM simulations

5.3.5 Effect of particle friction coefficient

The biaxial test simulations showed that friction coefficient plays a significant role in the DEM simulations. The stress-strain response of an assembly not only depends on the particle shape but also on interparticle friction. The effect

of particle shape will be discussed in the next section. In this section, a serious of simulations was carried out to investigate the effect of particle friction coefficient. The sample was prepared using the same method which was described before and when the sample initial state was reached, the particle friction coefficient was changed to 0.1, 0.3, 0.5 0.7 and 0.9 respectively for each sample. Thus every time the same sample existed before loading. The different particle friction coefficients (varying from 0.1 to 0.9) were applied to the dense sample (initial porosity=0.36). The effect of particle friction coefficient on the cavity expansion simulations is shown in Figure 5.8. It can be seen that the friction coefficient has a large effect on the cavity expansion behaviour when the friction coefficient is lower than 0.7. However, it makes little difference to the cavity pressure when the friction coefficient is increased from 0.7 to 0.9.

Figure 5.8 show that particle friction coefficient had a large effect on the peak value of cavity pressure. The peak value of cavity pressure increases when the particle friction coefficient increases. However, the cavity pressure ratio (P/P_0) at the end was approximately of 2 in all cases. Although the samples had not quite reached critical states, this strongly suggests that the cavity pressure at the critical state would not be significantly affected by the particle friction coefficient. The peak cavity pressures were obtained almost at the same internal radius ratio (a/a_0=1.15) irrespective of particle friction coefficient; this is a different observation to the simulations with different initial porosities and coefficient of friction of 0.7.

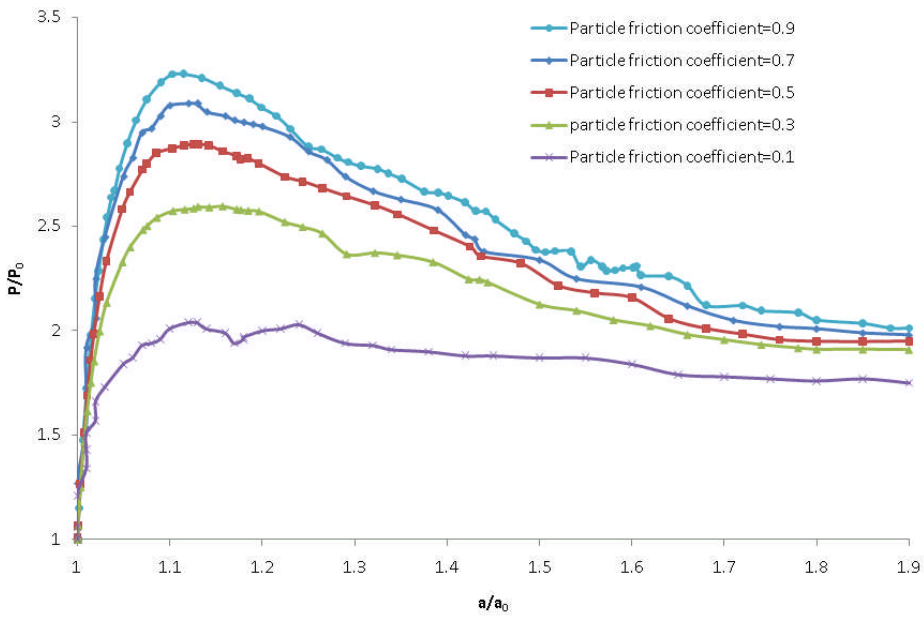

Figure 5.8: Cavity expansion curves for different particle friction coefficients using spheres with porosity n=0.36

5.3.6 Effect of particle shape

Particle shape plays a key role in the behaviour of granular materials. Previous studies (Ting et al., 1989; Ng and Dobry, 1992; Rothenburg and Bathurst, 1992) have shown that particle shape has a great influence on the mechanical behaviour of granular materials and using spheres to represent each grain is not enough for granular materials comprising angular particles. This section presents a simple particle shape by using two balls of different sizes to form a clump, in order to show the effect of the particle shape on the inhomogeneous stresses induced within the particle assembly. The result of a cavity expansion simulation on clumps is compared with that for cavity expansion on spheres and the effects of the particle shape on contact distribution and particle displacements are studied.

The particle shape used in these simulations is the same as in the biaxial test simulation in chapter 4, shown in Figure 4.5. Apart from the particle shape, the samples were generated exactly same with the procedure described before. A quarter of the sample was generated and loaded by the internal circular boundary using a constant strain rate. The velocity of the external boundary was automatically controlled by a servo-mechanism to keep a constant external pressure. Figure 5.9 shows the simulated samples for spheres and two-ball clumps. The sample has dimensions of approximately 13.0mm external diameter, 2.0mm internal diameter and 1.0mm high. Figure 5.9(a) shows the sample with 7696 spheres. The normal and shear stiffness (liner-elastic) of the spheres were set to be 1×10^9 N/m and the stiffness of the walls were set to have the same value with the spheres. The particle friction coefficient was 0.7 and the density of the spheres was 2650kg/m^3. The clumps were formed by replacing the spheres. “Virtual spheres” were created by deleting the initial spheres and creating a virtual space by multiplying the initial sphere diameter by a factor of 1.27. Each “virtual spheres” formed the outermost possible boundary for each clump and the clumps were created with in the “virtual spheres”. Figure 5.9(b) shows the sample containing 7696 clumps (15392 balls). For the clumps, the stiffnesses and coefficients of friction used were the same as for the samples on spheres. The initial porosity was 0.36 for both samples of spheres and clumps. It should be note that for the clumps, the particle friction coefficient during sample preparation was set to a little higher (particle friction coefficient=0.1) than that for the sample of spheres during compaction, in order to obtain the same initial porosity as the spherical particle sample.

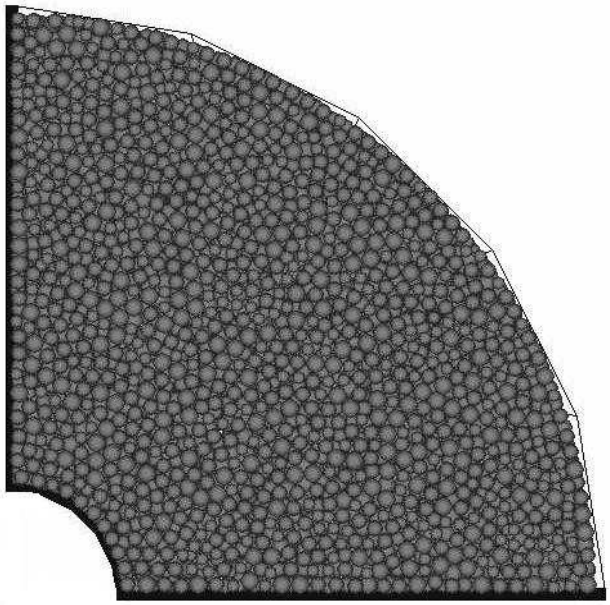

(a)

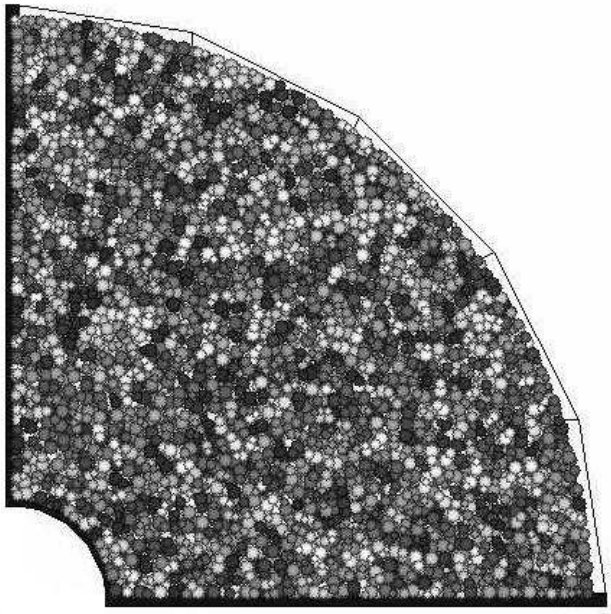

(b)

Figure 5.9: Sample for cavity expansion simulations using (a) spheres and (b) two-ball clumps

There is a contribution to the mass in the overlapping region from each of the overlapping balls. This may not influent the mechanical behaviour of the clumps under static loading. However, when the dynamic effect of the clumps is significant, the influence of mass due to overlapping balls will become significant. In such dynamic simulations, density can be scaled to give the correct particle mass, but the distribution of mass will be incorrect, leading to incorrect moments of inertia and hence rolling resistance. In these simulations, density is not scaled to fit correct mass.

Figure 5.10 shows the contact forces for each of the samples under compaction. It can be seen that the contact forces are reduced for the clumps, and more homogeneous for the sample consisting of more complex shape particles. This is because the higher number of contacts per particle for the sample of two-ball clumps leads to a more homogeneous stress distribution.

Figure 5.11 and Figure 5.12 show the contact forces for the spheres and clumps before and after loading respectively. It is noted that the number of contacts does not change much during the loading. The magnitude of the mean contact force for sample of clumps is less than that for the sample of spheres, because of the higher number of contacts per particle for the sample of clumps. It should be noted that the maximum contact force for the clumps is higher than that for the spheres.

Figure 5.13 shows the particle displacement vectors for the sample of spheres and two-ball clumps drawn at the same scale. It can be seen that the displacements of these samples on the side of internal wall and inside of the sample are larger than those displacements on the other positions and the

displacement are generally outwards. The difference between sample of spheres and clumps can be attributed to the interlocking provided by the three-dimensional clumps, which affects the rolling resistance. The higher number of balls in the sample consisting of two-ball clumps leads to more displacement vectors.

Sample	Initial porosity	Particle friction coefficient and stiffness	
Sample of spherical particles	0.36	0.1	1×10^9N/m
	0.36	0.3	1×10^9N/m
	0.36	0.5	1×10^9N/m
	0.36	0.7	1×10^9N/m
	0.36	0.9	1×10^9N/m
	0.38	0.7	1×10^9N/m
	0.40	0.7	1×10^9N/m
	0.42	0.7	1×10^9N/m
Sample of two-ball clumps	0.36	0.7	1×10^9N/m

Table 5.1: The particle properties and the sample initial states

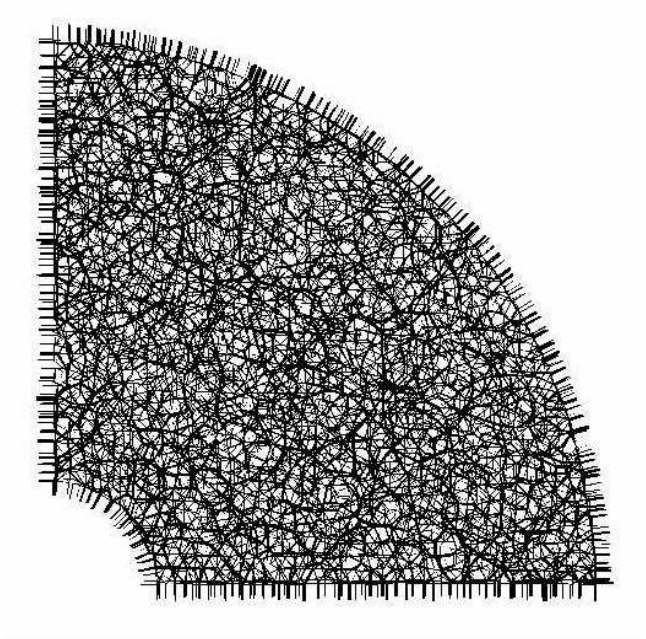

(a)

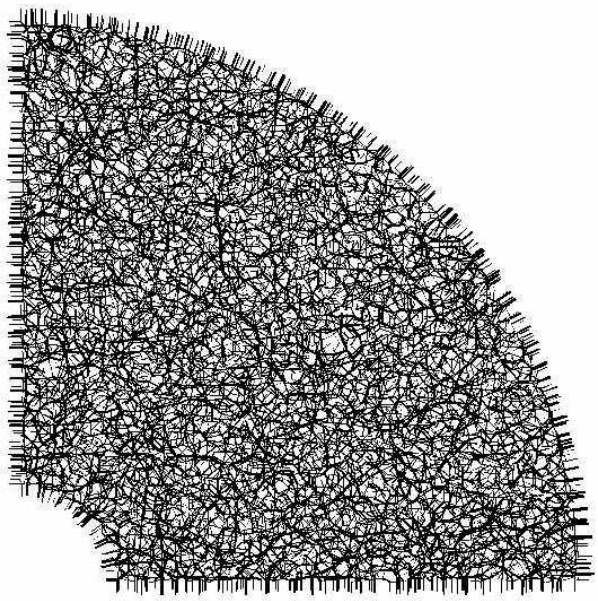

(b)

Figure 5.10: Contact forces for (a) spheres, (b) two-ball clumps, drawn to the same scale

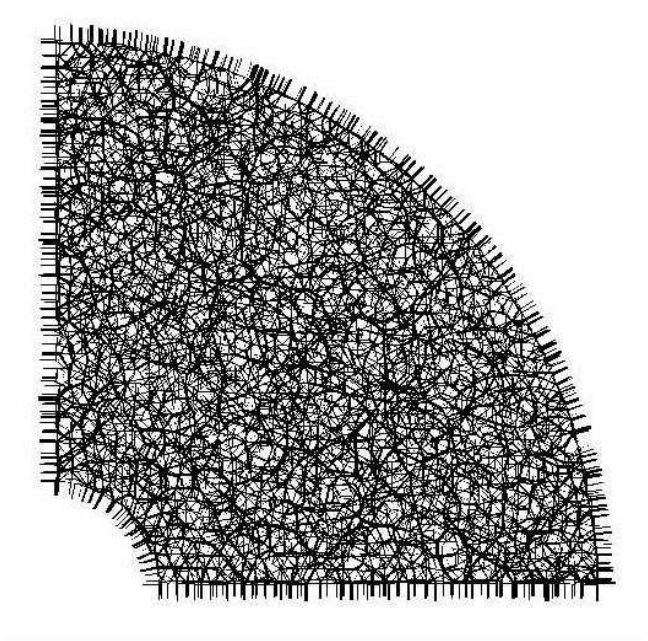

(a)

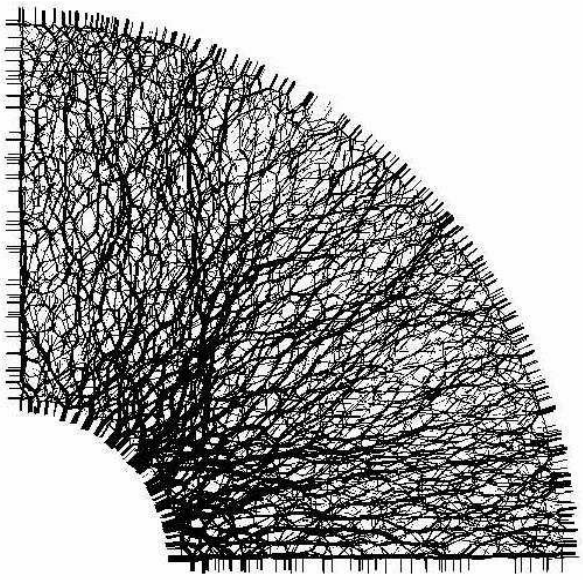

(b)

Figure 5.11: Contact forces for sample of spheres (a) before loading (maximum contact force=3.114×10^6N, mean contact force=5.393×10^5N, number of contacts=30693); (b) after loading (maximum contact force=5.953×10^6N, mean contact force=6.647×10^5 N, number of contacts=29335).

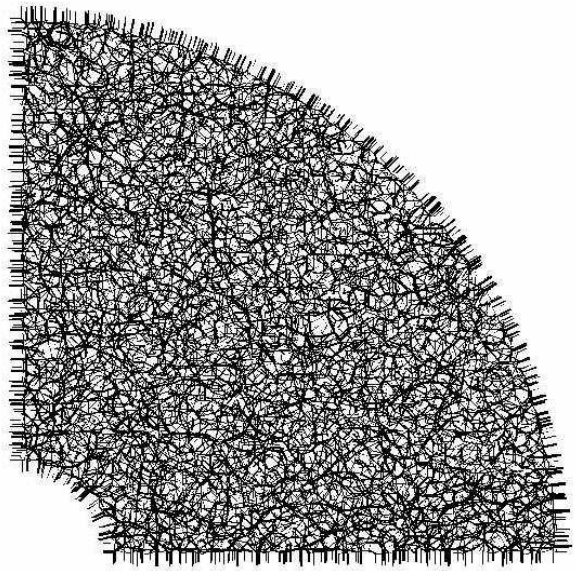

(a)

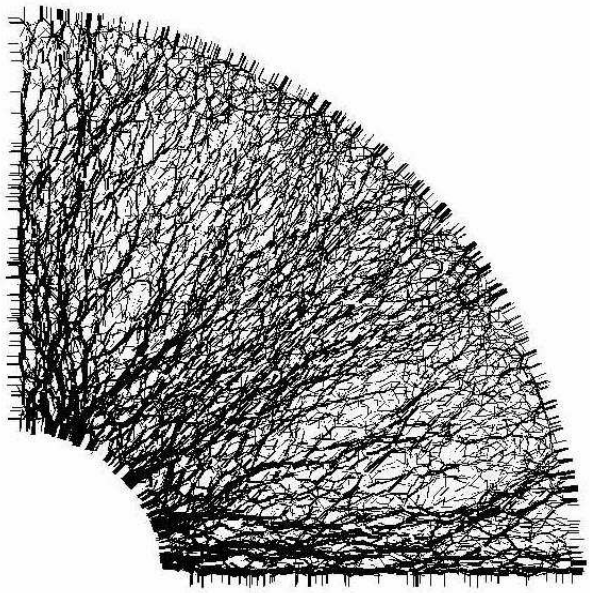

(b)

Figure 5.12: Contact forces for sample of clumps (a) before loading (maximum contact force=3.290×10^6N, mean contact force=4.685×10^5N, number of contacts=61452); (b) after loading (maximum contact force=9.941×10^6N, mean contact force=5.870×10^5N, number of contacts=58067).

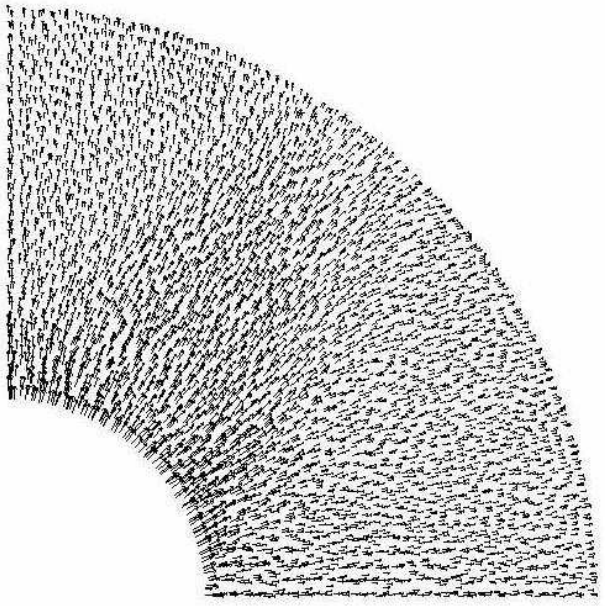

(a)

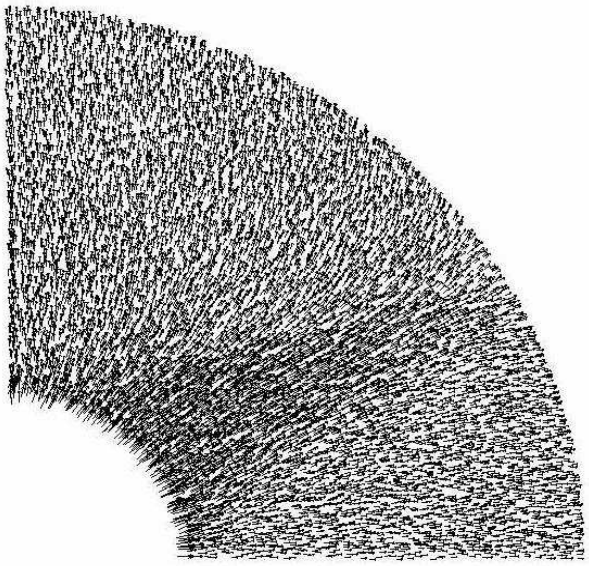

(b)

Figure 5.13: Total displacement after loading for (a) spheres (maximum displacement = 1.088mm), (b) two-ball clumps (maximum displacement = 1.020mm)

Figure 5.14 shows the responses of the sample of spheres and two-ball clumps during the cavity expansion. It can be seen that the clumps sample give a higher cavity pressure than the sample of spheres. The difference in the response of the sample of spheres and two-ball clumps can be attributed to the interlocking provided by the three-dimensional clumps, which affects the rolling resistance and particle displacement. Thus particle shape has a very important influence on the response of the aggregate. As discussed before, particle friction coefficient has a great effect on the maximum cavity pressure, but this did not affect the critical state at large strains (Figure 5.8). However for the clumps, not only does the maximum cavity pressure increase, but the critical or ultimate cavity pressure also increases (Figure 5.14).

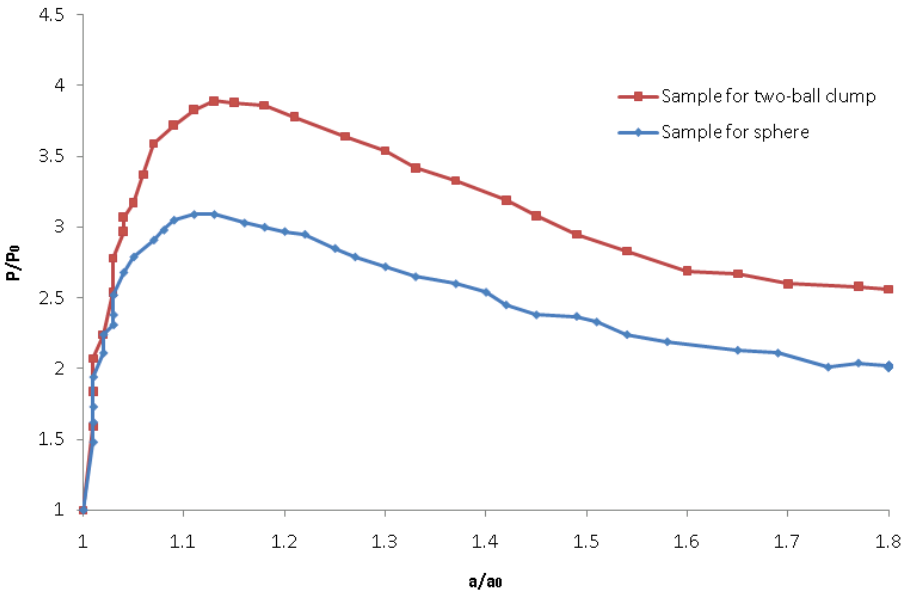

Figure 5.14: Cavity expansion curves for spheres and clumps

5.3.7 Effect of the initial cavity pressure

The in situ state of stress is an important parameter in many areas of geotechnical design. Pressuremeter tests can be used to estimate the in situ

horizontal stress, and thus describe the state of stress in a soil. An experimental study of finite pressuremeter length effects in sand has been developed by Ajalloeian (1996). This experimental study involved a series of calibration chamber tests with four different length to diameter ratios of L/D=5, 10, 15, 20 in a 1m height by 1m diameter calibration chamber. Stress controlled boundaries allowed independent control of vertical and horizontal stresses in the range of 50kPa to 150kPa. The material of Stockton Beach sand was used in these experimental tests. A schematic diagram of the triaxial chamber is shown in Figure 5.15.

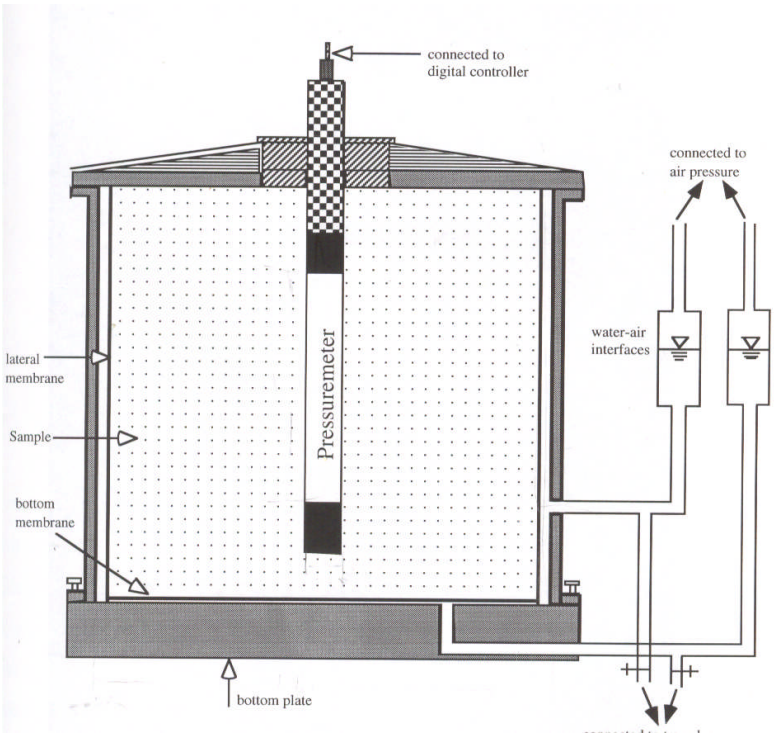

Figure 5.15: Schematic diagram of the calibration chamber (Ajalloeian, 1996)

The length of membrane as a flexible part of the pressuremeter is variable but its diameter is constant (D=30mm). In his research, any soil has two limiting states of density: the loosest and the densest possible states. These states are

influenced by the characteristics of the element grains. The relative density (R_d) is defined as follow (Equation 5.1):

$$R_d = \frac{e_{\max} - e}{e_{\max} - e_{\min}} \tag{5.1}$$

Where $e_{\max}$, $e_{\min}$, e are the void ratios in maximum, minimum and natural states respectively. The influence of specific gravity on the test results is normalised by converting maximum and minimum densities to void ratios. In this research, the samples were prepared by raining pluviation with an average R_d =0.852 for the dense sample, an average R_d =0.639 for the medium dense sample and an average R_d =0.307 for the loose sample. The maximum and minimum dry densities of Stockton Beach sand are 1.77 t/m^3 and 1.49 t/m^3 respectively. The value of G_s is 2.65 and γ_w=9.81kN/m^3 were found for Stockton Beach sand. Equations 5.2 and 5.3 were used to calculate e_{max} and e_{min} as 0.78 and 0.5 respectively.

$$\frac{G_s\gamma_w}{1+e_{\max}} = \gamma_{\max} \Longrightarrow e_{\max} = \frac{G_s\gamma_w}{\gamma_{\max}} - 1 \tag{5.2}$$

$$\frac{G_s\gamma_w}{1+e_{\min}} = \gamma_{\min} \Longrightarrow e_{\min} = \frac{G_s\gamma_w}{\gamma_{\min}} - 1 \tag{5.3}$$

In most analyses, cavity expansion is considered as a plane strain problem, so the walls perpendicular to the length direction have been fixed. Three different initial isotropic states of stress (50, 100 and 150kPa) have been used to perform the simulations with the medium dense sand with R_d =0.67 and L/D=20. From equation 5.1, voids ratio for this sample is e=0.6. Figure 5.16 shows typical

results for tests performed on samples of similar density, subject to a variety of initial cavity pressures (Ajalloeian, 1996). In this figure, the abscissa and longitudinal coordinates are cavity strain (ε_c) and cavity pressure (p') respectively. They can be defined here:

$$p' = \frac{2\sigma_h^{'} + \sigma_v^{'}}{3} \tag{5.4}$$

$$\varepsilon_c = \frac{a - a_0}{a} \tag{5.5}$$

where σ'_h is the effect horizontal stress; σ'_v is the effective vertical stress;

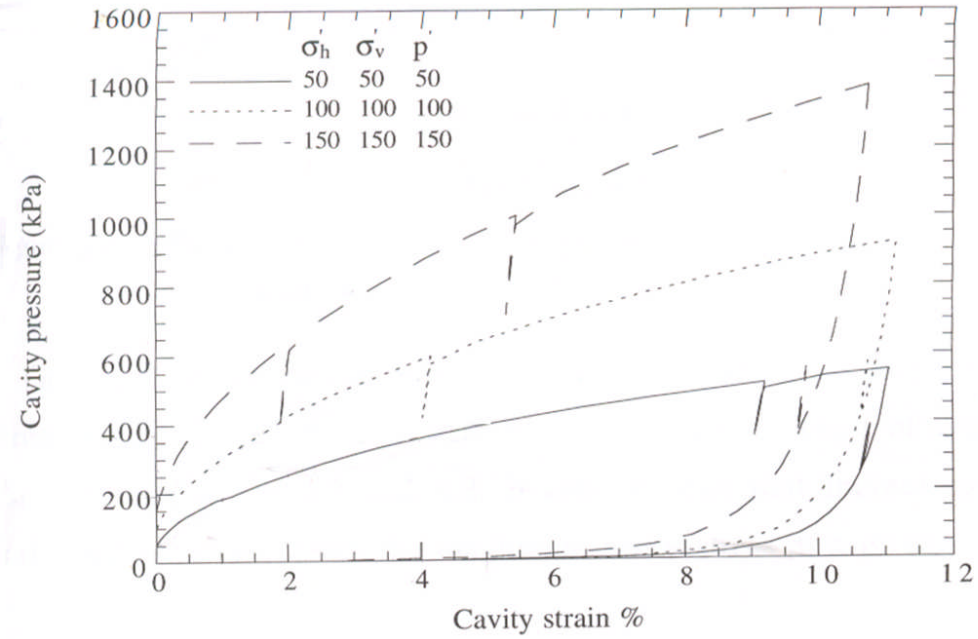

Figure 5.16: Influence of mean effective stress on pressuremeter pressure-expansion curves (medium density sand, L/D=20, K=1) (Ajalloeian, 1996)

Using this information, the simulation of DEM of cavity expansion has been developed. Figure 5.17 shows PFC^{3D} models of the cavity expansion using spherical particles. These particles were used in order to model the particle size

distribution considered by Ajalloeian (1996) shown in Figure 5.18. The DEM simulations are performed to investigate the initial cavity pressure effect on the cavity expansion curves. The particle properties and the sample initial state are given in Table 5.2. Different initial cavity pressures 50kPa, 100kPa and 150kPa were performed on the samples with similar initial geometry (b_0/a_0 is around 10). The purpose of this series of simulations is to investigate the cavity expansion under various stress conditions and compare with the experimental test data.

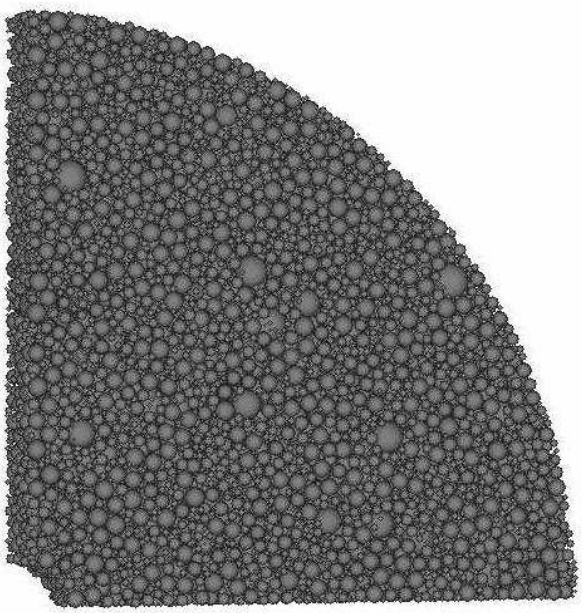

Figure 5.17: PFC^{3D} model with spherical particles

The particle properties		Sample initial state	
Particle stiffness (N/m)	Particle friction coefficient	Initial cavity pressure (KPa)	Initial porosity
1×10^6	0.7	50; 100; 150	0.33

Table 5.2: The particle properties and the sample initial states for simulations in Figure 5.19

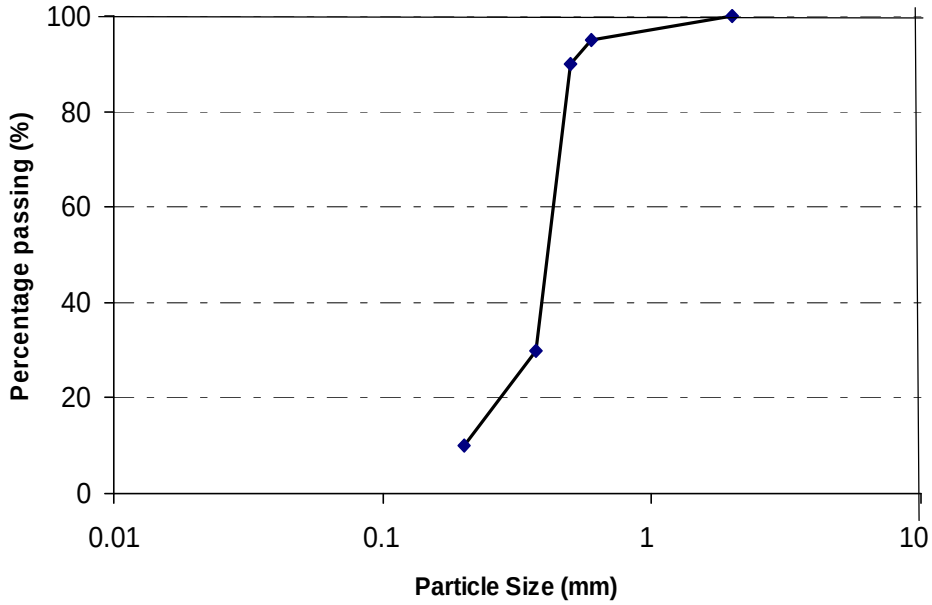

Figure 5.18: Grain size distribution curve for Stockton Beach Sand

The simulation results are shown in Figure 5.19. It can be seen that for soils of a given density, a trend of increasing cavity pressure at a given cavity strain with increasing insitu stresses is clearly observed. It is easy can be obtain that increasing the initial cavity pressure increases the soil resistance. As shown in Figure 5.19, we can get the similar results comparing with the experimental test data, although there are still some differences between the results, especially at larger cavity strains (Figure 5.20).

The difference between the experimental test result and DEM simulation result could be due to the geometry of the sample, initial porosity and the shape of the particles. The geometry used in the simulation (b_0/a_0=10) is smaller than the experimental test. The geometry used in the experimental test (b_0/a_0) is around 33. The initial porosity in the simulation is 0.33, but in the laboratory test is 0.37. The particle shape used in all these simulations is spheres, while the real particle shape used in the experimental test is obviously non-spherical.

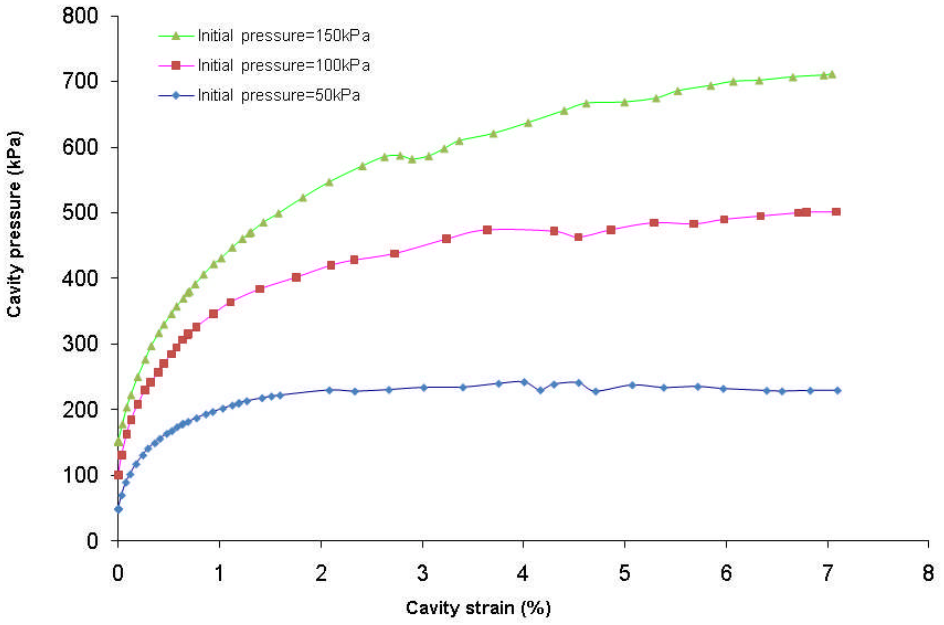

Figure 5.19: Cavity expansion curves using different in-situ stresses in DEM simulations

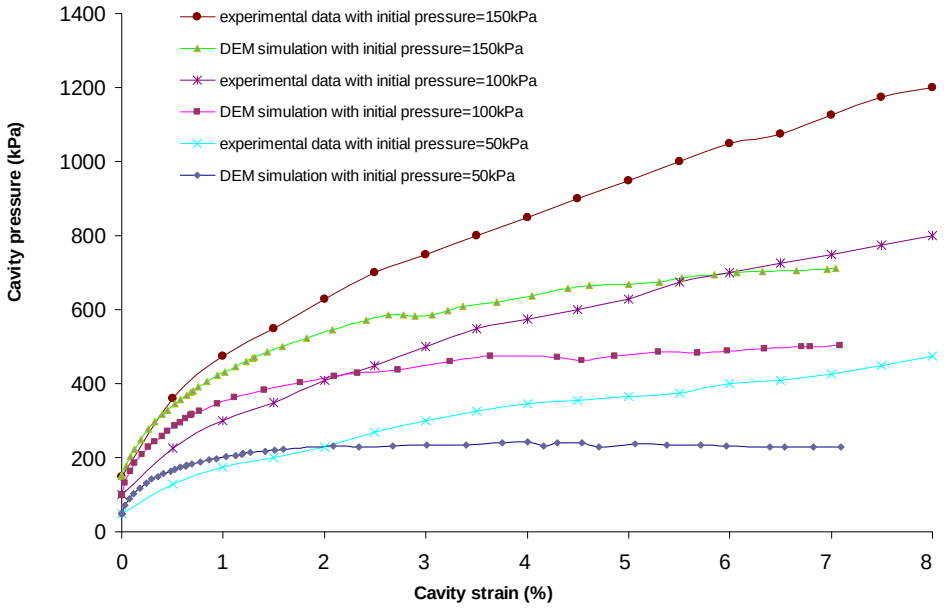

Figure 5.20: Comparison between the experimental test result and DEM simulation result

All these factors contribute to the difference between the results of the DEM simulations and the experimental test results, but the same pattern is discovered. The simulations demonstrate the validity of cavity expansion can be correctly modelled under a range of initial cavity pressures. Qualitative analysis is only discussed here; more simulations with similar conditions to the experimental test are needed for the quantitative analysis.

5.4 Conclusions

PFC^{3D} can be used to simulate soil behaviour under different conditions, and the parameters of the particles hold an important place in the DEM simulation. Selecting the suitable particle parameters is important for DEM simulations. The size of the particle is selected bigger for some simulations to reduce the calculation time since the timestep is related to the particle size. These simulations are just used for comparing with the analytical solutions. The particle properties are selected the same for biaxial simulation and cavity expansion simulation. For comparing with the experiment test result, the particle size is needed to follow with the test material. Only two simple particle shapes are used in these simulations which can not provide the real interlocking of the granular material. These simulations are aim to show the interlocking effect on the granular material behaviour. For simulating the real granular material behaviour, the complicated particle shape similar with the real material is required.

Soil has a very complicated structure, the continuum mechanics is not suit for granular materials like sand under large strain. This chapter showed that DEM can simulate the cavity expansion in granular materials. The particle

parameters and sample initial conditions effect on the sample behaviour of cavity expansion were investigated. Some of these results are used in the following chapter to compare with the analytical solution. More simulations are needed in the future to reveal more realistic behaviour and properties of granular material during cavity expansion.

Further simulations using more realistic particle shapes would shed further light on the micro mechanics of the behaviour in doing cavity expansion.

CHAPTER 6

COMPARISON BETWEEN DEM SIMULATION AND ANALYTICAL SOLUTION

6.1 Introduction

Cavity expansion analysis plays a significant role in modern soil mechanics. Cavity expansion in soil or rock is a fundamental problem in theoretical geomechanics primarily because it provides a useful and simple tool for modelling many complex geotechnical problems. To compare the DEM simulation results with continuum analysis, analytical solutions of large strain expansion of Mohr-Coulomb material are given (Yu, 2000). For simplicity, the soil stress-strain behaviour is considered as elastic-perfectly plastic. Some biaxial test simulations using DEM are performed to obtain the basic granular material properties for obtaining cavity expansion analytical solutions based on continuum mechanics. The particle properties have a significant effect on the soil stress-strain behaviour. The influence of micro-properties of granular material on the macroscopic stress-strain behaviour observed in the DEM simulation was described in chapter 4.

In this chapter, macro properties of samples with various input particle parameters are presented and used to obtain the theoretical cavity expansion

solutions. Cavity expansion analysis focuses on the cavity pressure needed to expand a cavity in soil by a certain amount. The analysis of a cylindrical cavity has been applied to practical problems such as the interpretation of pressuremeter tests (Ladanyi, 1963; Palmer, 1972). A detailed study of the application of cylindrical cavity expansion in modelling the installation of driven piles was given by Randolph and Wroth (1979). The effect of longitudinal shaft friction in a cylindrical expanding cavity has also been considered (Sagaseta, 1984).

DEM modelling is a popular method to numerical simulation for granular soils. To simulate the cylindrical cavity expansion stress-strain curve in a granular material, the cavity expansion simulation using DEM has been discussed in chapter 5. This chapter is mainly focus on the comparison between the analytical solution using cavity expansion method and numerical simulation result using DEM.

6.2 Biaxial Test Simulation

The mechanical response of cohesionless granular materials under monotonic loading is studied using DEM simulations. It describes the effect of initial density and interparticle coefficient of friction on the macro-mechanical behaviour of granular material. Many researchers have shown that DEM successfully simulates the granular material behaviour in the biaxial mode, as observed in experimental tests (Ni, 2003; Huang et al., 2008; Gong, 2008). The DEM simulation of biaxial test has been described in chapter 4.

6.2.1 Sample preparation

PFC^{3D} was used to simulate the biaxial test on samples consisting of spherical particles. A cuboidal sample was generated and loaded by the top and bottom walls. The right and left walls were used to maintain a constant confining pressure. The velocities of the top and bottom walls were specified to simulate the strain controlled loading, the velocities of right and left walls were automatically controlled by a servo-mechanism (see Appendix) to keep the confining pressure constant. The sample modelled in the numerical biaxial test simulations had dimensions of 4m × 1m × 8m in the directions of the minor (y), intermediate (z) and major (x) principal stresses respectively. The properties of all these walls are assumed to be the same. The wall friction coefficient is 0 and wall normal stiffness and shear stiffness are chosen to be the same as particle stiffness 1×10^9 N/m. Around 7000 particles are used to form each sample in these simulations. All the particle parameters are identical. Particle friction coefficient is 0.7 and the particle size distribution for this numerical sample ranged from 0.075 to 0.1m. The specific gravity is 2.65.

6.2.2 Results and discussion

Simulation of a materials macro behaviour using DEM is difficult as the choice of micro-properties is complicated. The particle properties have an important effect on the macro behaviour. Figures 6.1 to 6.3 show the mechanical behaviour of the granular assembly sheared under biaxial condition with samples of different initial porosities. Two samples are generated using

spherical particles and each sample has a different confining stress of 100, 500 and 1000KPa, respectively. Figure 6.1a shows the stress-strain curves of a dense sample, with initial porosity n=0.36, where axial strain ε_a is the strain along the x direction. It shows a peak stress at a relatively low strain and thereafter the stress necessary for additional strain decreases. The stress-strain behaviour of a loose sample, with n=0.42, are presented in Figure 6.1b showing that the principal stress ratio increases gradually to an ultimate value without a prior peak.

Figure 6.2 and Figure 6.3 show the stress-strain behaviour and dilation of samples with confining pressure of 1000KPa and initial porosity of 0.36 and 0.42. The term dilatancy is used to describe the increase in volume of a dense sand during shearing and the rate of dilation can be represented by the gradient $d\varepsilon_v/d\varepsilon_a$. Figure 6.2 shows the counterpart of Figure 6.1 under drained condition, with the sample having different initial porosities after being compressed to 1000KPa istropically. It can be seen from Figure 6.2 that the loose sample exhibits a hardening behaviour, while the dense sample tends to show strain-softening after reaching their peak states. However, an essentially identical critical state is finally approached when the samples are subjected to large deformations. The critical axial stress is around 2100KPa. The maximum angle of friction (φ) is determined from peak stresses.

The results in Figure 6.3 show an increase in the volume of the specimen during shearing for a dense sand, as characterized by the relationship between volumetric strain and axial strain. The volumetric strain is defined as the change of volume per unit of volume. The peak strength normally corresponds

to the maximum rate of dilation. A parameter known as the angle of dilation (ψ) is defined either in terms of the maximum and minimum principal strain increments $d\varepsilon_1$ and $d\varepsilon_3$ or in terms of increments of volumetric strain ($d\varepsilon_v$) and maximum shear strain ($d\gamma$). In the case of a loose sand the increase in stress is accompanied by a decrease in volume, as shown in Figure 6.3. The particle parameters and the initial states of each sample are given in Table 6.1. This information needs to be used in the cavity expansion simulations, which will be described later.

The initial porosity was calculated using measurement spheres, which is a function available in PFC^{3D}. The porosity of all measurement spheres is shown in Figure 6.4. The bottom plane is used to indicate the position of each measurement sphere located at X-Y plane of sample in biaxial test simulation and the vertical axle is used to present the porosity of each sphere. We can see that the porosities are quite uniform. The finial initial porosity is the average value of these porosities.

The particle properties		Sample initial state	
Particle stiffness (N/m)	Particle friction coefficient	Confining pressure (KPa)	Initial porosity
1×10^9	0.7	100; 500; 1000	0.36, 0.42

Table 6.1: The particle properties and the sample initial states of biaxial test simulation

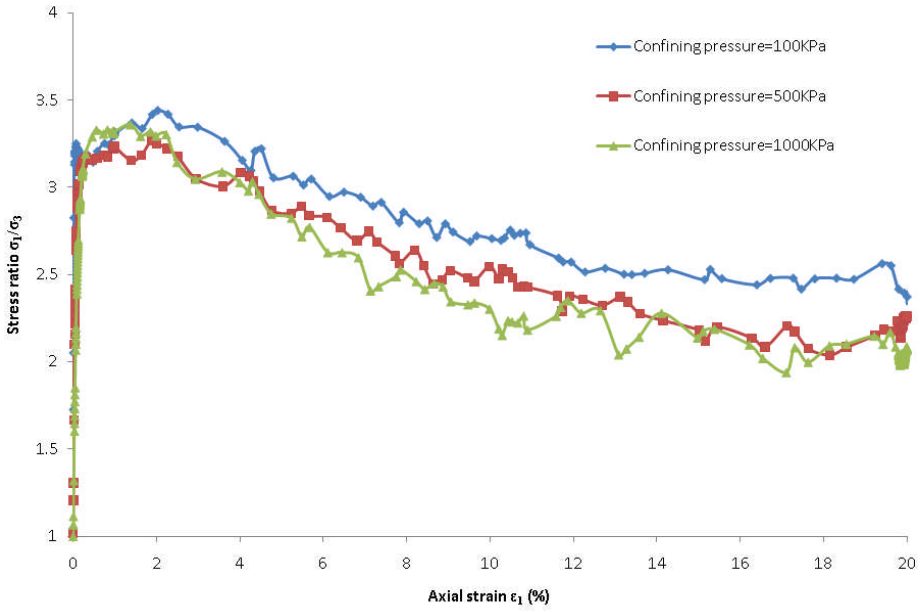

(a) Initial porosity=0.36

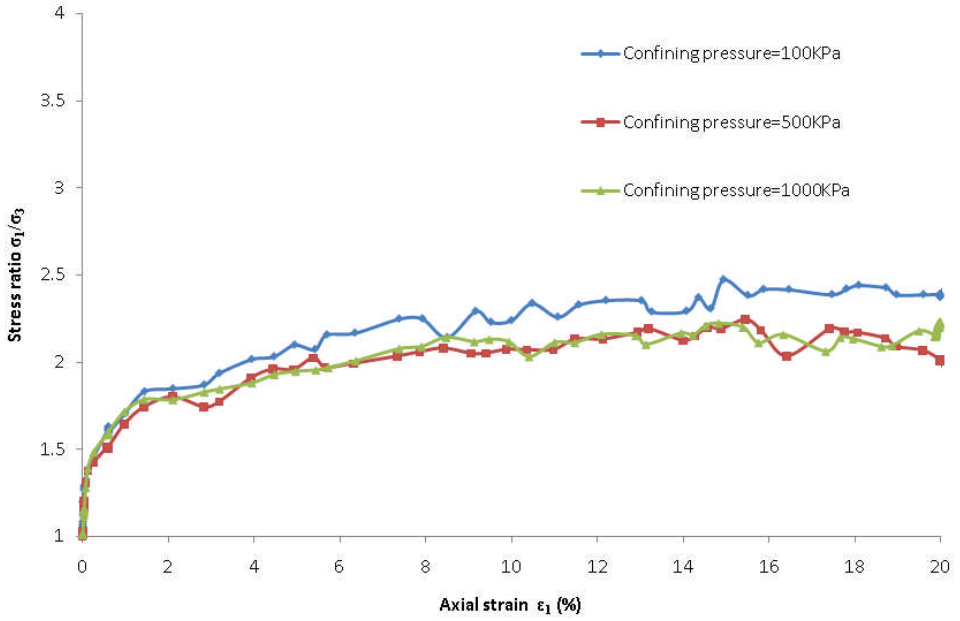

(b) Initial porosity=0.42

Figure 6.1: Stress-strain behaviour of cell pressure 100, 500, 1000kPa using DEM

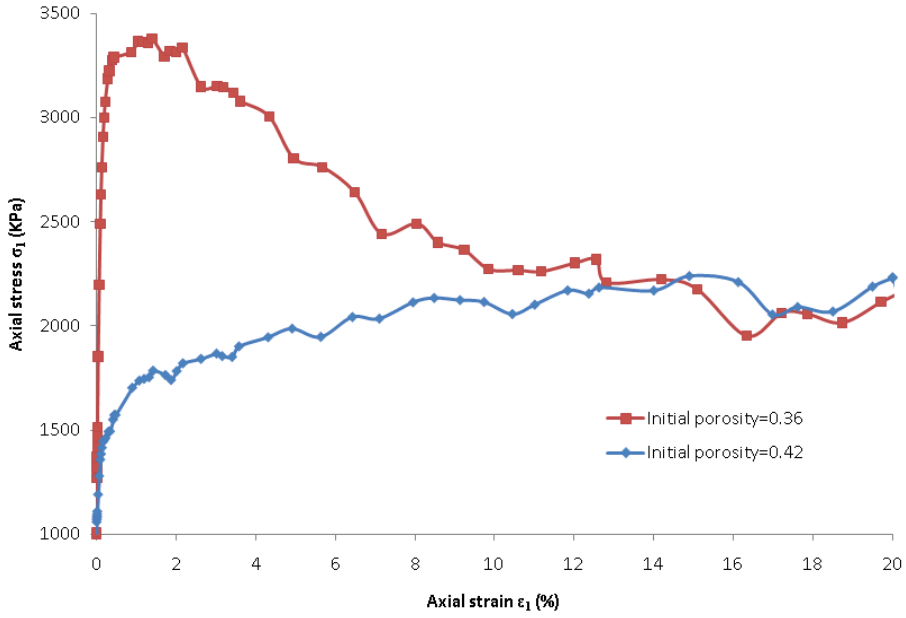

Figure 6.2: Stress-strain behaviour of DEM simulations (Cell pressure=1000kPa)

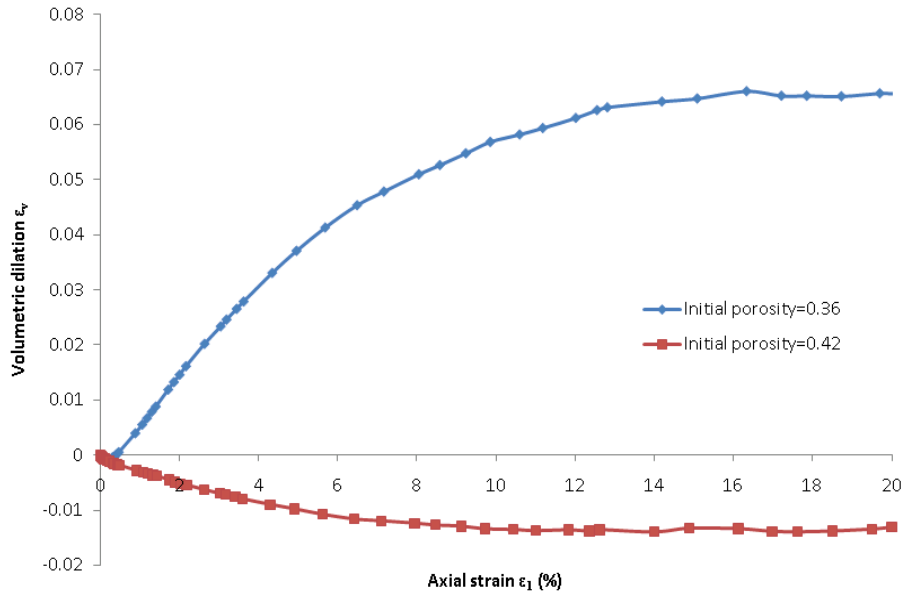

Figure 6.3: Volumetric dilation against axial strain of DEM simulations (Cell pressure=1000kPa)

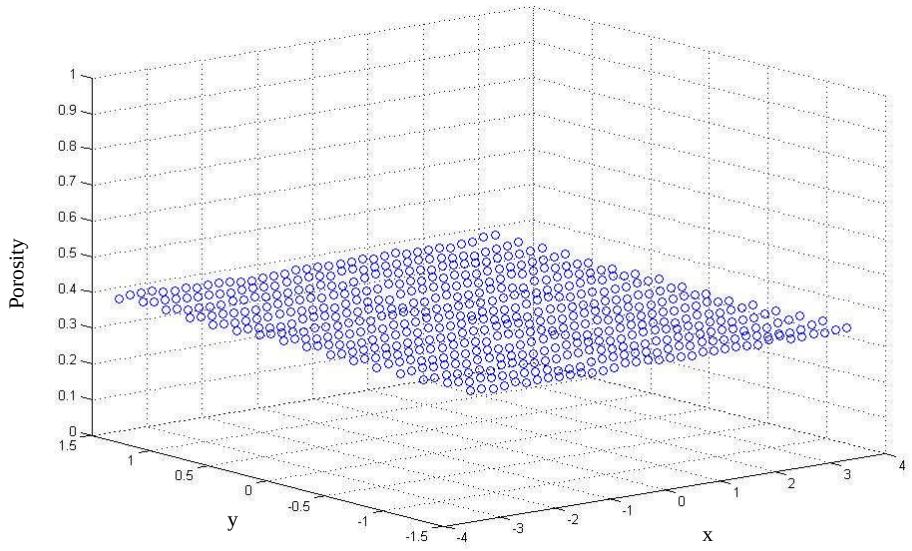

Figure 6.4: The initial porosities of biaxial test simulation

This chapter presents mainly on the comparison between the analytical solution and DEM simulation results of cavity expansion. It is clear that the material properties are important for getting the analytical solution, so these biaxial tests simulations using DEM are performed to evaluate the material properties from the particle-scale view. The same particle parameters are applied in both the biaxial test simulations and cavity expansion simulations, and the soil parameters which are used in the theoretical analytical solution of cavity expansion are calculated from the biaxial test simulation results. In addition, the same initial conditions are required for these two kinds of simulations. For the cylindrical cavity expansion simulation, z direction is fixed for simulating the plane-strain problem. So z direction is fixed as well in the biaxial test simulations for the relative same initial conditions. These biaxial test simulations are like a ligament that connects the analytical solution and the

DEM solution of cavity expansion.

6.3 Cavity Expansion Simulation

Cavity expansion processes are relevant to a number of problems of interest in soil mechanics, including pressuremeter testing, pile driving, pile loading to failure, cone penetration testing, and detonation of explosive devices within soil deposits. Many researchers focused on this problem. The boundary condition problems like bearing cavity of granular ground have been studied by Ting et al. (1989). Huang and Ma (1994) were the first to use DEM in deep penetration simulations in sand. Later, the study on soil-penetrometer interface friction has been described by Jiang et al. (2006). A two-dimensional discrete element method has been used to simulate the deep penetration tests on a granular ground. The DEM simulation of cavity expansion has been presented in chapter 5.

6.3.1 Sample preparation

The DEM code PFC^{3D} was used to simulate cylindrical cavity expansion on samples consisting of spheres or clumps (Figure 6.5).A quarter of a fan-shaped sample was generated and loaded by its internal boundary using a constant strain rate. The velocity of its external boundary was automatically controlled by a servo-mechanism (see Appendix) to keep a constant external pressure. The sample thickness was fixed by front and back walls to simulate the plane-strain condition. Two other walls normal to x and y axes are fixed since it is an axial symmetry of the x and y axes structure. Stresses on the walls are determined from the particles contact forces acting on them. The particle parameters are

exactly the same with the biaxial test simulations. For the sample consisting of spherical particles, all the particle parameters and sample initial states are shown in table 6.2. The minimum particle radius for each sample was 0.075m and maximum radius was 0.1m. The particle friction coefficient is 0.7 and the normal stiffness and shear stiffness of particles are 1×10^9N/m. Six walls were generated as sample boundaries. The wall friction coefficient is 0 and wall normal stiffness and shear stiffness are 1×10^9 N/m. Around 7000 Particles were generated to fill into this space for each sample.

Two different initial cavity pressures were used. One was 20MPa. The other was 1MPa. For the higher initial cavity pressure $P_i=P_e=P_0=20$MPa, four samples are generated with different initial porosities (0.36, 0.38, 0.40 and 0.42) which have been described in chapter 5. The initial porosities are calculated by a measurement sphere which is a function available in PFC^{3D}. Using the measurement spheres, the porosity of each sphere can be obtained. Many spheres are generated to cover the whole sample. The finial porosity is decided by using the average value of these porosities (Figure 6.6). As shown in Figure 6.6, X-Y plane is used to show the position of each sphere and the z axle is used to indicate the porosity of each measurement sphere. The various initial porosities of these samples can result from the different particle friction coefficients during the generation of each sample. Once the initial state of the sample is reached, the particle friction coefficient is changed to the same value 0.7. While for the lower initial cavity pressure $P_i=P_e=P_0=1$MPa, another two samples are generated with initial porosities n=0.36 and 0.42. The samples generation and the initial porosity calculation are the same with the samples of higher initial cavity pressure.

For investigating the result of sample consisting of different particle shape, anther sample using two-ball clumps (Figure 6.5(b)) was generated with initial porosity n=0.36. The initial cavity pressure was 20MPa and the particle parameters are the same with the spherical particle described in Table 6.2.

The particle properties		Sample initial state	
Particle stiffness (N/m)	Particle friction coefficient	Confining pressure (MPa)	Initial porosity
1×10^9	0.7	1; 20	0.36, 0.42

Table 6.2: The particle properties and the sample initial states of cavity expansion simulation

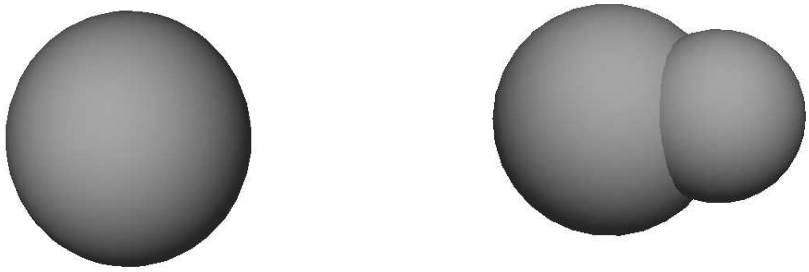

(a) **(b)**

Figure 6.5: PFC^{3D} model (a) single sphere as a particle; (b) two-ball clump as a particle

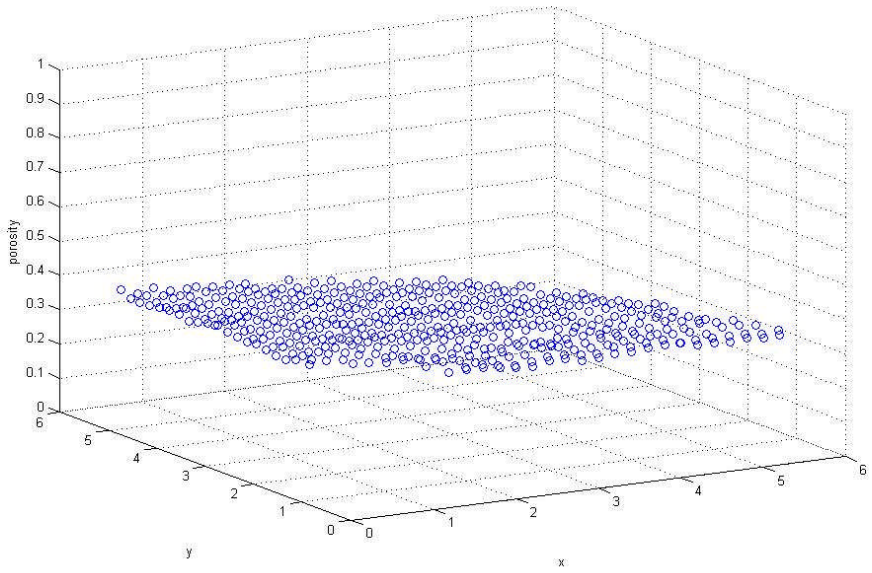

Figure 6.6: The initial porosities of cavity expansion simulation

6.3.2 Results and discussion

6.3.2.1 Cylindrical cavity expansion curves of DEM simulation

PFC^{3D} can be used to simulate the soil behaviour under different conditions. The parameters of the particles hold an important place in DEM simulation. The selection of particle parameters has significant influences on the sample behaviours. Figure 6.7 shows the results of two simulations selected from Figure 5.6 in chapter 5. The initial cavity pressure for these samples is 20MPa and b_0/a_0 is around 6. It can be seen from Figure 6.7 that the peak cavity pressure ratio (P/P_0) varied from 3.1 for the dense sample to 2.2 for the loose. The corresponding range of internal radius (a/a_0) at peak pressure was 1.13 (dense) to 1.28 (loose). The final cavity pressure ratio, at 1.7 internal radius, was about 2 in these cases. The results of another two simulations (Initial

porosity n=0.36 and 0.42) of initial cavity pressure P_0=1MPa have been shown in Figure 6.8. It is apparent that the result obtained from lower initial cavity pressure is in accordance with the result of higher initial cavity pressure shown in Figure 6.7. Meanwhile, it is found that the maximum cavity pressures increase significantly while the value of initial porosities decreases.

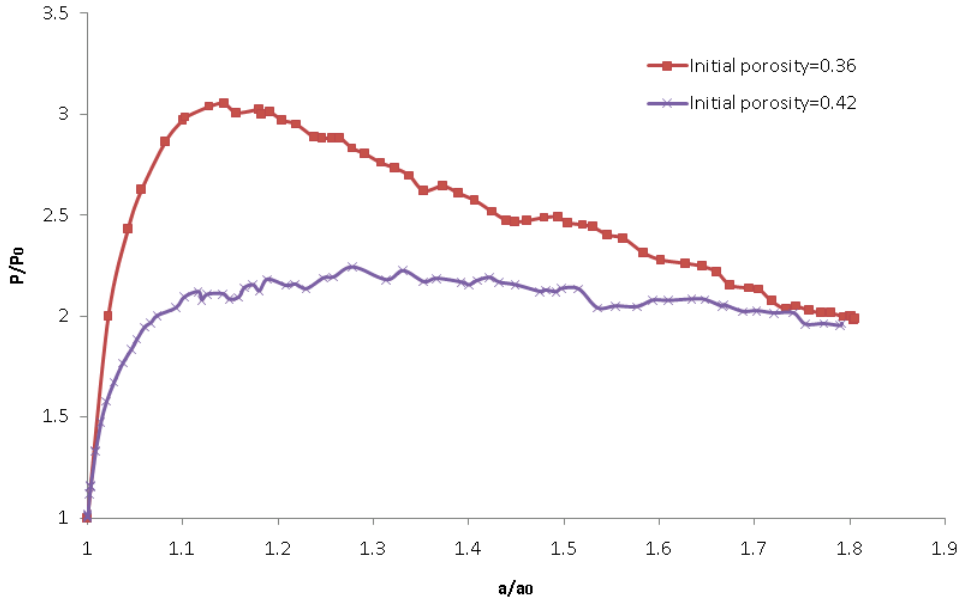

Figure 6.7: The cavity expansion curves of different initial porosities using DEM simulations (Initial cavity pressure=20MPa)

Figure 6.9 shows the typical results of cavity expansion simulations performed on samples of similar initial porosities (0.36 and 0.42), subject to a variety of initial cavity pressures. It can be seen that for soils of a given porosity, a trend of increasing the value of cavity pressure ratio with decreasing the initial cavity pressure is clearly observed. The results of initial porosity 0.36 are graphically presented in Figure 6.9 (a) for initial cavity pressures of 1MPa and 20MPa. As

can be expected, the curve of small initial cavity pressure tends to give the maximum cavity pressure at smaller internal radius ratio (a/a_0).

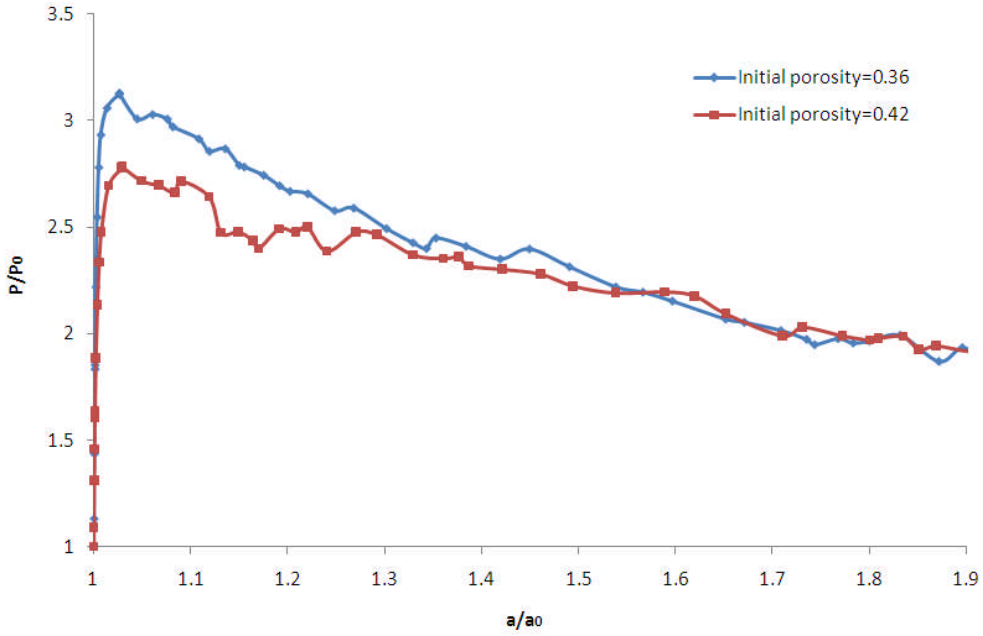

Figure 6.8: The cavity expansion curves of different initial porosities using DEM simulations (Initial cavity pressure=1MPa)

In other words, this happens when the deformation required to reach the maximum cavity pressure is smaller than the one of higher initial cavity pressure. This is because the different initial cavity pressures are used for these simulations of similar initial porosity. As the state of a material depends not only on its density (void ratio e) but also on P (confining pressure). For the different P, different e_c (the preordained void ratio at a critical state) can be obtained. So the soil behaviour could be different for the same current void ratio but different P.

As shown in Figure 6.9 (b), the initial porosity is 0.42, the value of the cavity

pressure increases during the loading and the maximum cavity pressure occurs at increasingly large value of internal radius ratio when the initial cavity pressure is 20MPa. No prior peak value of cavity pressure is shown. While for the sample of initial cavity pressure of 1MPa, the soils must be relative denser than that of initial cavity pressure 20MPa when the similar initial porosity 0.42 is considered. The result in Figure 6.9 (b) showing that a softening curve is observed with the initial cavity pressure 1MPa and the value of cavity strain required to reach the maximum cavity pressure is also relative smaller. The peak cavity pressure is reached at very small internal radius ratio (a/a_0=1.03).

It is interesting to compare these simulation results with the analytical cavity expansion solutions obtained from Yu (1992, 2000). The cavity expansion theory is applied to obtain the analytical solution of cavity expansion using soil properties which is described in the following part. These soil properties are obtained from the biaxial test simulations results. So the particle parameters and sample initial states of cavity expansion simulations are selected the same with the biaxial test simulations to make sure that these results of comparison comes from the same soil particles. Some biaxial test simulation results have been discussed in the beginning, as shown in Figure 6.1. The results shown in Figure 6.7 and 6.8 which have the same initial state with the samples in these biaxial test simulations are used to compare with the theoretical analytical solutions. For the sample consisting of two-ball clumps, the result shown in Figure 6.10 is going to compare with the analytical solution too. In order to obtain this analytical solution, some biaxial test simulations using the same particle properties and initial states with the cavity expansion simulations for two-ball clumps are needed.

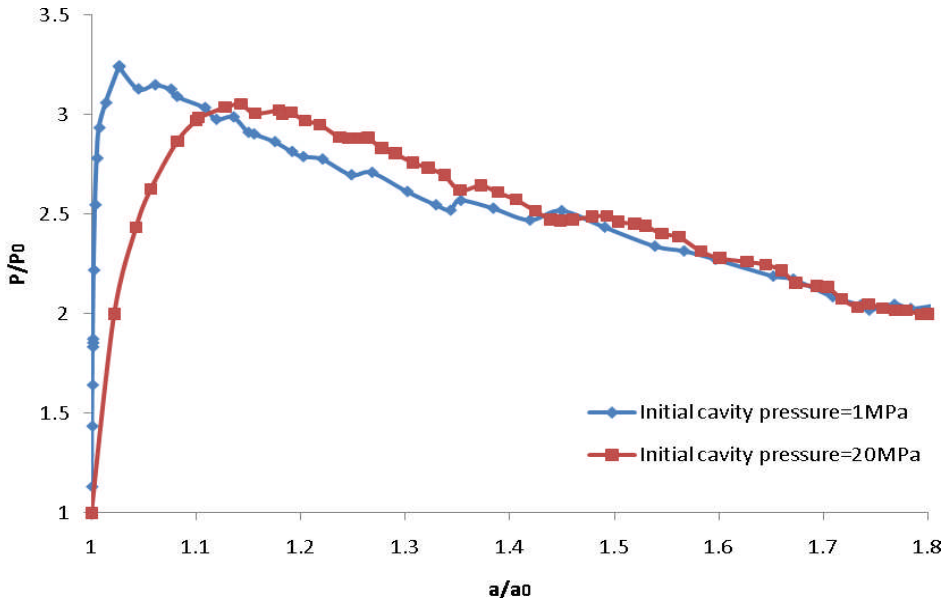

(a) Initial porosity=0.36

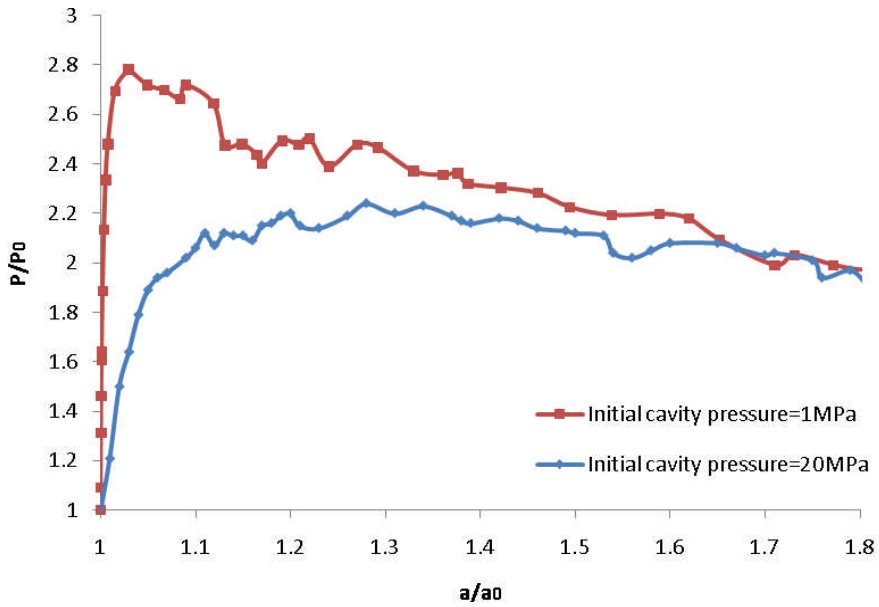

(b) Initial porosity=0.42

Figure 6.9: The cavity expansion curves of different initial cavity pressures for samples of different initial porosities in DEM simulations

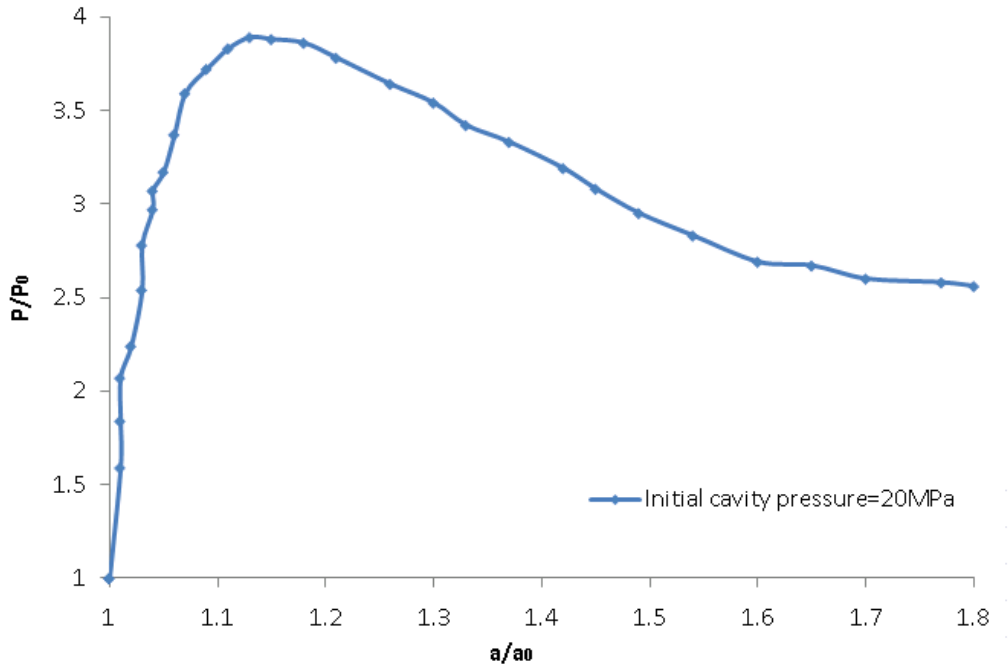

Figure 6.10: The cavity expansion curve of sample consisting of two-ball clumps and initial porosity n=0.36 in DEM simulations

6.3.2.2 The analytical solutions of cylindrical cavity expansion

The cylindrical cavity expansion stress-strain curve of idealized material can be obtained using the cavity expansion method (Yu, 1992, 2000). The material is modelled as an isotropic dilatant elastic-perfectly plastic material. The elastic behaviour obeys Hooke's law until the onset of yielding which is determined by the Mohr-Coulomb criterion. The theoretical cylindrical cavity expansion curve is described by the material properties (Young's modulus E, Poisson's ratio ν, cohesion c, angle of friction φ and angle of dilation ψ). A non-associated plastic flow rule is used and therefore the dilatancy of the soil is fully taken into account. In order to obtain the proper material properties for analytical solutions, DEM simulations of biaxial tests were carried out as described before. This biaxial test simulation acts as ligament to connect the analytical solution using macroscale material properties and the DEM solution

using microsacle particle properties. The analytical solution can be presented for stress and displacement field for the cylindrical cavity expansion.

6.3.2.2.1 Soil properties

The properties of the soil are defined by the Young's modulus E, Poisson's ratio ν, cohesion c, angle of friction φ and angle of dilation ψ. The initial in-situ stress is $P_{0.}$ Some derived parameters which are constant can be abbreviated in the mathematics.

$$G = \frac{E}{2(1+\nu)} \tag{6.1}$$

$$M = \frac{E}{1-\nu^2} \tag{6.2}$$

$$Y = \frac{2C\cos\phi}{1-\sin\phi} \tag{6.3}$$

$$\alpha = \frac{1+\sin\phi}{1-\sin\phi} \tag{6.4}$$

$$\beta = \frac{1+\sin\varphi}{1-\sin\varphi} \tag{6.5}$$

$$\gamma = \frac{\alpha(\beta+1)}{(\alpha-1)\beta} \tag{6.6}$$

$$\delta = \frac{Y+(\alpha-1)p_0}{2(1+\alpha)G} \tag{6.7}$$

Initially the radii of inner and outer boundaries of the cylinder are a_0, b_0 respectively and a hydrostatic pressure p_0 acts throughout the soil which is assumed to be homogeneous. An additional pressure $p\text{-}p_0$ is then applied inside the cavity and increased sufficiently slowly for dynamic effects to be negligible. If the principal stress components satisfy the inequalities $\sigma_i \le \sigma_j \le \sigma_k$, the Mohr-Coulomb yield function takes the form $\alpha\sigma_k - \sigma_i = Y$. Tensile stress and strain are considered as positive.

At any time in any position around the cavity, the inner and outer radii a_0 and b_0 change to a and b and the stress must satisfy the equation of equilibrium:

$$(\sigma_\theta - \sigma_r) = r\frac{\partial \sigma_r}{\partial r} \tag{6.8}$$

Subject to the two boundary conditions:

$$\sigma_r\big|_{r=a} = -p \tag{6.9}$$

$$\sigma_r\big|_{r=b} = -p_0 \tag{6.10}$$

The displacement is defined as $u = r - r_0$

6.3.2.2.2 Elastic response and Elastic-plastic stress analysis

The deformation of the soil at first is purely elastic with the cavity pressure increases from p_0. The elastic stress-strain relationship can be expressed as:

$$\dot{\varepsilon}_r = \frac{\partial \dot{u}}{\partial r} = \frac{1-\nu^2}{E}\left[\dot{\sigma}_r - \frac{\nu}{1-\nu}\dot{\sigma}_\theta\right] \tag{6.11}$$

$$\dot{\varepsilon}_\theta = \frac{\dot{u}}{r} = \frac{1-\nu^2}{E}\left[-\frac{\nu}{1-\nu}\dot{\sigma}_r + \dot{\sigma}_\theta\right] \tag{6.12}$$

The solution of equations (6.11), (6.12) and (6.8) subject to the boundary conditions (6.9) and (6.10) is given in chapter 2 (elastic-perfectly plastic solutions).

When the internal pressure reaches p_{1y} (Equation 2.16), the material starts to yield from the internal surface. After initial yielding at the cavity wall, a plastic region forms around the inner wall and the cavity wall which increased with the cavity pressure.

The radius of elastic-plastic boundary, the internal pressure (When c=b, the whole cylinder becomes plastic), the outer boundary displacement in the elastic zone and the value of c/a and a/a_0 can be obtained using equations shown in chapter 2. These equations in chapter 2 aimed to express the pressure and expansion relationship depends on the different conditions.

6.3.2.2.3 The procedure

To obtain the cylindrical cavity expansion analytical solutions, decide the soil properties first. Choose the suitable soil properties parameters, like E, v, C, Φ, Ψ and then decide the initial pressure p_0 and the internal and external radius a_0 b_0. Secondly, calculate the derived parameters: G, Y, α, β, γ, δ using equations 6.1-6.7. Calculate the yielding pressure p_{1y} from equation 2.16 in chapter 2. If the internal pressure p is less than this yielding pressure, then calculate the

expansion radius from elastic solution in chapter 2. If the pressure is larger than this yielding pressure, then calculate the radius from the elastic-plastic solutions shown in chapter 2 as well. When c=b, the whole cylinder becomes plastic, the pressure at that conditions also can be calculated (as shown in chapter 2).

6.3.2.2.4 Discussion of the results

In this chapter, some basic cavity expansion solutions for elastic-perfectly plastic soils are described. To obtain the cylindrical cavity expansion analytical solution using soil properties, the soil is modelled as an isotropic dilatant elastic-perfectly plastic material obeying the Mohr-Coulomb criterion as described before. It is very difficult to fit the complete real stress-strain behaviour of sandy soil satisfactorily with a simple elastic-perfectly plastic model. The upper bound and lower bound are used to explain the soil behaviour. Real stress-strain behaviour is between them. For the sample of spherical particles, the upper bound and lower bound are chosen as elastic-perfectly plastic model based on the biaxial test simulation results in Figure 6.1. These models are formed by two straight lines shown in Figure 6.11. The upper bound is formed using initial stiffness and peak axial stress value. The lower bound is mainly formed by critical axial stress. When the horizontal straight line cross the critical axial stress, it is easy to find another point through the stress-strain curve on this line. Connect this point with the origin of coordinates to form another straight line for lower bound. The sample of initial porosity n=0.42 is quite loose and no prior peak axial stress is obtained. Therefore only one elastic-perfectly plastic model is used for this sample (see Figure 6.12).

This model is composed by initial stiffness and ultimate axial stress value. For the sample of non-spherical particles, some biaxial test simulations of sample consisting of two-ball clumps with initial porosity n=0.36 were carried out to calculate the soil properties. Figure 6.13 shows the generated upper bound and lower bound for this sample using the same method as the sample of spherical particles.

The soil properties can be obtained from these selected upper bound and lower bound models based on the biaxial test simulation results. The ultimate/maximum friction angle and cohesion are obtained from Mohr-Coulomb criterion. The other macroscale parameters of the material are obtained from these equations:

$$\text{Young's modulus: } E = \frac{\delta\sigma_X}{\delta\varepsilon_X} \tag{6.13}$$

$$\text{Poisson's ratio: } \nu = -\frac{\delta\varepsilon_y}{\delta\varepsilon_x} \tag{6.14}$$

$$\text{Dilation angle: } \sin\psi_{\max} = \frac{\delta\varepsilon_1 + \delta\varepsilon_3}{\delta\varepsilon_1 - \delta\varepsilon_3} \tag{6.15}$$

In accordance with these equations and the Mohr-Coulomb criterion, the material properties of each model can be calculated, as shown in table 6.3. From biaxial test simulations results, the material behaviours are represented by five elastic perfectly plastic models to calculate these material properties.

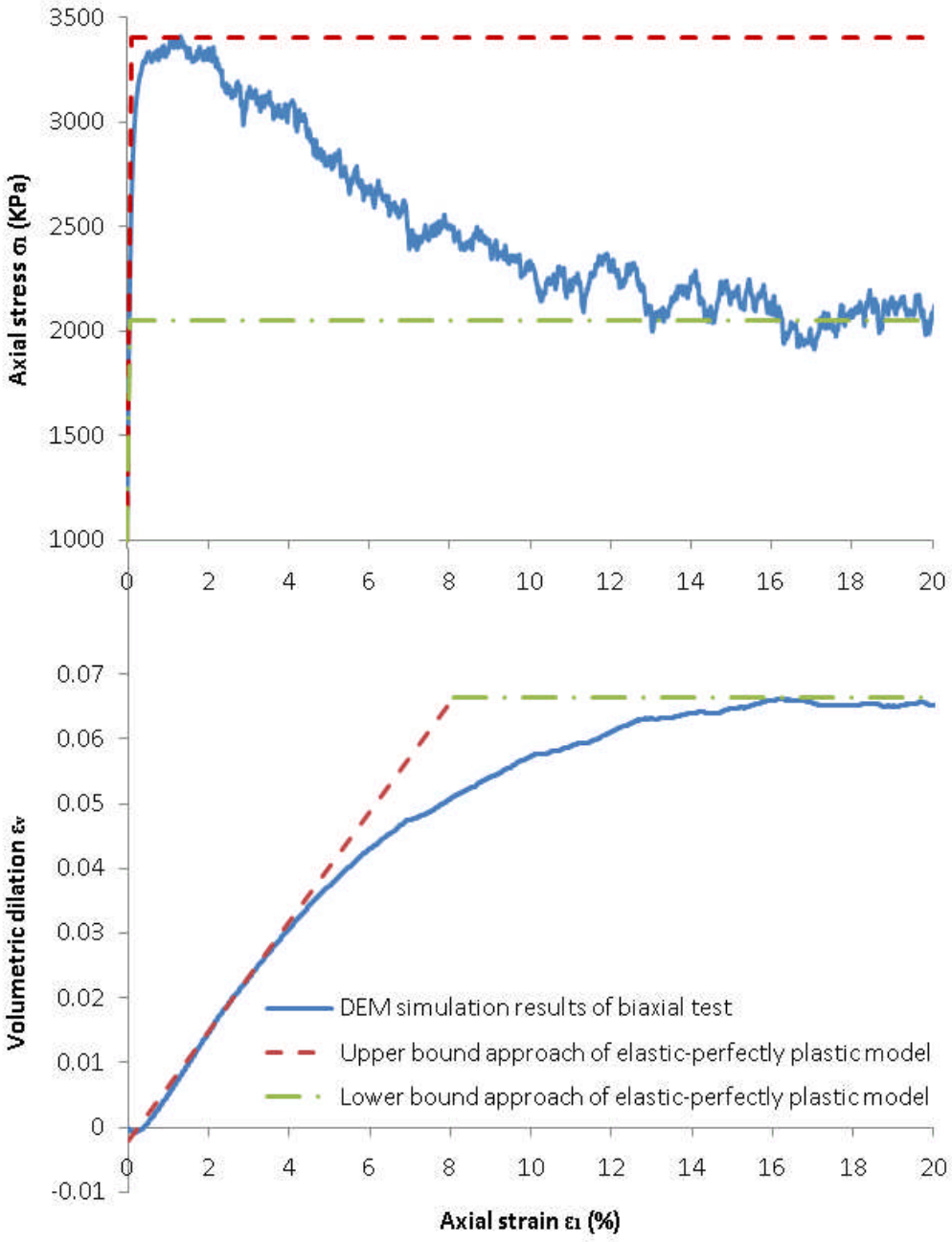

Figure 6.11: The choosing upper bound and lower bound for sample initial porosity 0.36 in DEM simulation

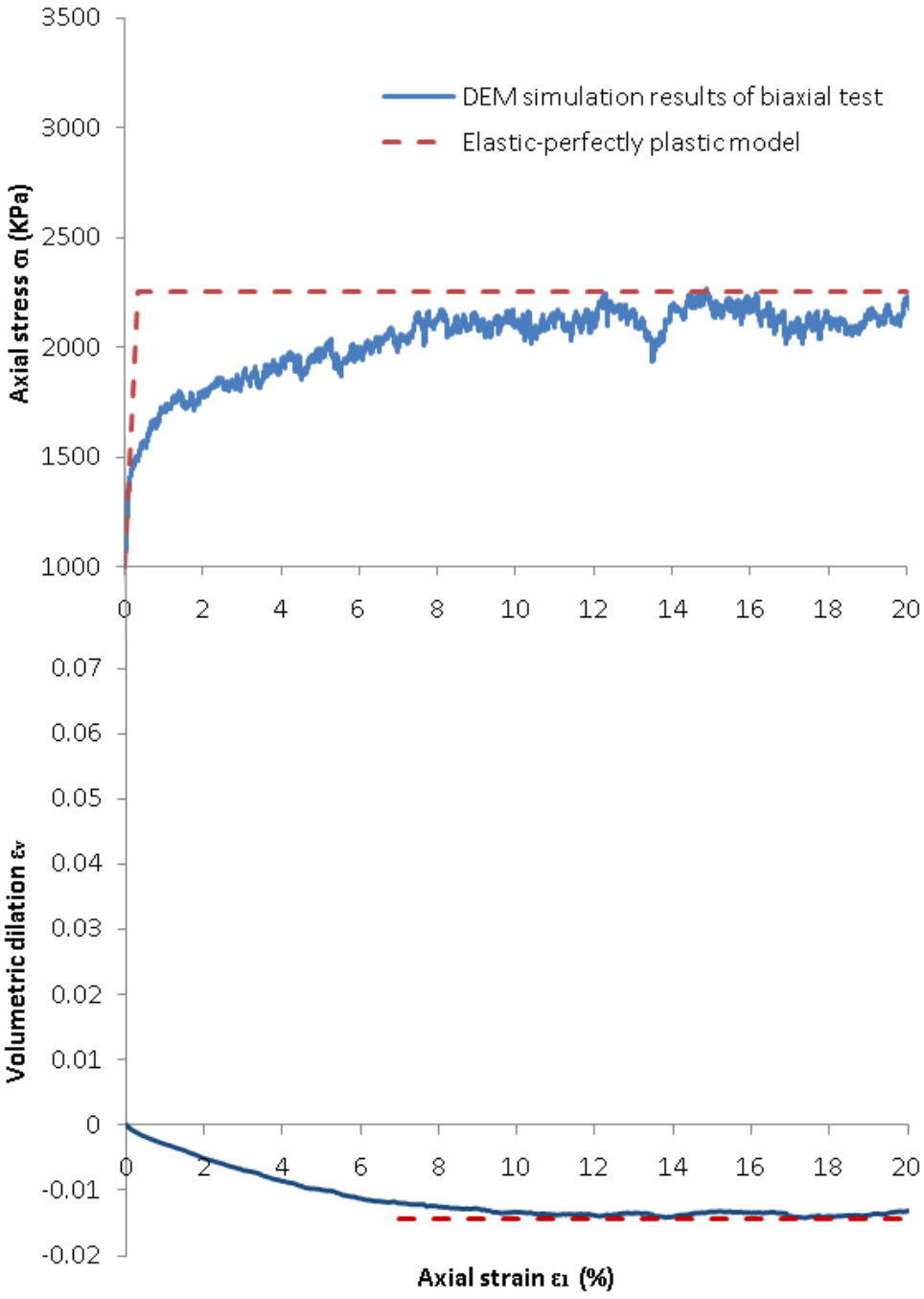

Figure 6.12: The choosing upper bound and lower bound for sample initial porosity 0.42 in DEM simulation

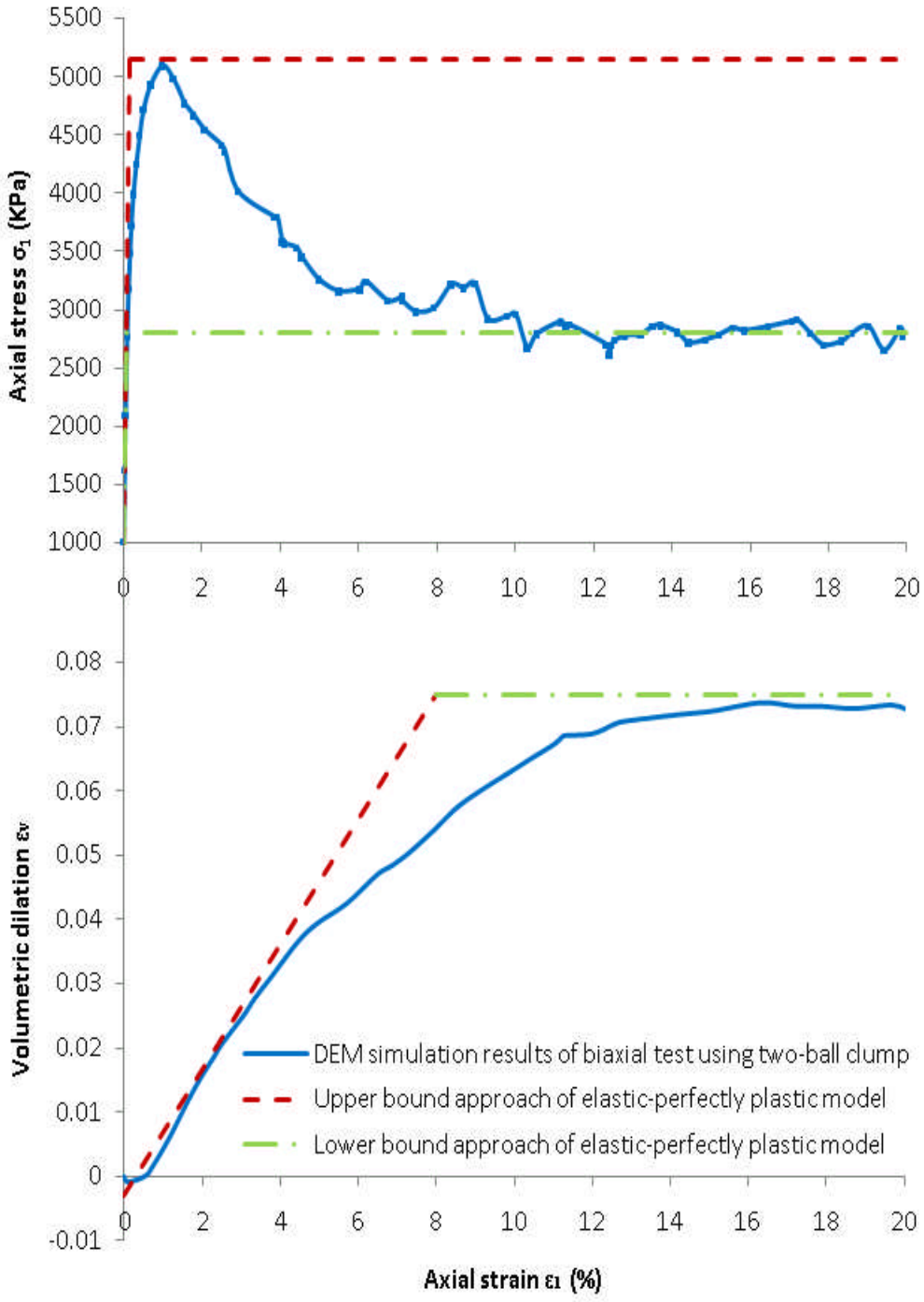

Figure 6.13: The choosing upper bound and lower bound for sample of two-ball clumps (Initial porosity n=0.36) in DEM simulation

Upper bound approach and lower bound approach are shown in Figure 6.11 and Figure 6.13 and elastic-perfectly plastic model is shown in Figure 6.12. As we can see from Figure 6.11 and Figure 6.13, the upper bound is based on the maximum axial stress. The maximum rate of dilation is occurred when the peak axial stress is reached. It can explain that the maximum friction angle and maximum dilation angle can be obtained using upper bound approach. While the lower bound is formed by critical axial stress. It can be used to calculate the critical friction angle and critical dilation angle. The value of slope of curves in Figure 6.11 and Figure 6.13 (Volumetric dilation against axial strain) becomes more and more small and the value is almost zero when the critical state is reached. That means the dilation angle is zero and the minimum friction angle can be obtained when the lower bound is used in the calculation. Plotted in Figure 6.12 shows that just one elastic-perfectly plastic model is generated to explain the soil behaviour, so the friction angle calculated using this model is both maximum and critical friction angle. The dilation angle is zero since the maximum axial stress equal to the critical axial stress in this case. These parameters are very useful for the analytical solutions of cavity expansion using the cavity expansion method. The theoretical results of cylindrical cavity expansion can be obtained using these calculated soil parameters and the boundary values of cavity expansion from the large strain analysis. In the large strain analysis the cylinder thickness is continuously reduced as the elastic-plastic boundary spreads out. The results are graphically illustrated in Figure 6.14 for sample initial porosity of 0.36 and 0.42 and initial cavity pressure of 20MPa. The results in Figure 6.14 (a) show that a softening curve is observed for the sample initial porosity n=0.36, but not for another sample initial

porosity n=0.42. Plotted in Figure 6.15 is the cavity expansion curves with sample initial porosity of 0.36, 0.42 again, but the initial cavity pressure is 1MPa. Softening behaviour can be observed for both of them shown in Figure 6.15. Figure 6.16 shows the cavity expansion curves obtained using cavity expansion method for the sample initial porosity of 0.36 and particle of two-ball clumps with the initial cavity pressure of 20MPa. The same result can be observed as shown in Figure 6.14 and Figure 6.15. The maximum cavity pressure is normally reached before the whole cylinder becomes plastic.

Model	Initial porosity	E (MPa)	v	φ (D)	ψ (D)	c (MPa)	b_0/a_0	P_0 (MPa)
U-D-S	0.36	2400	0.3	33	14	0	6.20/1.15	1, 20
L-D-S	0.36	1615	0.3	21	0	0	6.20/1.15	1, 20
E-L-S	0.42	568	0.3	22	0	0	6.41/1.02	1, 20
U-C	0.36	2310	0.3	42	16	0	6.33/1.07	20
L-C	0.36	1800	0.3	28	0	0	6.33/1.07	20

U-D-S: Upper bound approach of elastic-perfectly plastic model for sample consisting of spherical particles (relative dense sample with initial porosity=0.36)

L-D-S: Lower bound approach of elastic-perfectly plastic model for sample consisting of spherical particles (relative dense sample with initial porosity=0.36)

E-L-S: Elastic-perfectly plastic model for sample consisting of spherical particles (relative loose sample with initial porosity=0.42)

U-C: Upper bound approach of elastic-perfectly plastic model for sample consisting of two-ball clumps (initial porosity=0.36)

L-C: Lower bound approach of elastic-perfectly plastic model for sample consisting of two-ball clumps (initial porosity=0.36)

Table 6.3: The material properties for analytical solution of cavity expansion

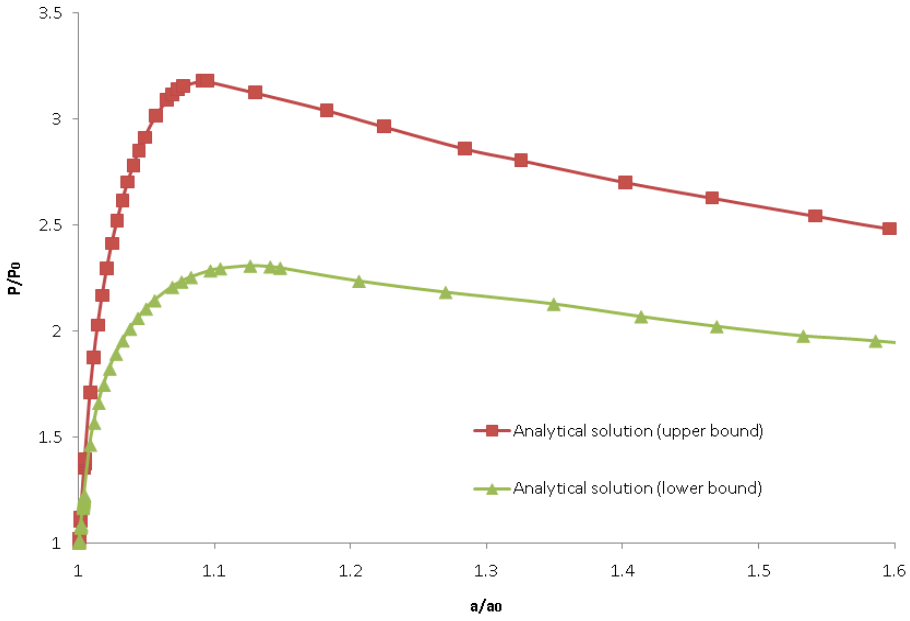

(a) Initial porosity=0.36

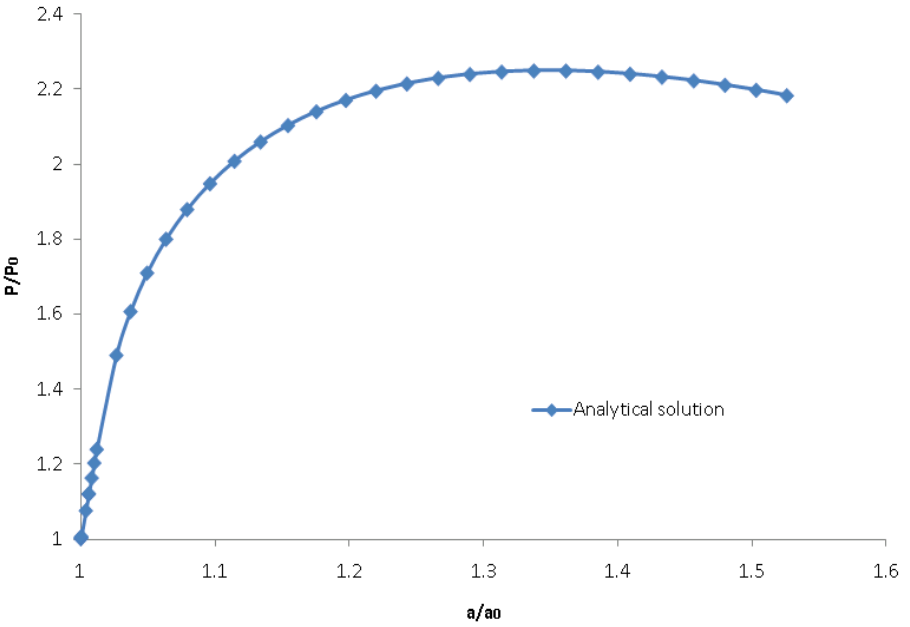

(b) Initial porosity=0.42

Figure 6.14: The theoretical analytical solutions for sample initial porosity of 0.36 and 0.42 (Initial cavity pressure=20MPa)

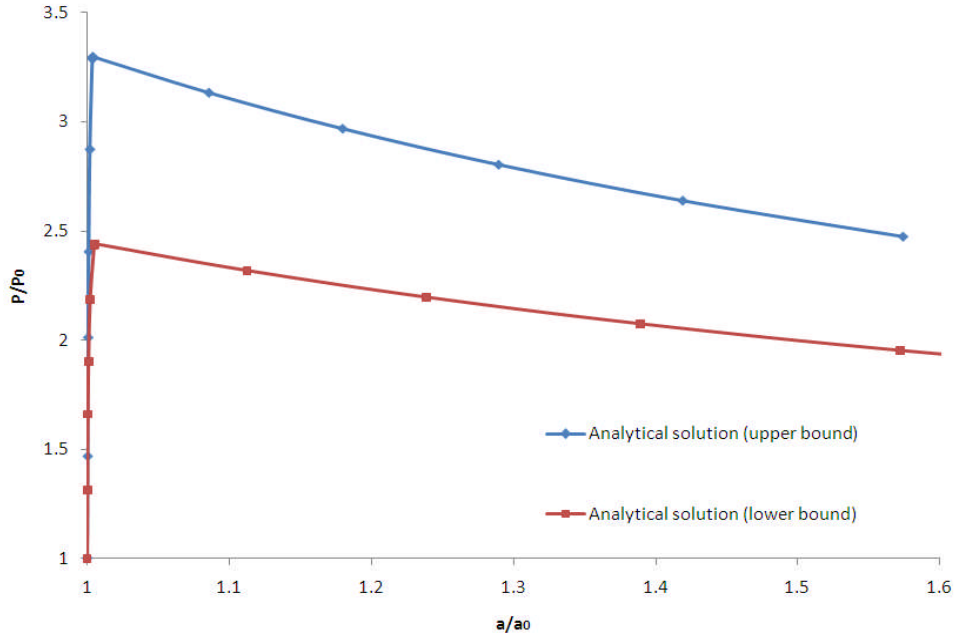

(a) Initial porosity=0.36

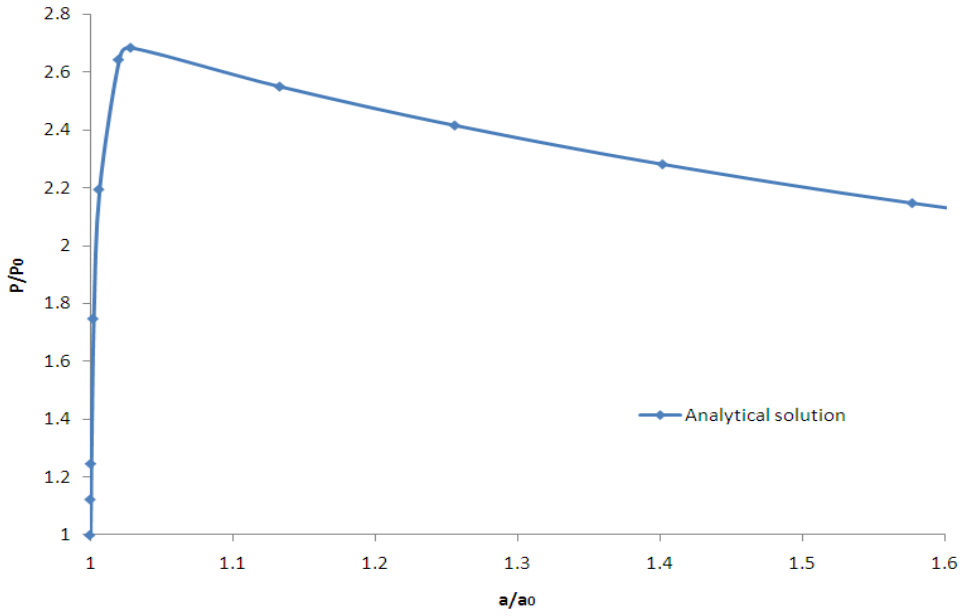

(b) Initial porosity=0.42

Figure 6.15: The theoretical analytical solutions for sample initial porosity of 0.36 and 0.42 (Initial cavity pressure=1MPa)

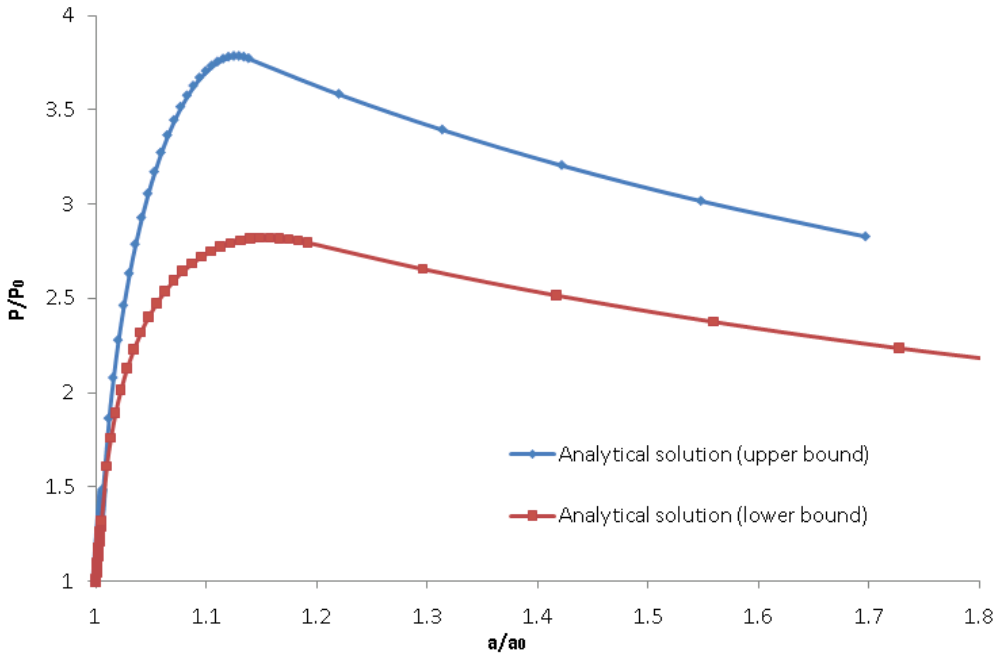

Figure 6.16: The theoretical analytical solution of cavity expansion for sample of two-ball clumps (Initial porosity n=0.36)

6.3.3 Comparison of DEM results and analytical solutions

The DEM simulation results of cylindrical cavity expansion using spherical particles (Figure 6.7 and Figure 6.8) are compared with the ones obtained from theoretical solutions (Figure 6.14 and Figure 6.15). The comparisons are shown in Figure 6.18 and Figure 6.19. Figure 6.17 presents the comparison results of DEM simulation of cavity expansion using two-ball clumps (Figure 6.10) and theoretical solutions (Figure 6.16). These figures show the simulation and theoretical results, in term of cavity pressure ratio (P/P_0) against internal radius ratio (a/a_0). Both the analytical solution and the DEM solution for the samples of same initial porosity and same initial cavity pressure are plotted in these figures to demonstrate a direct comparison.

As expected, the DEM simulation results are just in between of upper bound and lower bound values of the analytical solutions (Figure 6.17, Figure 6.18 (a) and Figure 6.19(a)). As to another two samples, the initial porosity value of 0.42, only one elastic-perfectly plastic model is used to describe the soil behaviour, the results are shown in Figure 6.18 (b) and Figure 6.19 (b). As can be seen from these figures, the simulation result gives a good fit to the theoretical result. That means DEM can be used to simulate the cavity expansion in granular materials and the results show a great agreement with the theoretical analytical solutions.

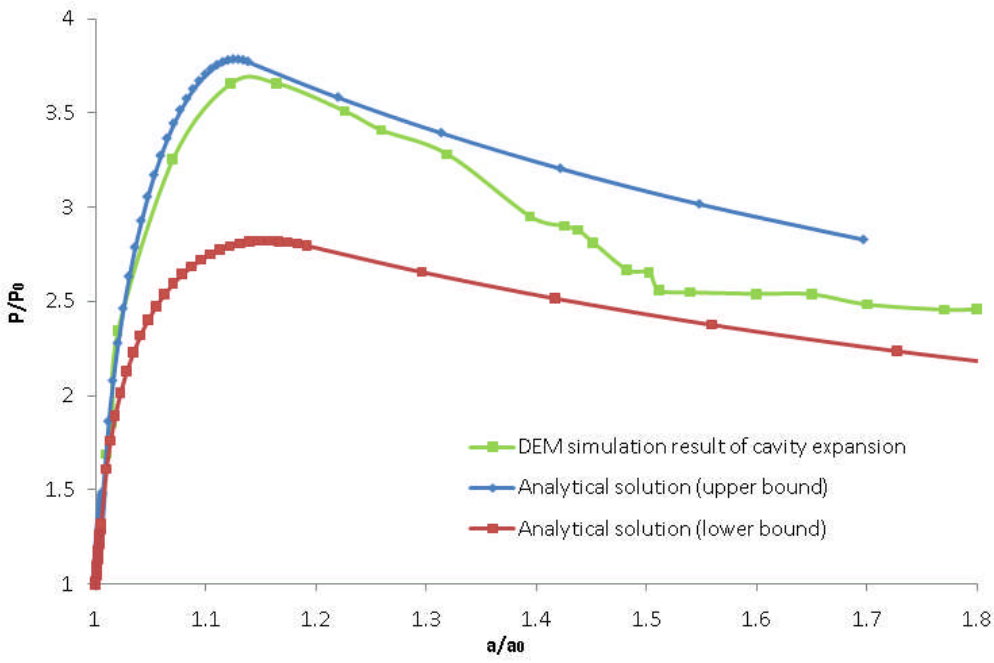

Figure 6.17: The compansion of DEM simulation result and analytical solution (Sample of initial porosity n=0.36 and particle of two-ball clumps)

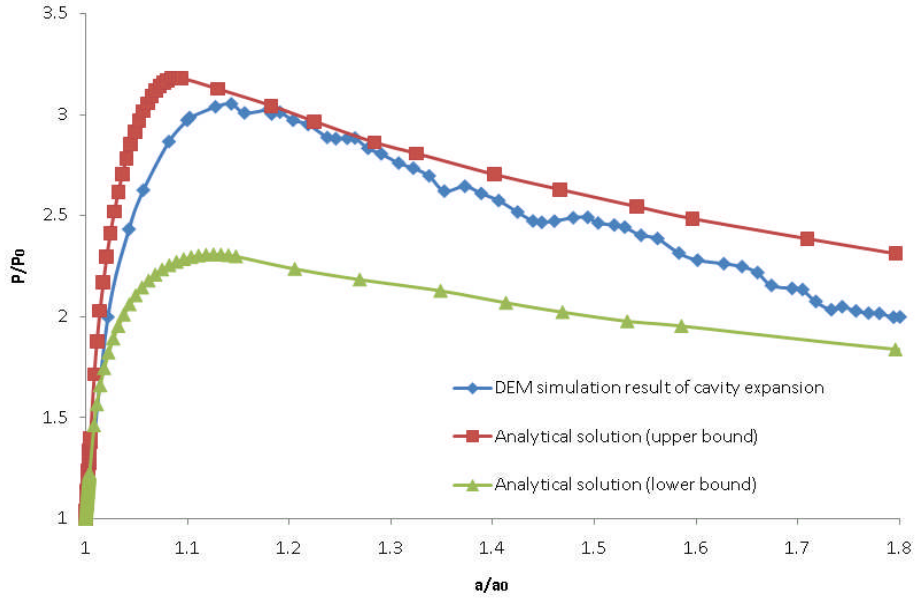

(a) Initial Porosity=0.36

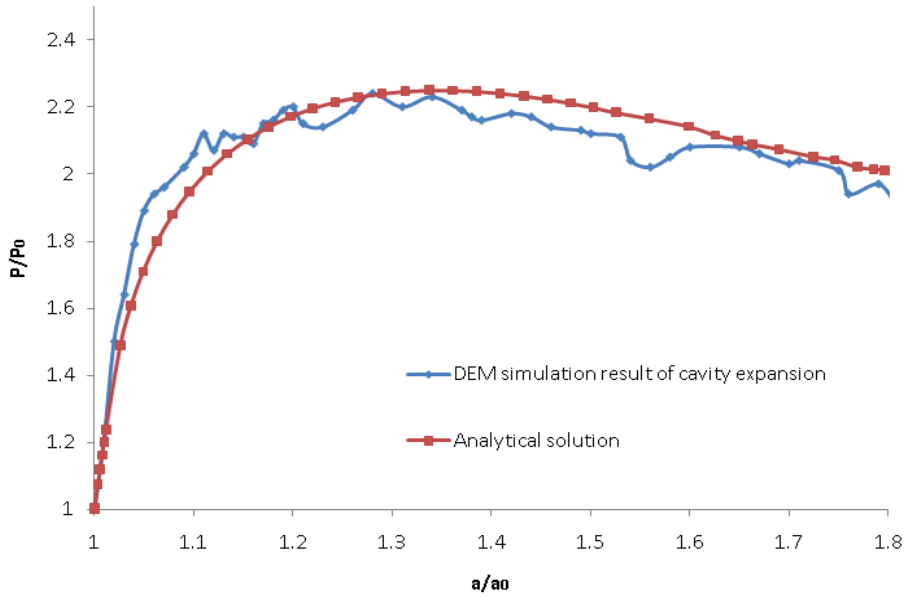

(b) Initial Porosity=0.42

Figure 6.18: The comparison of DEM simualtion results and analytical solutions (Initial cavity pressure=20MPa)

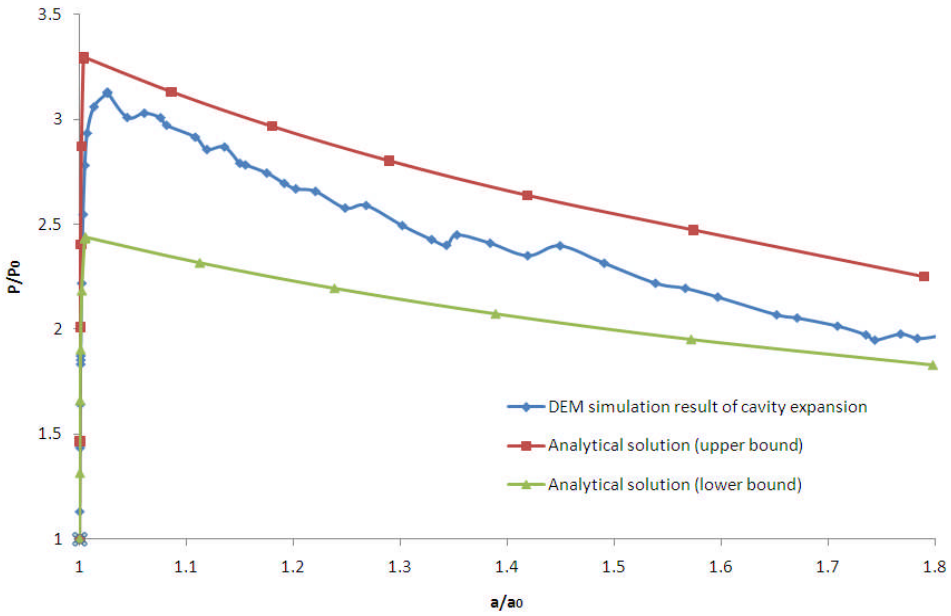

(a) Initial Porosity=0.36

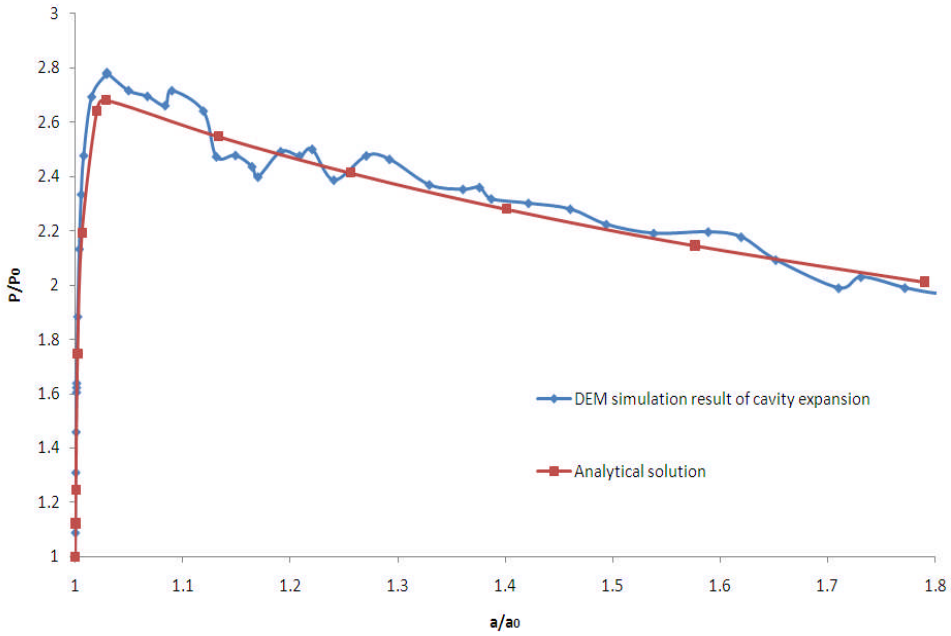

(a) Initial Porosity=0.42

Figure 6.19: The comparison of DEM simualtion results and analytical solutions (Initial cavity pressure=1MPa)

6.4 Conclusions

In this chapter, a numerical analysis of cylindrical cavity expansion in a granular material is investigated with the aid of DEM. While the analytical approach works at a macroscopic level, the numerical method has the advantages of providing the mechanical behaviour of the granular assembly at both the macro- and micro- scales. The cylindrical cavity expansion stress-strain curves of cohesionless granular material under monotonic loading are studied.

The comparison of the simulation results with the theoretical results shows a good agreement. DEM is a useful method to simulate cylindrical cavity expansion in a granular material using spherical or non-spherical particles. These simulation results need to be compared with the experimental results. The results presented in this chapter have shown that the DEM was able to capture accurately the macro scale response of the cavity expansion problem in granular material by comparison to the analytical data obtained from the cavity expansion method.

Particle shape plays a significant role in the behaviour of granular material. The early DEM models usually considered the granular material as assemblies of interacting spheres and reproduced results qualitatively well. However, materials consisting of non-spherical particles behave significantly differently from those consisting of spherical particles (Lin and Ng, 1997). More recent DEM developments focus on the shape of the particles to get more reliable results (Jensen et al., 2001; Lu and McDowell, 2007). Using complex non-

spherical shaped clump to represent each particle in cavity expansion simulation is required for the further research.

Particle parameters have a considerable effect on the simulated behaviour. Another procedure which permits the generation of clumps of spheres is being developed for comparison with experimental results of calibration chamber tests. Next chapter will focus on studying the validity of the DEM solutions by comparing them with the results of cavity expansion tests conducted in the laboratory.

CHAPTER 7

PRESSUREMETER TEST SIMULATIONS

7.1 Introduction

Interpretation of tests on real granular media, such as sand, is difficult because the stresses inside the sample cannot be measured straightly and must be estimated from the boundary conditions. The numerical analysis of discrete element method technique starts with basic constitutive laws at interparticle contacts and the macroscopic response of particle assemblage after loading can be obtained using this method. In this research, PFC^{3D} was used to simulate the soil behaviour in the pressuremeter test. The particles used in the simulation followed the relative particle size distribution of Leighton Buzzard sand. This sand is tested in laboratory by Fahey (1980) and these results are used for comparison. The specific size of sample can be adjusted by changing the actual sample size of simulations in proportion to the laboratory sample size. The influence of the micro-properties of the granular material on the macroscopic stress-strain behaviour observed in the DEM simulation can be obtained.

As far as granular soils are concerned, DEM is popularly used to simulate the granular soil behaviour. The properties of particles can be defined in the DEM which is very difficult to describe in the other method. The DEM has been

widely used for granular materials with respect to the fundamental behaviours such as macro failure criteria of granular materials (Thornton, 2000) and shear strength functions of unsaturated granulates (Jiang et al., 2004). The DEM is able to monitor the evolution of internal stresses and deformation patterns in a non-destructive manner with the comparison of experiments. It also facilitates sample reproducibility. It provides a powerful numerical tool for modeling the mechanical behaviour of granular material and for studying the micromechanical behaviour of granular material. Few studies have been carried out using DEM analysis of pressuremeter test in granular material. DEM has succeeded used to simulate some cavity expansion problems, like penetration test. Many researchers have focused on this problem. DEM is also used for solving the boundary condition problems like bearing cavity of granular ground (Ting et al., 1989). Huang and Ma (1994) were the first to use DEM in deep penetration simulation in sand. In their paper, the DEM-BEM simulation technique was described. The granular soil mass near the penetration was simulated by the discrete element method (DEM). However, the soil mass was simulated using the boundary element method (BEM) in the far field, where the strain is expected to be small. The cone penetration mechanism can be evaluated without the complication caused by boundary effects using this method. Later the study on soil-penetrometer interface friction was described by Jiang et al. (2006). A two-dimensional discrete element method (DEM) has been used to simulate the deep penetration tests on a granular ground. Cavity expansion can be used to describe the pressuremeter test, so DEM might be used in the pressuremeter test simulation.

Cavity expansion processes are relevant to pressuremeter testing. The theory of

cylindrical cavity expansion has been adapted by geotechnical researchers and engineers as the most important interpretation method for self-boring pressuremeter tests in soil and rock. It is also used to describe the soil properties of cone pressuremeter tests. This chapter presents a numerical study on pressuremeter tests in granular materials to focus on the effect of particle properties. A range simulation of various initial porosities using different particle shapes has been carried out. In particular, the key contribution is to show that the validity of pressuremeter test can be correctly modelled using discrete element method, providing micromechanical insight into the behaviour.

7.2 Experimental Data

The pressuremeter test (PMT) is a well established in-situ test in geotechnical engineering for estimation of soil properties such as deriving strength and stiffness parameters (Fahey, 1986). These tests consisted essentially of expanding a thick cylinder of sand under conditions of plane strain. In a PMT, the pressure in the cavity is increased above the in situ horizontal pressure. Displacement is purely radial and is constant with depth through the material. In all the tests the initial value of the outer boundary pressure was constant during the loading. The element is subjected to plane strain deformation. Pressuremeter development has involved advances both in respect of the equipment and theoretical. The introduction of the pressuremeter into geotechnical practice is described by Menard in the late 1950's (Menard, 1957). It was a device which was inserted into a preformed borehole to measure the strength and stiffness of the surrounding soils and rocks. More general

descriptions of the development of the pressuremeter and associated theories are provided in references by Baguelin et al. (1978), Wroth (1984) and Mair and Wood (1987). Over the last three decades, the pressuremeter has been developed in the areas of the equipment and analysis and it is recent widely used in site investigation to evaluate in situ soil properties. It is necessary for pressuremeter testing to perform proper calibrations of the instrument (Mair and Wood, 1987). Therefore, calibration of a pressuremeter is very important if accurate estimates of soil properties are required. Recently, Ajalloeian (1996) focus on the effect of pressuremeter length on derived soil properties from both loading and unloading pressuremeter tests. Finite-element analysis of a two-dimensional axisymmetric was used to simulate pressuremeter tests and it was found that the finite pressuremeter length has a significant effect on the soil properties.

Fahey (1980) performed a series of pressuremeter tests on dense samples of sand at initial pressure 90kPa. The soil used in this study was Leighton Buzzard Sand and the particles are subrounded and contain mainly quartz. Figure 7.1 is the variety of different sizes and shapes of the sand particles which influence the number of interparticle contacts per unit volume. The small pressuremeter was modelled on that originally designed by Hughes (1973). The plane strain apparatus was designed for the purpose of controlling the conditions at the top and bottom boundaries of the deforming region during a pressuremeter test (Figure 7.2). Figure 7.2 shows sections in elevation (Section Y-Y) and plan (Section X-X) through the assembles apparatus.

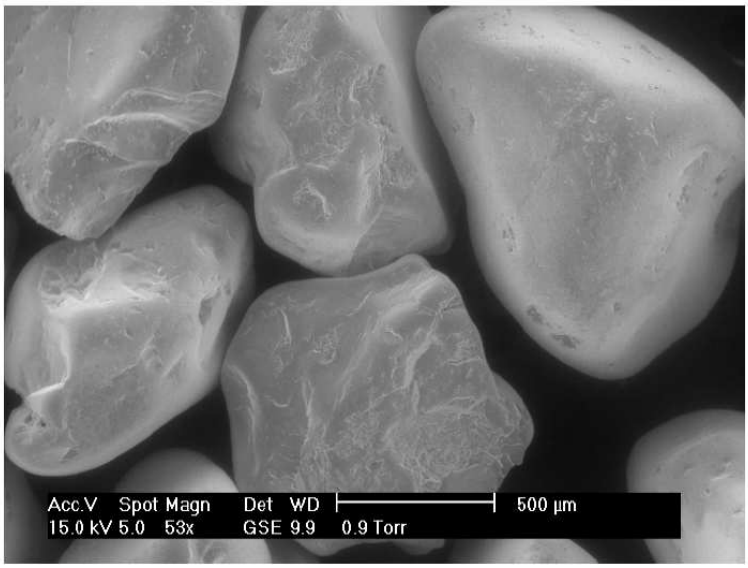

Figure 7.1: Microphotograph of Leighton Buzzard Sand (Fahey, 1980)

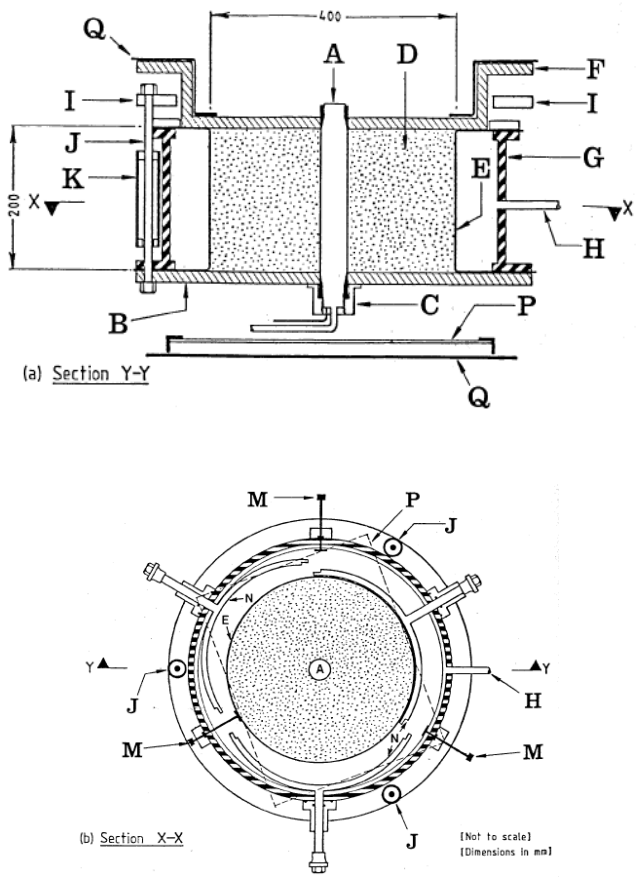

Figure 7.2: Section through the plane strain apparatus (Fahey, 1980)

The top and bottom plates of the apparatus were machined flat and ground to a mirror finish, with end friction being further reduced by greasing the plates and placing a sheet of thin latex rubber between the sand and the plates. Measured expansion volumes must also be corrected for the effects of system compliance in order to give the true cavity expansion volume (e.g. Baguelin et al., 1978 and Mair and Wood, 1987). The sample was prepared by pouring sand very slowly from a hopper suspended about 1 m above the container to achieve a reproducible sample of maximum density. The average voids ratio measured in this manner was 0.5115, so the initial porosity is 0.34. The tests were performed in the thick cylinder apparatus with frictionless top and bottom boundaries. In all tests, the initial value of the outer boundary pressure was set to 90KPa. SC test (test with smooth ends and constant boundary pressure) results with the pressure-expansion curves for four tests in the SC group are presented in Figure 7.3 (Fahey, 1980).

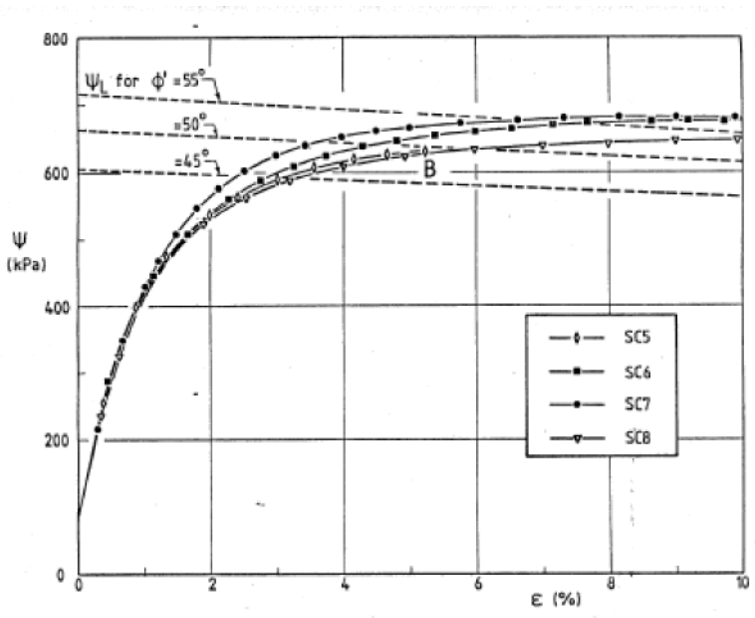

Figure 7.3: Pressure-expansion curves for four SC tests (Fahey, 1980)

7.3 Modelling Procedure

7.3.1 The DEM Code

The DEM code PFC^{3D} was used to simulate pressuremeter test on samples consisting of spheres or clumps (Figure 7.4). A clump is an agglomerate of overlapping spheres. Each clump here comprises two sphere particles of different sizes. If R and r are the radii of the larger and smaller spheres respectively and L is the distance between the centres of two spheres in each clump, the relationship among them are L=R and r=0.75R. The clumps were formed by creating initial spheres, of the same size as the simulations using spherical particles. “Virtual spheres” were then created by deleting the initial spheres and creating a virtual space by multiplying the initial sphere diameter by a factor of 1.27. Each “virtual sphere” formed the outermost possible boundary for each clump and the clumps were created in the “virtual spheres. The model is composed of distinct particles that displace independently of one another and interact only at contacts or interfaces between the particles.

(a) (b)

Figure 7.4: PFC^{3D} model (a) single sphere as a particle; (b) two-ball clump as a particle

A clump is a single entity of overlapping balls (i.e. the balls comprising the clump remain at a fixed distance from each other). Internal overlapping contacts are ignored in calculations, resulting in a saving of computational time compared to a similar calculation in which all contacts are active. For the clumps, the total volume of balls in a clump is greater than the volume of the clump because of balls overlap. The mass of the clump is therefore greater than the mass of an equivalent clump with a uniform density. The entity such as this is not available in PFC^{3D} currently. There is a contribution to the mass in the overlapping region from each of the overlapping balls. This may not influent the mechanical behaviour of the clumps under static loading. However, when the dynamic effect of the clumps is significant, the influence of mass due to overlapping balls will become significant. A modified density can be used in each clump for further research. In order to achieve the desired mass, the modified density ρ_m is derived from the initial density ρ_0 as

$$\rho_m = \frac{V_{clump} \cdot \rho_0}{\sum V_i} \tag{7.1}$$

Where V_i is the volume of the i^{th} ball in the clump and V_{clump} is the volume of the clump and

$$\sum V_i = \sum V_i^{overlap} + V_{clump} \tag{7.2}$$

Where $\sum V_i^{overlap}$ is the volume of overlap in the clump. In such dynamic simulations, density can be scaled to give the correct particle mass, but the distribution of mass will be incorrect, leading to incorrect moments of inertia and hence rolling resistance. Therefore, density is not scaled to fit correct mass

in these simulations.

7.3.2 Sample preparation

Fahey (1986) described thick cylinder tests of sand to simulate pressuremeter tests. The nominal initial sample dimensions are 40mm in diameter and was expanded in a cylindrical sample of sand with 400mm in diameter by 200mm long in the experimental test. The experimental test was contained in an apparatus which allowed the outside boundary pressure constant and no axial movement to occur. The material used in these tests is composed of Leighton Buzzard sand with maximum diameter of 4mm, and a minimum diameter of 0.15mm, as shown in Figure 7.5.

Due to the geometric symmetry of the problem concerned, only a quarter of the sample was considered in the analyses. The sample was loaded by the internal circular boundary using a constant strain rate. The velocity of the external boundary was automatically controlled by a servo-mechanism (see Appendix) to keep a constant external pressure (Figure 7.6).

The samples had dimensions of approximately 60.0mm in external diameter × 6.0mm in internal diameter × 30.0mm in height with more than 10000 particles in each sample, which follow the relative sample size of laboratory test, but proportionally smaller. There are too many particles generated if the same sample geometry with experimental test is used. Multiple-sized particles of approximately 0.15mm - 4mm diameter were used in order to model the particle size distribution in the laboratory test by Fahey (1986). The density of the particles is 2650kg/m^3.

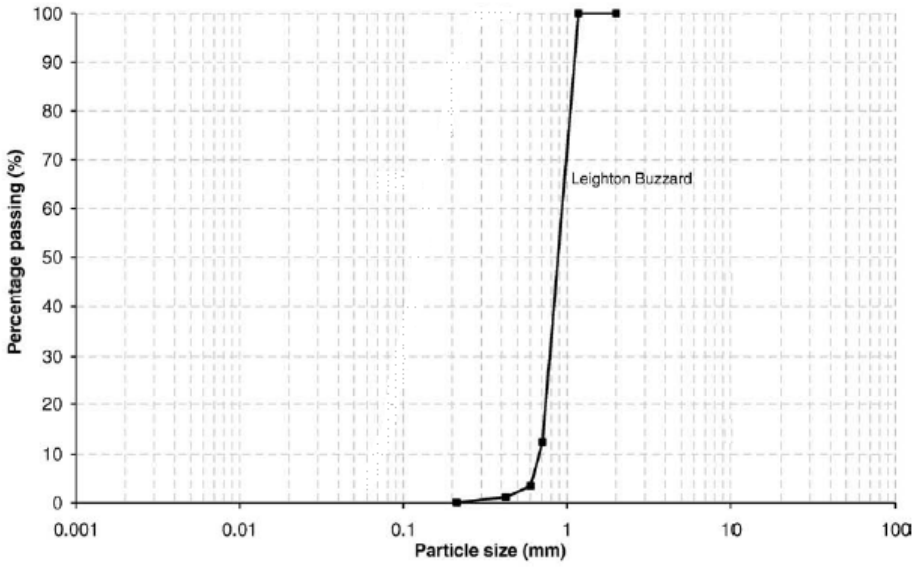

Figure 7.5: Particle size distribution of Leighton Buzzard sand

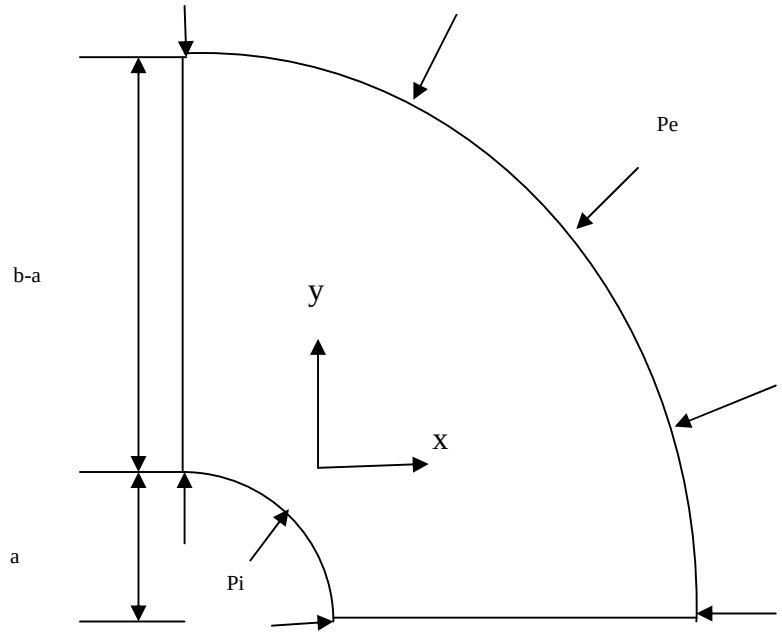

Figure 7.6: Schematic illustration of cavity expansion

Figure 7.7 shows PFC^{3D} models of the pressuremeter test and granular material particle models use single spheres or 2-ball clumps. The initial porosity and the number of particles used in each sample of spherical particles and two-ball clumps are given in Table 7.1. In these pressuremeter test models, six walls were generated as sample boundaries. Two cylindrical vertical walls were used to simulate the flexible membrane and two horizontal walls were placed at the top and bottom of the sample, respectively. Another two vertical walls normal to x and y axes are fixed since it is an axisymmetric structure.

The normal and shear stiffness of the balls was set to 1×10^{6}N/m and the specific gravity was 2.65. A friction coefficient of 0.5 was used for all balls in the simulations. The walls were set to frictionless during each simulation. The two horizontal walls and two vertical walls had the same normal stiffness as the particles (1×10^{6}N/m). The normal stiffness of the cylindrical vertical wall was set to be one tenth of the normal stiffness (1×10^{5}N/m) of the particles in order to simulate the effect of the flexible membrane. The two horizontal walls are fixed since this is plane-strain problem.

The assemblies were generated by the particle radius expansion method. This is used to place a specified number of particles at random coordinates within a given space without overlapping. A population of spheres were initially generated by artificially small of their final diameter. The number of spheres generated in the sample was calculated from a porosity, which is set by the user. It should be noted that the porosity set by user may differ from the final porosity obtained in sample initial state shown in Table 7.1, since the final size of the sample may change slightly and the spheres may be replaced by other

shaped particles (2-ball clumps). The spheres were then expanded to their final size and the system was cycled to equilibrium with the locations of walls remaining fixed.

The Newton's second law and a force-displacement law were used in the calculations. The equations of motion were solved via a time-stepping algorithm in which contact forces were calculated from relative displacements between particles at the contact and used to calculate velocity and position of the particles and therefore updated contact forces. This process was continued until the particles were in equilibrium. In order to make particle easy to arrange, the friction coefficients for all particles were choose a small value at the beginning. If non-spherical-shaped particles were used, the spheres could be replaced by clumps with random orientation. After particles of the sample were replaced by clumps, the high contact forces were mainly produced by overlapping of the particle replacement. For reducing the high contact forces, the system was cycled to equilibrium again. After that, all walls were moved outwards at the same slow rate for obtaining an initial state free sample of internal forces at first.

	Sample 1	sample 2	sample 3	sample 4
Number of particles	7921	7942	15872	15826
Initial porosity of samples	0.38	0.32	0.37	0.28

Table 7.1: Number of particles, initial porosity of the samples in DEM simulations

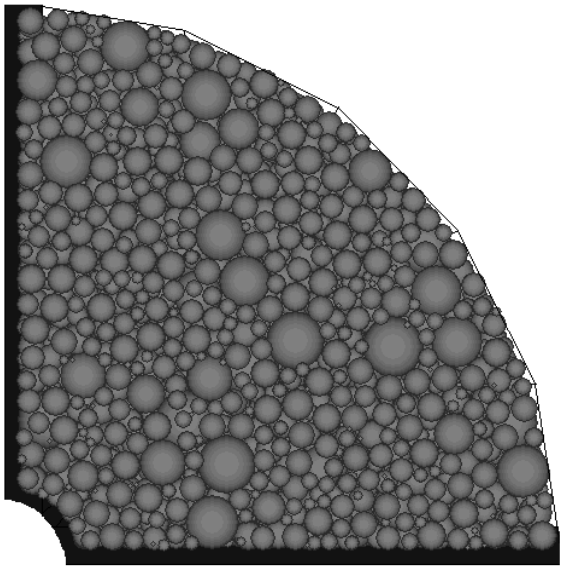

(a)

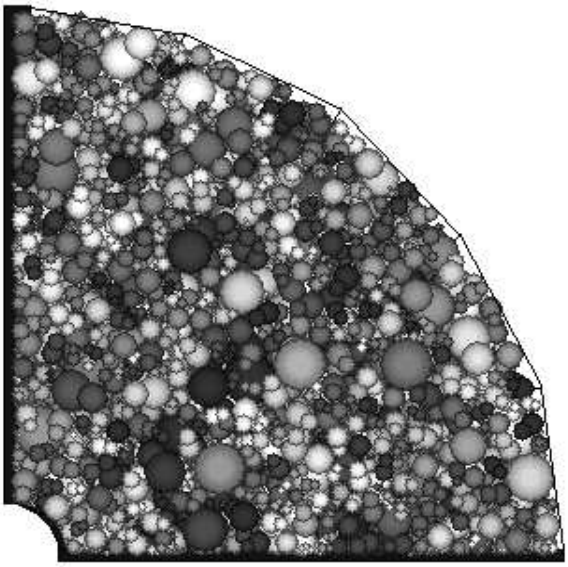

(b)

Figure 7.7: A sample of cavity expansion simulation of (a) single spherical particles (b) two-ball clumps

Artificial isotropic compression was applied to achieve the required stress state, after the sample generation procedure was completed. The required pressures could be obtained, since the servo-control (see Appendix) was applied to all walls. Stresses on the walls are determined from constant forces acting on the particles and strains experienced by tracking the relation distance between appropriate walls, respectively.

Material response is computed by recording the various stress and strain quantities using the history logic. Different initial porosities of samples were prepared using single spheres and 2-ball clumps, respectively. The different initial porosities of the samples were controlled from friction coefficients of 0.0 to 0.5 during artificial isotropic compaction. Once the initial state of the sample is reached, the friction coefficient was changed back to 0.5 for the loading stage of simulation. Monotonic loading was applied to internal wall with a constant speed of 0.01mm/s, so that the rate of loading was slow enough for the samples to remain under static loading conditions, but at the fastest rate which it did not affect the results deemed to be acceptable for saving the calculation time.

7.4 Results and Discussion

For many years, the pressure-expansion curves obtained from a pressuremeter test have been used to determine soil properties such as the shear modulus and the strength parameters. The purpose of these simulations is to get a similar typical behaviour of sand using DEM simulation compared to experimental results. In this chapter, simulations using different interparticle frictions, particle shapes and sample initial porosities will be discussed. The effect of the

micro-properties of granular material on its cavity expansion behaviour has been investigated using a three-dimensional, numerical simulation of a standard laboratory pressuremeter test. All the simulations were operated with particle rotation allowed in this research.

7.4.1 The particle shape

Particle shape plays a significant role in the behaviour of granular material. The behaviour of materials which consists of non-spherical particles is significant different from those consisting of spherical particles (Lin and Ng, 1997). Using complex irregular-shaped clumps to represent each particle in the pressuremeter test simulation is not practical due to the calculations being too time-consuming. However the spherical shape is too idealized to represent real granular material elements like sand grains. The real sand particle is irregular and involves more complex intergranular interactions than spherical particles.

For these reasons, a simple non-spherical particle of two-ball clump was used in these simulations. In this research, two simple shapes were used in the pressuremeter test simulations to represent the soil particle. The shapes (sphere and two-ball clump) are shown in Figure 7.4. The simulation results by using spherical particles and clumps are compared with the experimental result from Fahey (1986) to obtain a better model for modelling pressuremeter test of granular materials.

Table 7.1 lists the properties of each sample. Sample 1 and sample 2 are loose and dense samples constitutive of spherical particles. While sample 3 and sample 4 are loose and dense samples made up of two-ball clumps. The initial

porosities of these samples were produced by using different particle friction coefficients 0.0 and 0.5 under 90kPa isotropic compaction. For the sample consisting of either spherical particles or two-ball clumps, it is possible to calculate the porosity using a measurement sphere, which is a function in PFC^{3D}. The porosity of each sphere can be obtained. The finial initial porosity for each sample is the average value of all measurement spheres in the sample. So many spheres are needed to cover the entire sample.

The porosity of the samples produced by using different friction coefficients (e.g. μ=0.0 for dense samples and μ=0.5 for loose samples) for each particle shape model is listed in Table 7.1. Monotonic loading was applied to each sample under a constant external pressure of 90KPa. The cavity expansion curves of these samples are plotted in Figure 7.8 and Figure 7.9. Figure 7.8 shows the simulation results of sample consisting of spherical particles together with experimental data and Figure 7.9 shows the comparison of simulation results of sample consisting of two-ball clumps and experimental data. This experimental data was chosen from one of the experimental data in Figure 7.3 (SC7).

Comparing with the experimental data (Fahey, 1986), the results of sample consisting of spherical particles are both lower than the experimental data, as shown in Figure 7.8. While the result shown in Figure 7.9 is different, this experimental data is between the results of loose sample and dense sample using clumps.

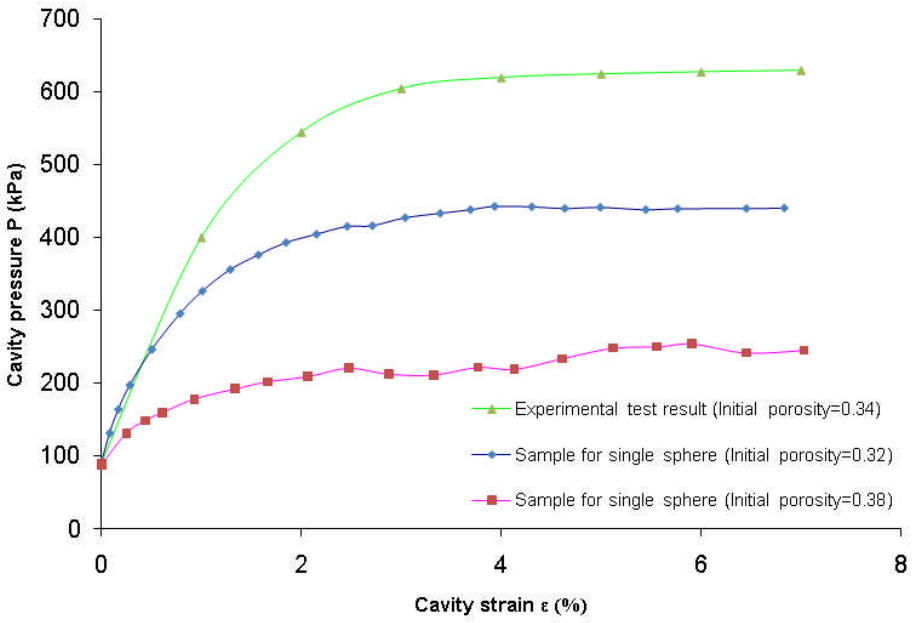

Figure 7.8: Results of pressuremeter test simulation for both dense and loose samples using single spheres

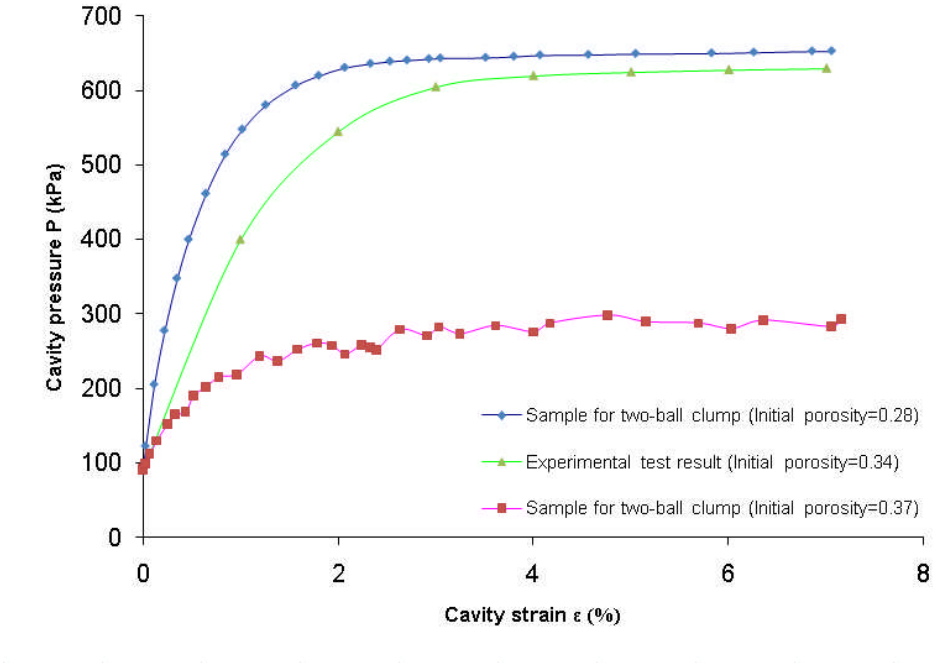

Figure 7.9: Results of pressuremeter test simulation for both dense and loose samples using two-ball clumps

Figure 7.10 shows the contact force for dense sample consisting of spherical particles and clumps after compaction, prior to loading. It can be seen that the contact forces are reduced for two-ball clumps (sample 4), which is in agreement with the results published by Lu and McDowell (2007), and that the stress distribution for the clumps is more homogeneous because of the higher number of contacts for sample 4. Figure 7.11 shows the contact forces for these two samples after loading. The force around the internal wall was higher than the other position since the internal wall is used to apply the loading. Comparing with Figure 7.10, it can be noted that the number of contacts does not change much during the loading. The more contacts in the sample of two-ball clumps cause a more homogenous stress distribution, so the magnitude of the mean contact force for sample using clumps is less than that for the sample using spheres. Figure 7.12 shows the particle displacement vectors for the samples of spheres and two-ball clumps drawn at the same scale. It can be seen that the displacements of spheres on the side of internal wall are larger than those displacements on the side of external wall and the displacements are generally outwards. It is well known that more interlocking is displayed between the clumps than spheres, so the displacement for the sample of clumps is a little different. For the clumps, the particle displacements are bigger around the side of internal wall and the displacements are outwards too. However, the displacement distribution for the clumps is more homogeneous than that for the spheres because the higher number of balls leads to more displacement vectors. These particle displacements of samples were indicated at the same cavity strain. The displacements are generally outwards for these samples, since loading is applied.

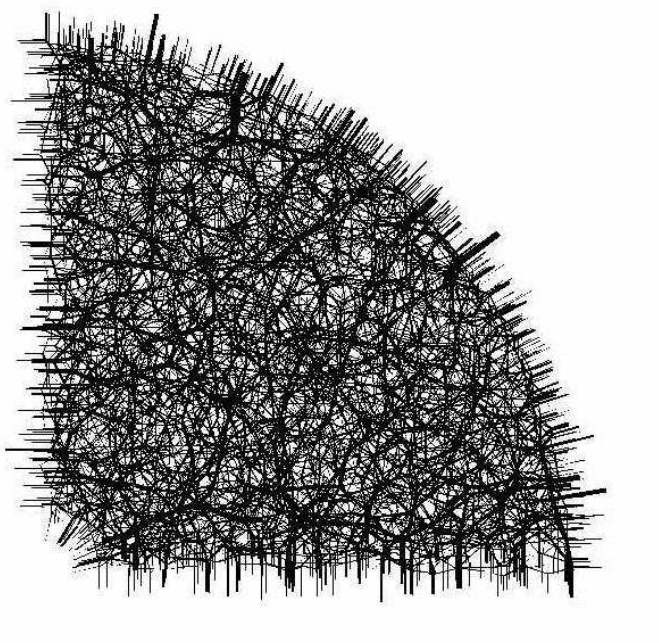

(a)

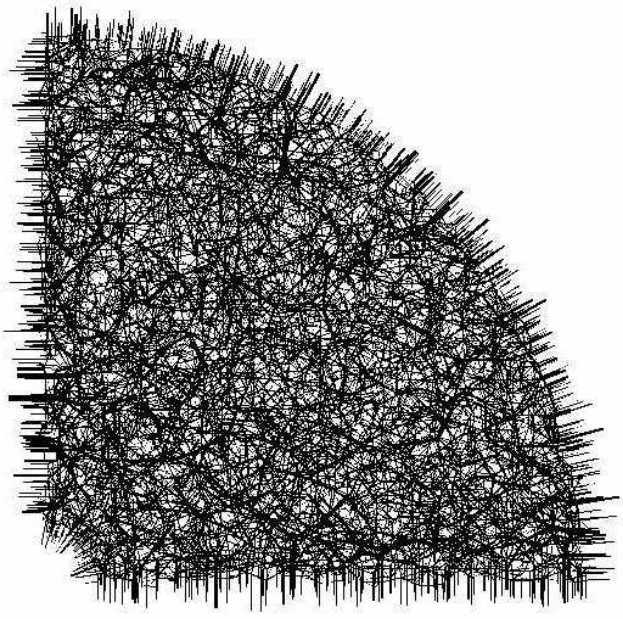

(b)

Figure 7.10: Contact force for dense sample of a) spherical particles (sample 2: number of contacts=27791) and b) two-ball clumps (sample 4: number of contacts=50268) prior to loading

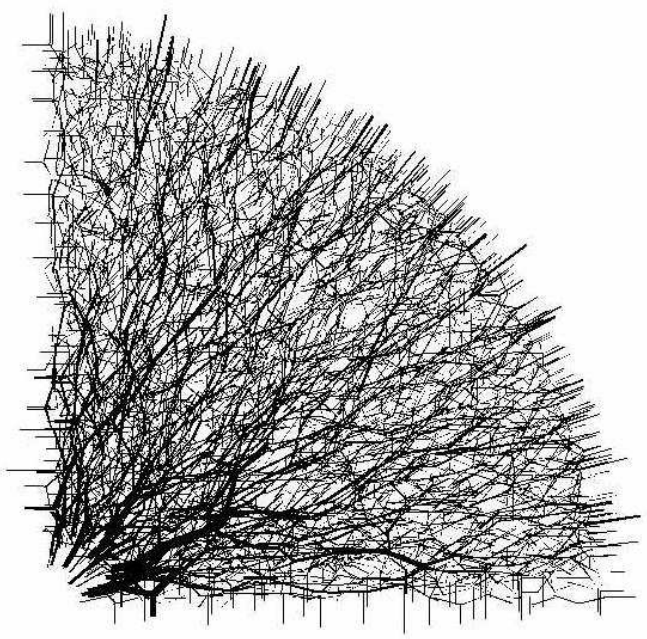

(a)

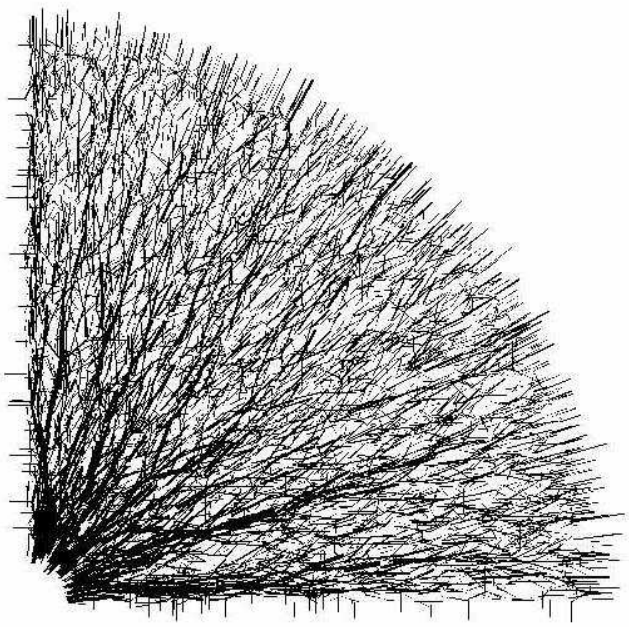

(b)

Figure 7.11: Contact force for dense sample of a) spherical particles (sample 2: number of contacts=27800) and b) two-ball clumps (sample 4: number of contacts=50106) after loading

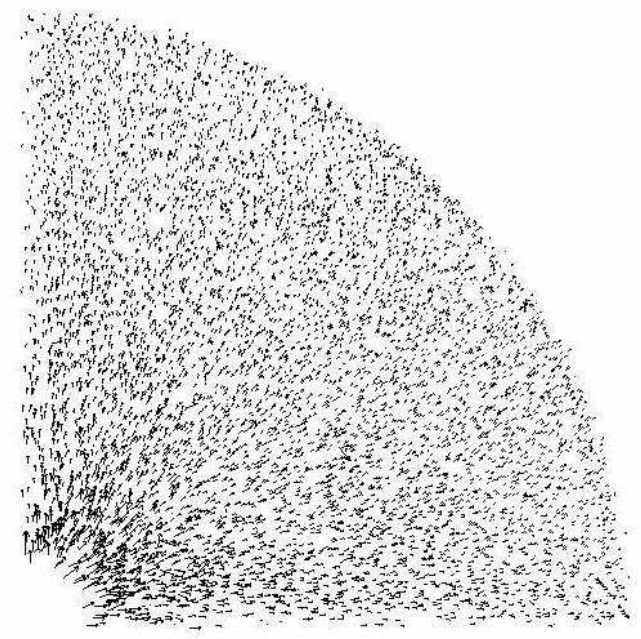

(a)

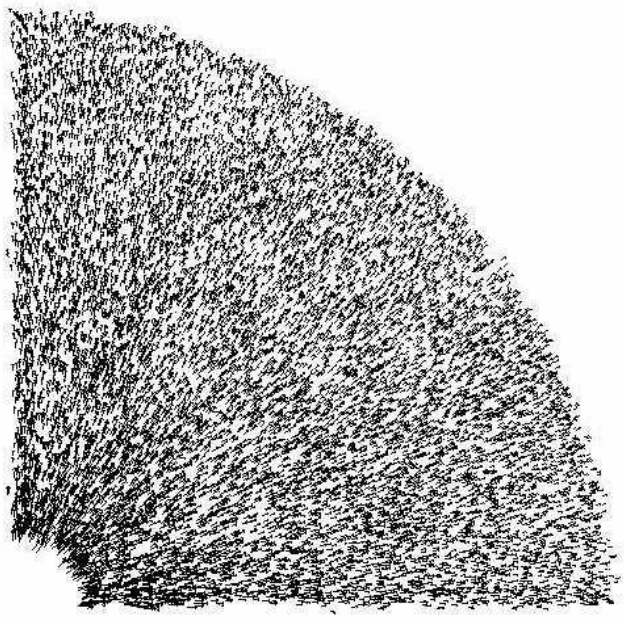

(b)

Figure 7.12: Total displacements for sample of a) spherical particles and b) two-ball clumps after loading

It can be noted that the stress-strain response of an assembly depends not only on the particle shape but on interparticle friction as well (Lu and McDowell, 2008). A series of simulations was performed to investigate the effect of friction coefficient. Different particle friction coefficients (varying from 0.5 to 0.9) were applied to the sample with dense random packing of spherical particles. The effect of particle friction coefficient on the cavity expansion curve is shown in Figure 7.13 for just the dense samples. It can be seen that the friction coefficient has a large effect on the cavity expansion curve when the friction coefficient is lower than 0.7. However, it makes little difference to the behaviour of cavity expansion when the friction coefficient is changed from 0.7 to 0.9. Comparing with experimental result (as shown in Figure 7.13), the cavity expansion curves in the simulations are still lower than that of the experimental test, even when a high friction coefficient is used.

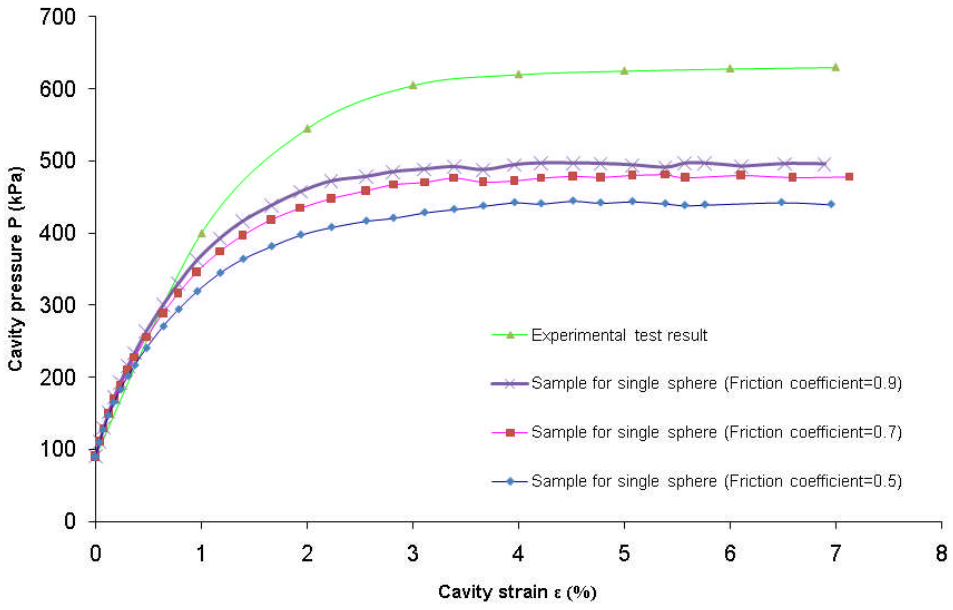

Figure 7.13: Effect of particle friction coefficient on expansion curve of spherical particles

Therefore, the correct behaviour cannot be modelled by purely increasing the friction coefficient. A real sand particle is typically non-spherical with a rough surface texture (as shown in Figure 7.1) and particle interlocking plays an important role in the soil behaviour of cavity expansion. The different particle friction coefficients (0.5, 0.7 and 0.9) were used in the dense and loose sample of clumps as well. Cavity pressure for different particle friction coefficients of these samples during cylindrical cavity expansion is plotted in Figure 7.14, that the same results were observed in Figure 7.13. The cavity expansion curve increases with the particle friction coefficient increasing. The behaviour of cavity expansion is affected by the particle friction coefficient, especially when the friction coefficient is low. After the particle friction coefficient was high enough, the particle friction coefficient did not obvious influence the behaviour of cavity expansion. It can be seen in Figure 7.13 and Figure 7.14, the interparticle friction has made a contribution to the maximum cavity pressure, but does not affect the stiffness of samples much.

The general results of different particle shapes are discussed before. As can be seen in Figure 7.8 and Figure 7.9, the maximum cavity pressure increase with particle angularity increasing and increasing particle angularity gives a higher sample initial stiffness. The material used in the laboratory test is Leighton Buzzard sand. The real shape of particle is non-spherical, so the particle shape must be the principal reason to affect the material behaviour in the simulations. It can be seen in Figure 7.8 and Figure 7.9, the laboratory test can be simulated better using clumps than spheres. The simulation result with clumps is similar to the experimental test result than the one with spheres.

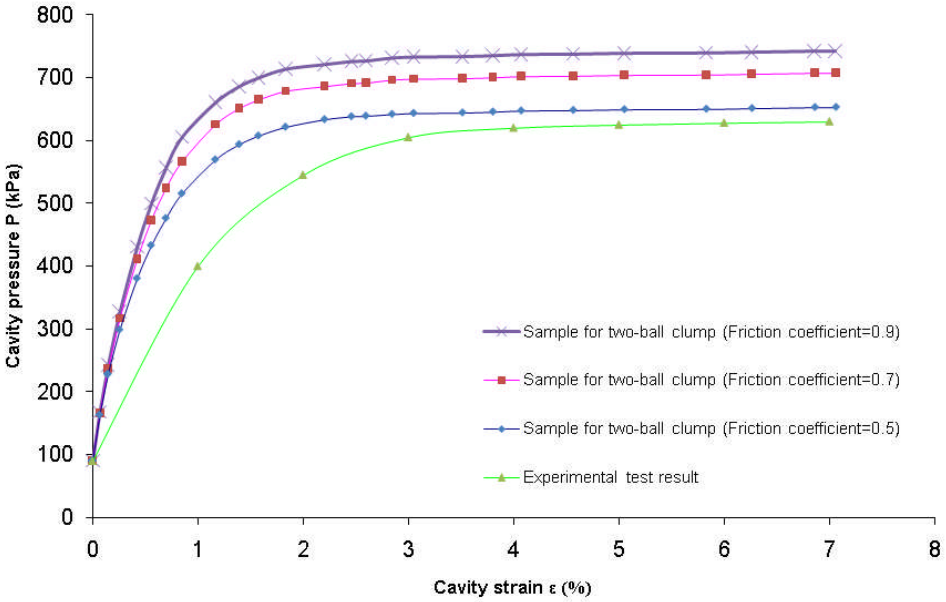

(a)

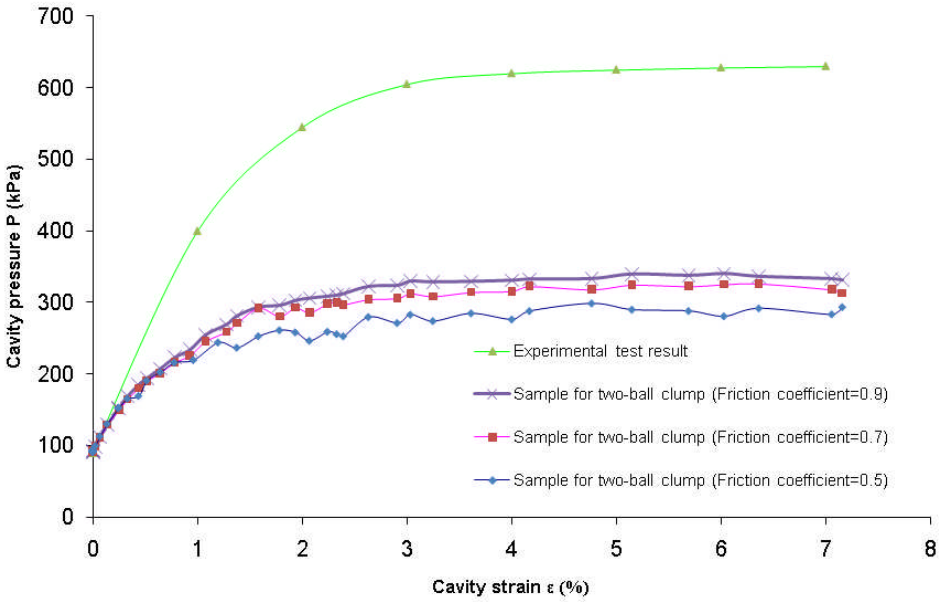

(b)

Figure 7.14: Effect of friction coefficient on expansion curve using two-ball clumps (a) dense sample (b) loose sample

The experiment data is between the results of dense and loose samples using two-ball clumps, as shown in Figure 7.9. The closer simulation result to the experimental data could be obtained when the initial porosity is selected between the porosities of these two samples. In this case, the sample of similar initial porosity with experimental test needs to generate for the simulation. More generally, the particle is generated using two-ball clump which is closer to the real material element than spheres.

7.4.2 The sample porosity

The experimental results are compared with the results of existing simulation results, but the initial sample porosities are all different from the sample in the experimental test. Simulation of a material's macro behaviour using DEM is difficult as the choice of micro-properties is complicated. Further, the validity of current simulation methods of pressuremeter tests will be assessed by comparison with the experimental results. From the comparison result in Figure 7.14, it can be noted that the sample of similar porosity with the experimental test in the simulation is required. One simulation result using sample consisting of two-ball clumps with the initial porosity of 0.33 and particle friction coefficient of 0.5 is compared with the experimental test data (the porosity in the experimental test is 0.34), as shown in Figure 7.15. We can see that this simulation result is closer to the experimental result comparing with the results in Figure 7.8 and Figure 7.9. However, the simulation result is still lower than the experimental data. It is clear to see that increasing the sample initial porosity to 0.34 (the initial porosity in the experimental test) causes the sample cavity expansion curve lower, not higher. That means the

sample porosity changing from 0.33 to 0.34 can not make the comparison result better. Though the porosity 0.34 is performed in the experimental test, the particle shape in the simulation is not exactly same with the real soil element shape in the experimental test. We can not expect to get the better result using the same initial porosity with the experimental test since different particle shapes of samples are used.

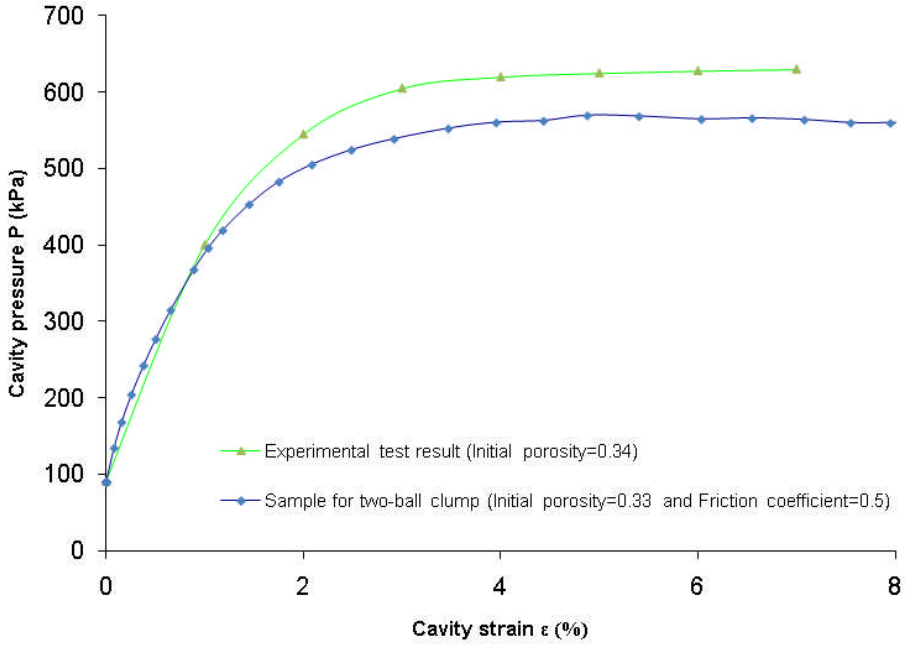

Figure 7.15: Results of comparison between the experimental data and DEM simulation of two-ball clumps using particle friction coefficient of 0.5

It can be noted that the interparticle friction has an important effect on the maximum cavity pressure, as shown in Figure 7.14. The maximum cavity pressure increases when the particle friction coefficient increases. The particle friction coefficient 0.7 was used in the simulation and compared with the experimental result together with the result using particle friction coefficient of 0.5, as shown in Figure 7.16. The particle properties and sample initial

porosities are shown in Table 7.2. As we expected, the experimental data is between these two simulations results and the difference of them is very small. We consider that DEM can simulate the pressuremeter test properly if realistic particle shape and properties are used in simulations.

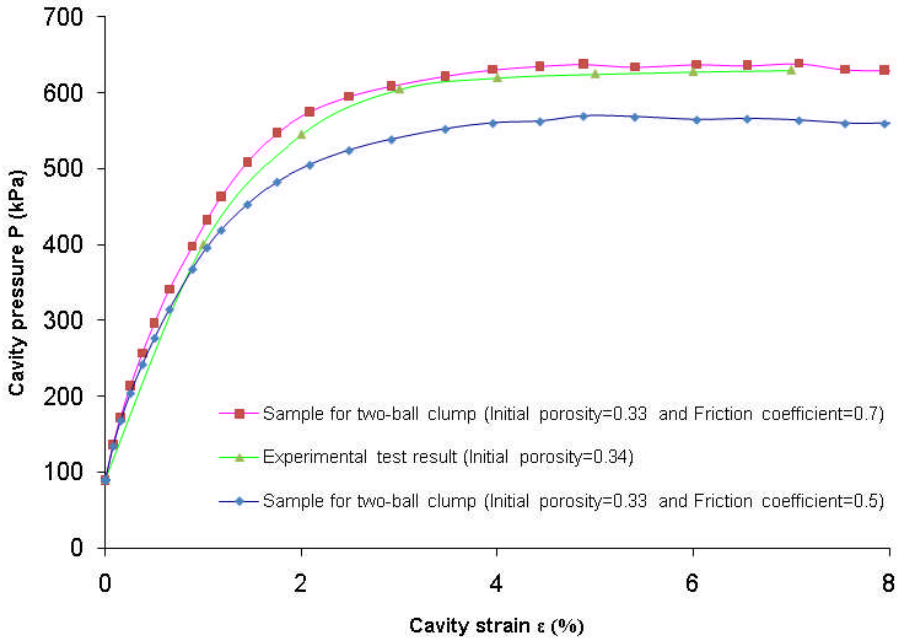

Figure 7.16: Results of comparison between the experimental data and DEM simulation of two-ball clumps using particle friction coefficient of 0.5 and 0.7 and initial porosity of 0.33

Sample	Initial porosity	Particle friction coefficient and stiffness	
Sample of two-ball clumps	0.33	0.5	1×10^6N/m
	0.33	0.7	1×10^6N/m

Table 7.2: Particle properties and initial porosities of the samples in DEM simulations

7.4.2.1 Limit pressure

In Figure 7.16, it is demonstrated that the limit pressure would be reached at a cavity strain ε of about 7% for the experimental data. For the pressure-expansion curves of two simulations using two-ball clumps, the maximum pressure were reached at a strain of about 5% for both of them. It can be seen in Figure 7.16, limit pressure for experimental test data was around 610kPa at cavity strain ε=7%, while the limit pressures obtained in the DEM simulation were 580kPa and 630kPa at around the same cavity strain ε =5%. It is clear that the limit pressure in the experiment test occur at cavity strain ε=7%, which is a little late than that in both of two DEM simulation results (the limit pressure happen at cavity strain ε=5%). Figure 7.16 shows that the DEM simulation results have a good agreement with the experimental test data. The limit pressure in the experimental test is between that in these two simulation results.

7.4.2.2 Dilation angle

The dilative behaviour of granular material is very important. Dense granular materials will dilate during shear due to the interlocking between the soil particles. One of the fundamental issues to model the stress-strain behaviour of a soil is to correctly describe its dilatancy. Dilatancy is used to describe the increase in volume of dense sand during shearing, the maximum rate corresponding to the peak stress. A parameter known as the angle of dilation (ψ) is defined to represent the rate of dilation. In a conventional in situ pressuremeter test, displacement measurements can only be made at the cavity wall. It is difficulties in calibrating the system and only qualitative results were obtained. While comparing with the experimental method, the inner and outer

boundary displacements can be recorded easily using PFC^{3D} program in the DEM simulation.

In the Figure 7.17, the displacement of the outer boundary (ξ_b) is plotted against the displacement of the cavity wall (ξ_a) for the simulations of two-ball clumps using particle friction coefficient of 0.5 and 0.7. The plot is initially curved and thereafter can be approximated by linear portion. Based on the equation 7.3, the dilation rate can be determined using slope ξ_b/ξ_a (Jewell et al., 1980). The values of ψ can be obtained using this manner for the performed simulations using particle friction coefficient 0.5 and 0.7, as the two straight lines shown in Figure 7.17.

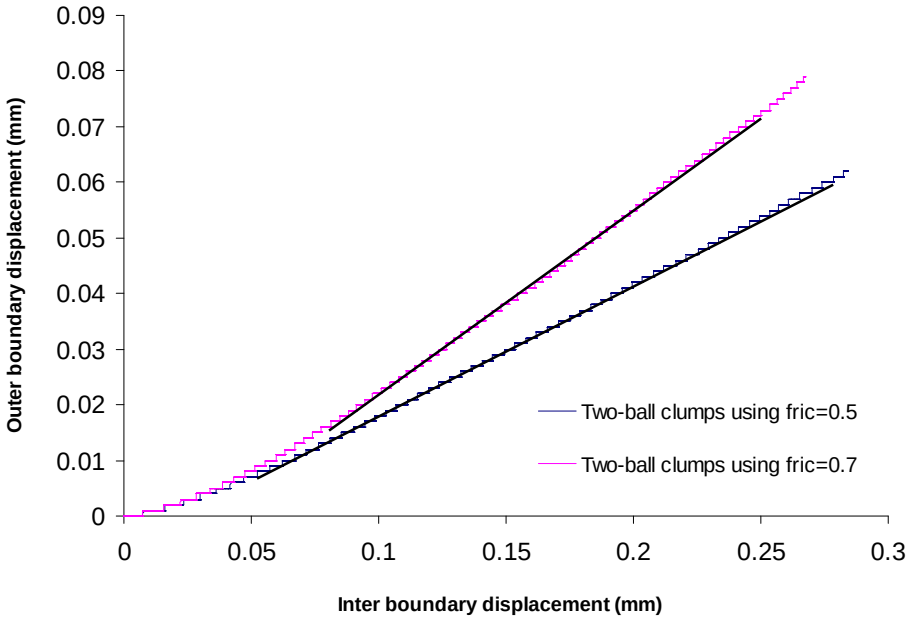

Figure 7.17: Boundary displacements of simulation using samples of two-ball clumps and particle friction coefficients of 0.5 and 0.7

It can be concluded that the dilation angle for the sample of particle friction coefficient 0.5 and 0.7 are 16° and 23° using equation 7.3. While the dilation

angle in the experimental test was 19° (Fahey, 1986). It is clear that this result is coincident with the result obtained before (Figure 7.16). The dilation angle of sample in the experimental test is between the angles of samples in the DEM simulation.

$$\frac{\log(\xi_b / \xi_a)}{\log(a/b)} = n = \frac{1-\sin\psi}{1+\sin\psi} \tag{7.3}$$

Where ξ_a, ξ_b are radial displacement at the inner and outer boundaries; a and b are inner and outer radii of a cylinder; ψ is dilation angle.

7.5 Conclusions

DEM successfully simulates the typical granular material behaviour in the pressuremeter test. These simulations show that particle properties have a great effect on the soil behaviour. The comparison between the DEM simulation results and the laboratory test results shows that the result using clumps is better than the result using spheres. The peak cavity pressure and friction angle of sample increase when the particle friction coefficient increases or when the particle shape is irregular.

The comparison of the DEM simulation result and the experimental test data shows a good agreement. The key contribution is that the pressuremeter test of granular materials can be modelled using DEM, providing micromechanical insight into the behaviour. The validity of the DEM solutions has been assessed by comparing them with the results of pressuremeter tests conducted in the laboratory.

CHAPTER 8

CONCLUSIONS AND SUGGESTIONS FOR FUTURE RESEARCH

8.1 Summary and Conclusions

The aim of cavity expansion simulation is to investigate the effect of micro parameters on macro response of granular material during the cavity expansion condition. A three-dimensional discrete element method computer code PFC^{3D} has been used to investigate the mechanical response of cohesionless granular materials under cavity expansion. In this study, granular materials have been modelled by spheres and non-spherical particles (two-ball clumps). DEM simulations of cavity expansion and laboratory tests in the pressuremeter test were performed to investigate the effects of particle properties and sample initial state for assemblages on their mechanical response. Particles of 0.075m-0.1m diameter were used to simulate a granular material during cavity expansion, and the effects of the interparticle friction, particle shape and initial porosity of an assemblage on its cavity expansion curve were investigated using numerical simulations. Particle followed the size distribution of Leighton Buzzard sand was used to simulate the pressuremeter test.

8.1.1 Effect of the particle shape and interparticle friction

Particle properties play an important role in determining the mechanical behaviour of granular material. Simulation of material behaviour using DEM is difficult as the particle properties are complicated to choose. The effects of particle friction coefficient and particle shape on the cavity expansion behaviour have been studied in the monotonic loading. The conclusions are:

1. The friction coefficient between the particles has a large effect on the maximum cavity pressure, but not on the ultimate cavity pressure. The peak value of cavity pressure increases when the particle friction coefficient increases.
2. A simple procedure has been developed which permits the generation of clumps of overlapping spheres to simulate different particles. In the pressuremeter test simulations, the mean contact forces of sample using clumps are found to become lower and more homogeneous than that of spherical particles.
3. Results using the angular clumps show a more realistic response than those using spheres by comparing with laboratory test results. This difference can be attributed to the interlocking provided by the angular clumps, which affects the rolling resistance and particle displacements.
4. The effect of particle shape is also studied in the cavity expansion simulations. Both peak cavity pressure and ultimate cavity pressure increase with increasing particle angularity, and increasing particle angularity give a higher initial stiffness.

8.1.2 Effect of sample initial state

The effect of sample initial states on soil behaviour in cavity expansion has been investigated. The mechanical behaviour of granular material under monotonic loading of different initial states has been investigated in the cavity expansion. Sample initial porosity and initial cavity pressure both play a significant role in the DEM simulation of cavity expansion. The conclusions are:

1. From the simulations of samples using different initial porosities, it is found that the maximum cavity pressure increases significantly while the value of initial porosity decreases. However, the initial porosity does not affect the ultimate cavity pressure much. All the ultimate cavity pressures reach almost the same value for different initial porosities.
2. Simulations of different initial cavity pressures were conducted. It can be seen that the value of cavity pressure increased with increasing the cavity pressure level at a given cavity strain. It can be easily obtained that increasing the initial cavity pressure increases the soil resistance.

The comparison of the simulation results with the theoretical results shows a good agreement. The key contribution is to show that the cavity expansion of granular materials can be modelled using DEM, providing micromechanical insight into the soil behaviour. Cavity expansion analysis can be used to explain the soil behaviour in the pressuremeter test and the validity of DEM solutions of the pressuremeter test can be proved by comparing them with the results of the pressuremeter tests conducted in the laboratory.

8.2 Suggestions for Further Research

The results of sample using spherical particles with no bond for the cavity expansion have been examined by comparing with analytical solution using cavity expansion method. Particle shape significantly affects the response of the granular material. The future work in this research will investigate more different shaped particle models in cavity expansion simulation. The same particle properties will be used in the biaxial test simulations to investigate the material behaviour and sample properties for the cavity expansion method to obtain the analytical solutions.

Pressuremeter test is an application of cavity expansion. DEM has been used to simulate in this pressuremeter test. The simulations carried out in this research focus on the simple shaped particles. In the future work, more realistic particle shape models will be used to get a better result since particle shape is an important factor. However, it should be noted that the size and shape of fragment in the natural particle are determined by contact force distribution of flaws in the particle. Therefore, in further work, the particle model should also be able to capture realistic particle fracture.

As for the clumps (spheres overlap), the total volume of spheres in a clump is greater than the volume of the clump (overlap between spheres in the clump counted once), and the mass of the clumps is therefore greater than the mass of a clump (overlap between spheres in the clump counted once) with a uniform density. As there is overlapping of spheres within a clump, a contribution to the mass in the overlapping region from each of the overlapping spheres is considered. This also affects the moment of inertia tensor of the clump since

the mass is not uniformly distributed within the clump. A method for producing clumps with uniform density and correct moment of inertia tensor is needed to be developed in the future.

A cylindrical wall was used to simulate a flexible membrane in the research. The real flexible membrane can not be simulated since the displacement of wall always keeps the same. Alternative methods should be developed in the future to model the real flexible boundary conditions. Although, it is possible to simulate a flexible membrane using a large number of bonded balls, this makes the computations too time-consuming. Consequently, a better method is required. Capturing the particle shape and flexible boundary is a goal in further research. Particle shape determines the contact force distribution under the same loading condition, boundary condition and particle arrangement.

For reducing the calculation time, a quarter of the sample was generated since this is axisymmetric problem. In this case, extra two boundaries were generated which do not exist in the real problem. The real problem can not be simulated because of the boundary effects in these simulations. A better boundary is required to model the real problem. Periodic boundary is often used to simulate a large system by modelling a small part. To eliminate boundary effects in the computation, simulation using periodic boundary is needed to be developed in the future.

It has been shown that the discrete element method provides a useful micro mechanical insight into the behaviour of granular material. However, the contact mechanics between real particles is not fully understood in this

research. Future research can study contact mechanics for real particle and develop a more realistic and effective contact constitutive model in DEM.

REFERENCES:

Ajalloeian, R. (1996). *An Experimental Study of Finite Pressuremeter Length Effects in Sand*, Ph.D, Thesis, University of Newcastle, Australia.

Ajalloeian, R. and Yu, H. S. (1998). Chamber studies of the effects of pressuremeter geometry on test results in sand, *Geotechnique,* 48, 621-636.

Antonio, G. F. (1990). Radial expansion of cylindrical cavities in sandy soils: application to pressuremeter tests, *Canadian Geotechnical Journal,* 67, 737-748.

Baguelin, F., Jezequel, J. F. and Shields, D. H. (1978). *The Pressuremeter and Foundation Engineering*, Trans Tech Publications.

Bardet, J. P. and Proubet, J. (1991). A numerical investigation of the structure of persistent shear bands in granular media, *Geotechnique,* 41, No.4, 599-613.

Bardet, J. P. and Proubet, J. (1992). Shear-bond analysis in idealized granular material, *J.Engrg.Mech.,ASCE,* 118, No.2, 397-415.

Bathurst, R. J. and Rothenburg, L. (1988). Micromechanical aspects of isotropic granular assemblies with linear contact interactions, *J.Appl.Mech*., 55, 17-23.

Bishop, A. W. (1954). Correspondence on shear characteristics of a saturated silt measured in triaxial compression, *Geotechnique,* 4, No.1, 43-45.

Bishop, R. F., Hill, R. and Mott, N. F. (1945). The theory of indentation and hardness tests, *Proc.,ESOPT 2*, Vol.2, Amsterdam, 439-446.

Chadwick, P. (1959). The quasi-static expansion of a spherical cavity in metals and ideal soils Part 1, *Q. J. Mech. Appl. Math*., 12, 52-71.

Clarke, B. G. (1995). *Pressuremeter in Geotechnical Design*, Chapman and Hall, London.

Cundall, P. A. (1971). A computer model for simulating progressive large scale movements in blocky rock systems. *Proceedings of the Symposium of the International Society of Rock Mechanics, Nancy, France*, Vol.1, Paper No. II-8.

Cundall, P. A. and Hart, R. D. (1992). Numerical Modelling of Discontinua, *Engineering Computations*, 9,100-113.

Cundall, P.A. and Strack, O. D. L. (1979). A discrete numerical model for granular assemblies, *Geotechnique*, 29, 47-65.

Darius, M. and Rimantas, K. (2006). Compacting of particles for biaxial compression test by the discrete element method, *Journal of Civil*

Engineering and Management, Voll2, No.2, 153-161.

Dinesh, S. V., Sitharam, T. G. and Vinod, J. S. (2004). Dynamic properties and liquefaction behaviour of granular materials using discrete element method, *Current science,* Vol.87, No.10.

Dixon, N., Whittle, R. W., Jones, D. R. V. and Ng'ambi, S. (2006). Pressuremeter tests in municipal solid waste: measurement of shear stiffness, *Geotechnique,* 56, 211-222.

Drake, T. G. and Shreve, R. L. (1986). High-speed motion pictures of nearly steady, uniform, two-dimensional, inertial flows of granular material, *Journal of Rheology*, Vol.30, No.5, 981-993.

Fahey, M. (1980). *A Study of The Pressuremeter Test in Dense Sand*, Ph.D, Thesis, University of Cambridge, London, U.K.

Fahey, M. (1986). Expansion of a thick cylinder of sand: a laboratory simulation of the pressuremeter test, *Geotechnique,* 36, No.3, 397-424.

Favier, J. F., Abbaspour-Fard, M. H., Kremmer, M. and Raji, A. O. (1999). Shape representation of axisymmetrical, non-spherical particles in discrete element simulation using multi-element model particles, *Engineering computations,* 16, 467-480.

Frossard, E. (1979). Effect of sand Grain shape on interparticle friction: indirect measurements by Rowe's stress dilatancy theory, *Geotechnique,* 29, 341-350.

George, Z. V., Mehmet, T. T. and Panos, D. K. (1990). Finite stain analysis of pressuremeter test, *Journal of Geotechnical Engineering*, Vol. 116, No.6.

Gibson, R. E. and Anderson, W. F. (1961). In-situ measurement of soil properties with the pressuremeter, *Civ. Engng. Publi. Wks. Rev*., 56, 615-618.

Golightly, C. R. (1990). *Engineering properties of carbonate sands*, Ph.D. dissertation, Bradford University.

Gong, G. (2008). *DEM Simulations of Drained and Undrained Behavior*, Ph.D, Thesis, University of Birmingham, Birmingham, U.K.

Hill, R. (1950). *The Mathematical Theory of Plasticity*, Oxford University, London.

Hogue, C. (1998). Shape representation and contact detection for discrete element simulation of arbitrary geometries, *Engineering Computations*, 15, 374-390.

Hogue, C. and Newland, D. E. (1994). Efficient computer simulation of moving granular particles, *Powder Technology*, Vol.78, 51-66.

Horne, M. R. (1968). The behaviour of an assembly of rotund, rigid cohesionless particles, *Proceedings of the Royal Society*, Vol.286 of A, London. The Royal Society, 67-97.

Houlsby, G. T. and Withers, N. G. (1988). Analysis of the cone pressuremeter test in clay, *Geotechnique*, 38, 573-587.

Houlsby, G. T. and Yu, H. S. (1990). *Finite element analysis of the cone-pressuremeter test*, Oxford.

Huang, A. B. and Ma, M. Y. (1994). An analytical study of cone penetration tests in granular material, *Canadian Geotechnical Journal*, 31, 91-103.

Huang, Z-Y., Yang, Z-X. and Wang, Z-Y. (2008). Discrete element modeling of sand behavior in a biaxial shear test, *Journal of Zhejiang University SCIENCE A*, 9(9), 1176-1183.

Hughes, J. M. O. (1973). *An instrument for the in situ measurement of the properties of soft clays*, Ph.D, Thesis, University of Cambridge, London, U.K.

Hughes, J. M. O., Wroth, C. P. and Windle, D. (1977). Pressuremeter tests in sands, *Geotechnique*, 27, 455-477.

Institute for Geotechnical Engineering. (2005). Large-strain dynamic cavity expansion in a -granular material, *Engineering Mathematics*, 52, 185-198.

Itasca, (1999). *Particle Flow Code in Three Dimensions*, Itasca Consulting Group, Inc., Minnesota.

Iwashita, K. and Oda, M. (1998). Rolling resistance at contacts in the simulation of shear band development by DEM, *J. Eng.Mech.Div.ASCE*, 124, 285-292.

Jensen, R. P., Edil, T. B., Bosscher, P. J., Plesha, M.E. and Kahla, N.B. (2001). Effect of particle shape on interface behaviour of DEM-simulated

granular materials, *The International Journal of Geomechanics*, Volume 1, Number 1, 1-19.

Jewell, R. J., Fahey, M. and Wroth, C. P. (1980). Laboratory studies of the pressuremeter test in sand, *Geotechnique*, 30, No.4, 507-531.

Jiang, M. J., Leroueil, S. and Konard, J. M. (2004). Insight into shear strength functions of unsaturated granulates by DEM analysis, *Computers and Geotechnics*, 31, 473-489.

Jiang, M. J., Yu, H-S. and Harris, D. (2006). Discrete element modeling of deep penetration in granular soils, *Int. J. Numer. Anal. Meth. Geomech*., 30, 335-361.

Juran, I. and Mahmoodzadegan, B. (1989). Interpretation procedure for pressuremeter tests in sand, *Journal of Geotechnical Engineering*, Vol.115, No.11.

Khan, A. S. and Huang, S. (1995). *Continuum theory of plasticity*, John Wiley&Sons, New York.

Kishino, Y. (1988). Disc model analysis of granular media. Micromechanics of granular materials, Satake and Jenkins (eds), *Elsevier Science Publishers*, Amsterdam, Netherlands, 143-152.

Kokusho, K. (1980). Cyclic triaxial test of dynamic soil properties for wide strain range, *Soil.Found.*, 20, 45-60.

Kruyt, N. P. and Rothenburg, L. (2004). Micromechanical study of macroscopic friction and dissipation in idealised granular materials: the effect of interparticle friction, (refereed paper on CD ROM number SM 20L-10866)). In W. Gutkowski & T.A. Kowalenski (Eds.), *ICtam04 Abstract Book en CD-Rom Proceedings,* Warszawa: IPPT Pan Warszawa, (ISBN 83-89687-1).

Ladanyi, B. (1963). Expansion of a cavity in a saturated clay medium, *J. Soil. Mech. Fdns. Eng. Div. ASCE*, 89(4), 127-161.

Lee, K. L. and Seed, H. B. (1967). Drained strength characteristics of sands, *Journal of the soil mechanics and foundations division, ASCE, 93 (SM6)*, 117-141.

Lu, M. and McDowell, G. R. (2007). The importance of modeling ballast particle shape in the discrete element method, *Granular Matter*, 9, 69-80.

Lu, M. and McDowell, G. R. (2008). Discrete element modelling of railway ballast under triaxial conditions, *Geomechanics and Geoengineering: An International Journal*, Vol. 3, No. 4, 257-270.

Lim, W. L. and McDowell, G. R. (2005). Discrete element modelling of railway ballast, Granular Matter 7, No. 1, 19-29.

Lin, X. and Ng, T.-T. (1997). Three-dimensional discrete element method using arrays of ellipsoid, *Geotechnique*, 47, 319-329.

Lobo-Guerrero, S. and Vallejo, L. E. (2005). Crushing a weak granular material: experimental numerical analyses, *Geotechnique*, Vol.55, 3, 243-

249.

Lorig, L. J. and Brady, B. H. G. (1984). A hybrid computational scheme for excavation and support design in jointed rock media, *Design and performance of Underground Excavations*, ISRM/GBS, Cambridge, England, 105-112.

Mair, R. J. and Wood, D. M. (1987). *Pressuremeter testing methods and interpretation*, Construction Industry Research and Information Association, Butterworths.

Malvern, L. (1969). *Introduction to the mechanics of a continuous medium*, Prentice Hall, Inc., Englewood Cliffs, New Jersey.

McDowell, G. R. (2002). On the yielding and plastic compression of sand, *Soils and Foundations*, Vol.42, No.1, 139-145.

McDowell, G. R. and Bolton, M. D. (1998). On the micromechanics of crushable aggregates, *Geotechnique* 48, No. 5, pp. 667-679.

McDowell, G. R. and Harireche, O. (2002). Discrete element modelling of soil particle fracture, *Geotechnique* 52, No.2, 131-135.

McDowell, G. R., Lim, W. L., Collop, A. C., Armitage, R. and Thom, N. H. (2005). Laboratory simulation of train loading and tamping on ballast, *Proceedings of the Institution of Civil Engineers: Transport* 158, No. TR2, 89-95.

Menard, L. (1957). *An Apparatus for Measuring the Strength of Soils in Place*,

Ph.D, Thesis, University of Illinois, Urbana, France.

Meyerhof, G. G. (1951). The ultimate bearing capacity of foundations, *Geotechnique*, Vol.2, 301.

Mitchell, J. K. (1993). *Fundamentals of soil behavior*, Wiley, New York.

Ng, T.-T. (2001). Fabric evolution of ellipsoidal arrays with different particle shapes, *Journal of Engineering Mechanics, ASCE* 127, No 10.

Ng,T.-T. and Dobry, R. (1992). A non-linear numerical model for soil mechanics, *International Journal for Numerical and Analytical Methods in Geomechanics*, 16, 247-263.

Ni, Q. (2003). *Effect of Particle Properties and Boundary Conditions on Soil Shear Behavior: 3-D numerical simulations*, Ph.D, Thesis, University of Southampton, Southampton, U.K.

Norman, G. M. and Selig, E. T. (1983). Ballast performance evaluation with box test, *AREA, Bul. 692, Proceedings* Vol. 84, 207-239.

Oda, M. (1997). A micro-deformation model for dilatancy of granular materials, *Mechanics of Deformation and Flow of Particulate Materials, ASCE*, 24-37.

Oda, M. and Iwashita, K. (2000). Study on couple stress and shear band development in granular media based on numerical simulation analyses, *International Journal of Engineering Science*, 38, 1713-1740.

Oner, M. (1984). Analysis of fabric changes during cyclic loading of granular soils, *Proc., 8th World Conf. Earthquake Engineering*, San Francisco, Calif., 3, 55-62.

Osinov, V. A. (2005). Large-strain dynamic cavity expansion in a granular material, *Journal of Engineering Mathematics*, 52, 185-198.

Palmer, A. C. (1972). Undrained plane-strain expansion of a cylindrical cavity in clay: a simple interpretation of the pressuremeter test, *Geotechnique*, 22, 451-457.

Pena, A. A., Lizcano, A., Alonso-Marroquin, F. and Herrmann, H. J. (2008). Biaxial test simulations using a packing of polygonal particles, *International Journal for numerical and analytical methods in Geomechanics*, 32, 143-160.

Peters, J. F. and Leavell, D. A. (1986). Biaxial consolidation test for anisotropic soils, *ASTM, Special Technical Publication*, 465-484.

Randolph, M. F. and Wroth, C. P. (1979). An analytical solution for the consolidation around a driven pile, Int. *J. Num. Analy. Meth. Geom.*, 3, 217-229.

Robertson, D. (2000). Numerical simulations of crushable aggregates, *Ph.D. dissertation, University of Cambridge*.

Rosenberg, Z. and Dekel, E. (2008). A numerical study of the cavity expansion process and its application to long-rod penetration mechanics, *Impact Engineering* 38, 147-154.

Rothenburg, L. and Bathurst, R. J. (1992). Micromechanical features of granular assemblies with planar elliptical particles, *Geotechnique*, 42, 79-95.

Rowe, P. W. (1962). The stress-dilatancy relation for static equilibrium of an assembly of particles in contact, *Proc. Roy. Soc. A*, Vol. 269.

Sagaseta, C. (1984). *Quasi-Static Undrained Expansion of A Cylindrical Cavity in Clay in The Presence of Shaft Friction and Anisotropic Initial Stresses*, Research report, Oxford University.

Salgado, R., Bandini, P. and Karim, A. (2000). Shear strength and stiffness of silty sands, *J.Geotech.Geoenviron.Eng., ASCE*, 126(5), 451-462.

Salgado, R., Mitchell, J. K. and Jamiolkowski, M. (1997). Cavity expansion and penetration resistance in sand, *Journal of Geotechnical and Geoenvironmental Engineering*, Vol. 123, No. 4, 344-354.

Salgado, R. and Prezzi, M. (2007). Computation of cavity expansion pressure and penetration resistance in sands, *International Journal of Geomechanics*, Vol.7, No.4.

Salgado, R. and Randolph, M. F. (2001). Analysis of cavity expansion in sand, *The International Journal of Geomechanics*, 1, 175-192.

Santamarina, J. C. and Cho, G. C. (2004). Soil behaviour: the role of particle shape, *Proc.Skempton Conf.*, London.

Schnaid, F. and Mantaras, F. M. (2003). Cavity expansion in cemented materials: structure degradation effects, *Geotechnique,* 53, 797-807.

Scott, R. F. (1963). *Principles of Soil Mechanics*, Addison-Wesley, London

Sitharam, T. G. and Dinesh, S. V. (2002). Micromechanical modelling of granular materials using three dimensional discrete element modelling, *Key Engineering Materials*, Vol.227, 73-78.

Sitharam, T. G. and Nimbkar, M. S. (2000). Micromechanical modelling of granular materials: effect of particle size and gradation, *Geotechnical and Geological Engineering*, 18, 91-117.

Skinner, A. E. (1969). A note on the influence of interparticle friction on the shearing strength of a random assembly of spherical particles, *Geotechnique,* 19, No.1, 150-157.

Tatsuoka, F., Salamoto, M., Kawamura, T. and Fukushima, S. (1986). Strength and deformation characteristics of sand in plane strain compression at extremely low pressures, *Soils and Foundation*, 26(2), 65-84.

Thornton, C. (2000). Numerical simulations of deviatoric shear deformation of granular media, *Geotechnique,* 50, No.1, 43-53.

Ting, J. M., Corkum, B. T., Kauffman, C. R. and Greco, C. (1989). Discrete numerical model for soil mechanics, *Journal of Geotechnical Engineering, ASCE* 115, 379-398.

Walton, O. R. (1983). Particle-dynamics calculations of shear flow, in Jenkins, J.T. and Satake, M.(Eds), *Mechanics of Granular Material: New Models and Constitutive Relations*, Elsevier Science, Amsterdam, 327-338.

Whittaker, B. N. and Frith, R. C. (1990). *Tunnelling design, stability and construction*, The Institution of Mining and Metallurgy, London.

Wroth, C. P. (1984). The interpretation of in-situ soil tests, *Geotechnique*, 34, No.4, 449-489.

Yasuda, N. and Matsumoto, N. (1993). Dynamic deformation characteristics of sand and rockfill materials, *Canadian Geotechnical Journal*, 30.

Yu, H. S. (1992). Expansion of a thick cylinder of soils, *Computers and Geotechnics*, 14, 21-41.

Yu, H. S. (2000). *Cavity Expansion Methods in Geomechanics*, Dordrecht, Kluwer.

Yu, H. S. and Collins, I. F. (1998). Analysis of self-boring pressuremeter tests in overconsolidated clays, *Geotechnique*, 48, 689-693.

Yu, H. S. and Houlsby, G. T. (1991). Finite cavity expansion in dilatant soils: loading analysis, *Geotechnique*, 41, 173-183.

Yu, H. S. and Mitchell, J. K. (1998). Analysis of cone resistance: review of methods, *Journal of Geotechnical and Geoenvironmental Engineering, ASCE*, 124(2), 140-149.

Zhang, Y. and Cundall, P. A. (1986). Numerical simulation of slow deformation, *Proc.,Symp. On the Mechanics of Particulate Media, 10th National Congress on Applied Mechanics,* Austin,Tex.

Zhou, J., Su, Y. and Chi, Y. (2006). Simulation of soil properties by particle flow code, *Chinese Journal of Geotechnical Engineering*, Vol. 28, No.3.

APPENDIX

The Numerical Servo-Mechanism

A servo-control algorithm was developed to reduce the difference between measured and required stresses (Itasca Consulting Group, Inc., 1999). A wall velocity is adjusted to make the measured stress close to required stress and control the stress state. The wall velocity $\dot{u}^{(w)}$ was calculated from a function of the measured stress $\sigma^{measured}$, the required stress $\sigma^{required}$ and a "gain" parameter G in Equation A.1.

$$\dot{u}^{(w)} = G\left(\sigma^{measured} - \sigma^{required}\right) = G\Delta\sigma \tag{A.1}$$

The maximum increment in wall force arising from wall movement in one timestep can be calculated using Equation A.2.

$$\Delta F^{(w)} = k_n^{(w)} N_c \dot{u}^{(w)} \Delta t \tag{A.2}$$

where N_c is the number of contacts on the wall, and $k_n^{(w)}$ is the average stiffness of these contacts. Therefore, the change in mean wall stress ($\Delta\sigma^{(w)}$) is calculated by Equation A.3.

$$\Delta\sigma^{(w)} = \frac{k_n^{(w)} N_c \dot{u}^{(w)} \Delta t}{A} \tag{A.3}$$

where A is the area of wall.

For stability, the absolute value of the change in wall stress must be less than the absolute value of the difference between the measured stresses and required stresses. Thus, a relaxation factor (α) is used and the stability requirement becomes:

$$\left|\Delta\sigma^{(w)}\right| < \alpha\left|\Delta\sigma\right| \tag{A.4}$$

Substituting Equations A.1 and A.3 into Equation A.4, we can get:

$$\frac{k_n^{(w)} N_c G\left|\Delta\sigma\right|\Delta t}{A} < \alpha\left|\Delta\sigma\right| \tag{A.5}$$

and the "gain" parameter can be determined by Equation A.6.

$$G = \frac{\alpha A}{k_n^{(w)} N_c \Delta t} \tag{A.6}$$

Therefore, the required stress can be achieved using Equation A.1 by adjusting the wall velocity.